ACS NANO

www.acsnano.org

REVIEW

Quantitative Phase Imaging: Recent Advances and Expanding Potential in Biomedicine

Thang L. Nguyen,[#] Soorya Pradeep,[#] Robert L. Judson-Torres, Jason Reed, Michael A. Teitell,* and Thomas A. Zangle*

Cite This: https://doi.org/10.1021/acsnano.1c11507

ABSTRACT: Quantitative phase imaging (QPI) is a label-free, wide-field microscopy approach with significant opportunities for biomedical applications. QPI uses the natural phase shift of light as it passes through a transparent object, such as a mammalian cell, to quantify biomass distribution and spatial and temporal changes in biomass. Reported in cell studies more than 60 years ago, ongoing advances in QPI hardware and software are leading to numerous applications in biology, with a dramatic expansion in utility over the past two decades. Today, investigations of cell size, morphology, behavior, cellular viscoelasticity, drug efficacy, biomass accumulation and turnover, and transport mechanics are supporting studies of development, physiology, neural activity, cancer, and additional physiological processes and diseases. Here, we review the field of QPI in biology starting with underlying principles, followed by a discussion of technical approaches currently available or being developed, and end with an examination of the breadth of applications in use or under development. We comment on strengths and shortcomings for the deployment of QPI in key biomedical contexts and conclude with emerging challenges and opportunities based on combining QPI with other methodologies that expand the scope and utility of QPI even further.

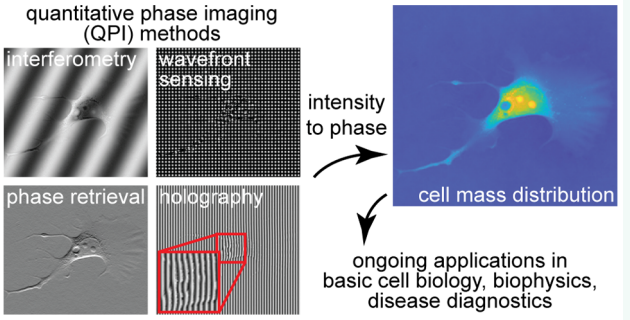

KEYWORDS: *microscopy, quantitative phase imaging, holography, tomography, interferometry, phase retrieval, diagnostics, biophysics*

Advances in microscopy have driven advances in biology and medicine by enabling visualization and greater perspectives on the machinery of life. In this review, we discuss advances in quantitative phase imaging (QPI), a label-free microscopy technique that measures fundamental cell properties and behaviors, including mass, mechanical properties, growth, and intracellular transport. We discuss the history of QPI, technical aspects of its applications, and emerging developments that will shape future applications of this technology for addressing opportunities and challenges in biomedicine.

QPI methods measure the phase shift of light as it passes through a transparent sample. This phase shift is caused by light slowing down as it passes through a material with a higher refractive index than water[1] and can be written as

$$\phi = \frac{2\pi}{\lambda}\int_{z=0}^{h} n(z)dz \tag{1}$$

where ϕ is the phase shift of light (in fractions of a wavelength) contributed by all elements in the sample of varying refractive index, n, through the height of the sample, h, in the z direction. This measured phase shift is directly proportional to the dry mass content of a biological sample.[2] Dry mass includes all mass excluding water and is therefore inclusive of biological macromolecules. For example, the increase of refractive index (real component) for a protein solution is proportional to the increase in protein concentration.[3] The slope of refractive index versus mass concentration defines this relationship and is called the specific refractive increment.[1,4] The average specific refractive increment, α, for the typical contents of mammalian cells, including proteins, nucleic acids, sugars, and lipids is $\sim 1.8-2.0 \times 10^{-4}$ m^3/kg,[2,3,5] with a value of 1.85×10^{-4} m^3/kg[1] used as a typical choice that is correct to within ~6%.[5] The cell dry mass, m, can then be calculated using the specific refractive increment, α, of a sample by[2]

$$m = \frac{\lambda}{2\pi\alpha}\int \phi dA \tag{2}$$

where this integral is performed over A, the imaged area of the cell, and λ is the wavelength of light used for imaging. The

Received: December 25, 2021
Accepted: July 14, 2022

https://doi.org/10.1021/acsnano.1c11507
ACS Nano XXXX, XXX, XXX−XXX

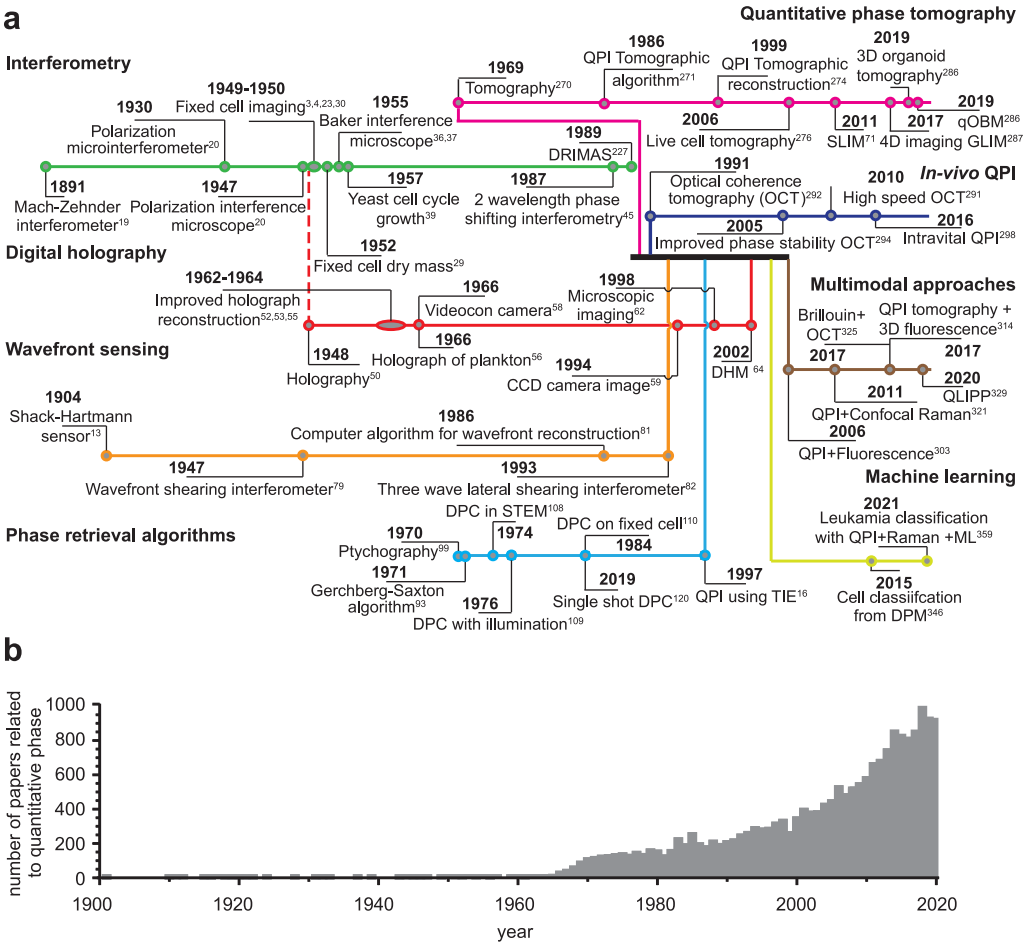

Figure 1. QPI has undergone a steady increase in interest driven by advances in different fields of optics. (a) Schematic of four main QPI approaches with interferometry (green timeline), holography (red timeline), wavefront sensing (orange timeline), and phase retrieval algorithms (light blue timeline) are indicated. These methods have improved extensively over time with the emergence of greater computational resources (thick black line). The improved efficiency of computational resources led to technical advances in QPI that include quantitative phase tomography (magenta timeline), *in vivo* QPI (dark blue timeline), multimodal approaches (brown timeline), and machine learning methods (yellow-green timeline). (b) The growth in interest and advances in QPI over time depicted by the number of publications on Web of Science using search terms "Quantitative Phase Imaging" or "Quantitative Phase Microscopy" by year.

ability of QPI to measure quantitative, biophysical features of the cell, such as mass, is central to its applications and potential in biomedicine.

Along with QPI, there are other widely used methods for leveraging the phase shift of light as it passes through a cell or other biological sample to generate image contrast. These include Zernike phase contrast microscopy[6,7] and Nomarski differential interference contrast (DIC) microscopy.[8] In phase contrast microscopy, a sample is illuminated with a limited spatial frequency range (background light). The refractive index distribution of nonuniform structures within cells then causes this background light to diffract and undergo a phase shift relative to the unperturbed background light. Both this diffraction and phase delay helps to generate contrast in the resulting image. As a result, even minute differences in refractive index translate into amplitude changes in the resulting image. In DIC microscopy, image contrast arises by splitting the incident light based on orthogonal polarization and introducing a small lateral shear of one polarization angle relative to the other using a Nomarski-modified Wollaston prism. Recombination of this polarized light after passing through the sample at a second Wollaston prism causes interference based on the relative phase shift between the two polarization angles. The image intensity in DIC microscopy, therefore, relates to the gradient of phase in the shear direction. Both phase contrast and DIC microscopy enable label-free measurements of cell shape and position. However, the intensity of images from phase contrast and DIC imaging do not linearly relate to the corresponding phase unless used as the basis for a phase retrieval method.[9,10] As a result, and in contrast to QPI, phase contrast and DIC microscopy remain qualitative phase methods. As discussed further, the quantitative data available with QPI enable more precise statistical and incremental studies for probing biological mechanisms than are available with qualitative methods.

In this review, we introduce the fundamental problem of QPI and trace the development of methods to solve this problem (Figure 1a). With the ever-increasing availability of computational resources, these solutions have increasingly converged, leading to a number of key applications in quantitative biology and a dramatic increase in research interest in QPI (Figure 1b). Finally, we conclude by discussing four key ongoing areas of QPI research that we believe will have the greatest influence in the future.

https://doi.org/10.1021/acsnano.1c11507
ACS Nano XXXX, XXX, XXX−XXX

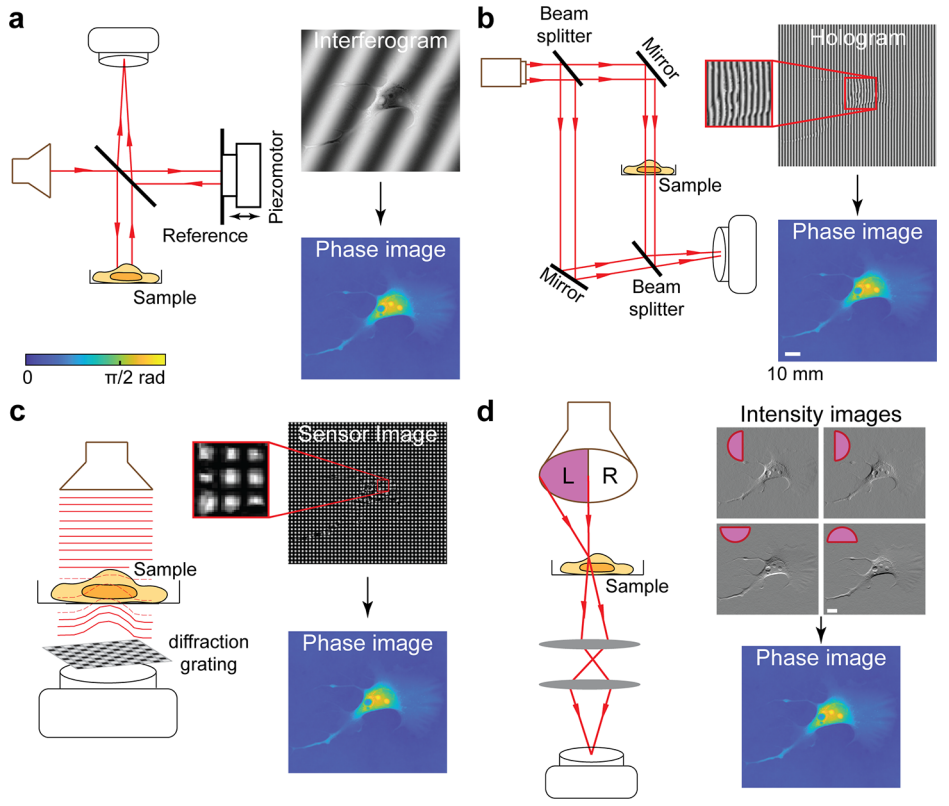

Figure 2. Examples of the four primary QPI lineages shown in Figure 1. (a) Michelson interferometry uses the interference between light beams passing through a sample and a reference to generate an interferogram that encodes phase information in the image amplitude (e.g. ref 12). The number of visible interference fringes generated depends on the optical setup and coherence of the light source, with low coherence light sources (e.g., white light)[24] producing fewer visible fringes than highly coherent lasers.[25] An in-focus interferogram is then used to generate the phase image, and, in phase shifting interferometry, the reference and sample path lengths are adjusted in steps, e.g., with a piezo, to shift the fringes by a fraction of a wavelength.[26] (b) DHM computationally reconstructs the phase image from an interferogram obtained using an interferometer.[27,28] Here, a Mach–Zehnder interferometer with a slightly off-axis reference beam is used to avoid the twin image problem, where the image and its conjugate sit on top of one another. (c) Wavefront sensing with QWLSI uses a diffraction grating that captures gradients in phase shift as local distortions in the resulting intensity grid pattern on the camera sensor.[14] A comparison of sample images to a reference wavefront image is used to determine the wavefront distortion due to the sample itself, with numerical integration to recover phase. (d) Differential phase contrast (DPC) microscopy, a deterministic phase retrieval method, images a sample using half-circle patterns of illumination that extend beyond the microscope objective numerical aperture. Light refraction through the sample then causes intensity increases (or decreases) in one-half-circle image and decreases (or increases) in image intensity with the opposing half-circle pattern. The normalized difference between these two images approximates the gradient of phase along one axis.[15] Multiple pairs of images are collected, and the phase is numerically reconstructed.

SOLVING THE FUNDAMENTAL PROBLEM OF QUANTITATIVE PHASE

QPI techniques seek to recover the phase shift of light that passes through a sample. However, conventional optical detectors recover only the amplitude of incident light, so additional optics and/or computations are necessary to recover phase shift information. This is the fundamental problem that all QPI methods must solve, which has stimulated the development of multiple QPI techniques. Here, we discuss the development of QPI in the context of these solutions, focusing on the four primary approaches that have had the largest impact on modern QPI methods and applications: interferometry,[11,12] wavefront sensing,[13,14] phase retrieval,[15,16] and digital holography.[17] While many of these approaches have integrated methods and concepts from electron, X-ray, and radio-wave techniques, here we use the term QPI to refer specifically to methods for phase retrieval based on visible light. We then discuss the convergence of these various techniques at the end of this section.

Interferometry. One method for computing phase information is interferometry. In interferometry, light incident on a sample is split into two paths, a sample path and a reference path, before recombining at a detector (Figure 2a). The amplitude of the resulting interference image relates to the phase shift of light passing through the sample with respect to the reference path by constructive and destructive interference between the light from these two paths. Interferometry was invented by Albert Michelson and improved further in collaboration with Edward Morley and famously used for the Nobel prize winning 1887 Michelson–Morley experiment that provided evidence against the existence of the luminiferous aether[18] (Figure 1a). Major early improvements were the introduction of separate sample and reference cells in the Mach–Zehnder interferometer[19] and use of thin calcite films faced at 45° to enable microinterferometry.[20] These dual path interferometers were followed by common-path interferometers where the reference beam and sample beam travel along the same path, reducing measurement sensitivity to vibra-

https://doi.org/10.1021/acsnano.1c11507
ACS Nano XXXX, XXX, XXX–XXX

tion.[21,22] A common-path interferometer microscope built by Dyson was used to image fixed biological specimens.[23]

The next major advance in QPI toward biomedical applications was the calibration of a specific refractive increment[3] using varying specimen compositions[29,30] that enabled the calculation of cell dry mass. The earliest applications of cell dry mass measurements with interferometry mostly focused on regularly shaped organisms such as yeast and bacteria to simplify calculations.[31,32] Early work on irregularly shaped cells used multiple images to find the total projected area and average optical thickness, the product of which is proportional to total cell dry mass through the specific refractive increment.[33] The integration of the scanning optical microspectrograph with the interference microscope increased resolution,[34] although not to the level of modern systems.[35] Other major improvements in interferometry focused on convenience for use in biological studies. This included a polarization interference microscope that replaced the partially silvered reflecting layers of earlier common path systems with a birefringent layer.[20] The Baker interference microscope, which was used widely on mammalian cells, is a polarizing microscope modified into a two beam interferometer.[36,37] Additional improvements included the use of a warmed stage to measure live yeast[38,39] or bacteria[32] and the replacement of uneven mercury lamp illumination with fiber optics. Although the relationship between amplitude and phase in interferometric images is straightforward, the required phase reference increases the complexity and number of optical elements and increases susceptibility to vibrations[40] and instability of a light source.[41] Therefore, it was not until the introduction of digital cameras and image processing[42,43] that interferometry provided reliable and reproducible quantitative data for internally complex mammalian cells.

Advances in a number of areas of interferometry-based QPI measurements benefit from the increasing use of computers. Automated image focusing has improved interference imaging accuracy and speed.[44] Single-wavelength interferometry cannot distinguish adjacent imaging pixels with a phase difference exceeding one-quarter of a wavelength,[2] but substantially larger phase shifts can be accurately measured by digitally combining images taken at two wavelengths.[45] Errors introduced from the unevenness of a reference surface can also be digitally corrected.[46] Phase shifting interferometry, in which multiple interference images are acquired at subwavelength shifts in the reference relative to the sample path length, corrects error due to external disturbances.[41] Applications of this approach with the required temporal and spatial resolution to study subtle changes in the shape of cancer cells require tight integration with computers for motion control and image processing.[35] Automated cell segmentation enables interferometry to measure the growth of many cells simultaneously in uniform[12] or mixed populations.[47] Automated segmentation has also improved the application of phase unwrapping or removal of phase jumps of one wavelength (2π radians) created due to the inherent ambiguity in interpreting interferometry data, thereby reducing errors in dry mass measurements.[48] Overall, computer control of interference microscopes and digital image processing of the resulting data has revolutionized this 100+ year old method and led to a convergence with other methods, as discussed below.

Digital Holography. Digital holography directly descends from interferometry (Figure 1a) and also captures the interference between a reference and sample beam. However, unlike interferometry, digital holography does not typically require mechanical scanning of the resulting interference fringes. In digital holography, the interferogram is captured with a digital camera placed at a known distance in front of the image plane.[49] This interferogram is analyzed using diffraction theory to reconstruct the complex object wavefront, including the phase shift and intensity modulation of light passing through the sample. Digital holography emerged from the establishment of holography by Gabor[50] for which he won the Nobel prize in 1971.[51] Gabor's work demonstrated that light from a point source interfering with secondary waves from light scattered by an object produces a negative photograph of a three-dimensional (3D) image. However, a conjugate image is also superimposed on the reconstructed image, resulting in ambiguity due to the presence of this twin image. It was later shown that use of an off-axis reference beam can separate the real and conjugate image.[52−55] Marine plankton provided an early application of live cells imaged using holography in a chamber with close proximity to a photographic plate.[56]

The use of digital cameras[57−59] and numerical reconstruction[60] has greatly improved the accessibility of holography. Since the 1970s, holography has been used extensively for cell imaging.[61] Later, digital holography was introduced for 3D imaging enabling visualization of specimens with highly fluctuating phase profiles such as pollen.[62] Initial applications of holography to quantitative phase measurements were restricted to measuring the refractive index distribution of inorganic materials,[63]. The broader application of digital holography to QPI was enabled by the development of efficient computational reconstruction of holograms in the early 2000s[64] as well as developments in the field of electron microscopy.[65] This led to digital holographic microscopy (DHM) of live neuron cells in culture with high phase accuracy.[27] Improved computational resources sped up the hologram reconstruction process for applications such as mapping the refractive index of cells.[66,67] Schlieren images were also generated from holography of patterns in inorganic materials,[68] which were later used to measure optical thickness.[69]

DHM has been implemented in multiple hardware configurations.[70] Of these, the Mach−Zehnder interferometer[19] is the most widely used (Figure 2b), although this approach has the same disadvantages of other double-path interferometers discussed previously. Traditionally, DHM requires spatially and temporally coherent laser light, leading to speckle noise. However, a number of white light and incoherent DHM alternatives are available, including spatial light interference microscopy (SLIM), a combination of digital holography and Zernike's phase contrast microscopy.[71] By processing a hologram of the 3D specimen wavefront, DHM also allows computational refocusing for the evaluation and standardization of QPI methods, discussed in more detail below.

Of note, DHM loses resolution with removal of the twin-image generated by in-line holography using the sideband technique[72] and through sideband filtering and cropping in the Fourier domain during hologram reconstruction in off-axis holography.[65] This loss of resolution of the reconstructed phase can be compensated by using higher numerical aperture and magnification objectives for imaging,[73] at the expense of obtaining fewer imaging pixels of phase data relative to other methods, such as phase shifting interferometry. Overall, DHM has high temporal resolution[74] and can be used for accurate

https://doi.org/10.1021/acsnano.1c11507
ACS Nano XXXX, XXX, XXX−XXX

phase measurements due to typically high signal-to-noise ratio in the reconstructed phase images.[75]

Wavefront Sensing. Wavefront sensing refers to approaches that seek to recover the aberrations in a wavefront caused by phase delays within a sample. Important wavefront sensing methods include Shack−Hartmann wavefront sensing[76] and Ronchi sensing.[77] Of these, the Shack−Hartmann wavefront sensor is the most commonly used version, with construction that uses either an array of evenly spaced holes or a lens microarray for improved image quality. Either of these arrays creates a pattern of focused light spots on the camera sensor.[78] Aberrations in the light wavefront causes these spots to move, allowing reconstruction of the total phase shift through the sample.

The earliest work in wavefront sensing used lateral shearing interferometry.[77,79] Lateral shearing wavefront imaging is similar to Nomarski DIC imaging in that the incident wave shears into two identical but tilted wave fronts that then interfere. The resulting single-direction phase gradient from lateral shearing interference data lacks the necessary gradient information to generate a complete two-dimensional (2D) phase-field and thus requires the use of multiwave interferometry techniques[80] that generate more than one gradient direction. Numerical reconstruction of the wavefront is possible, with such methods developed in 1986.[81] However, this method is computationally intensive and was later used in practice on images captured using a three-wave shearing interferometer configuration.[82] Typical wavefront sensors lack the resolution needed for imaging cells. Quadriwave lateral shearing interferometry (QWLSI) uses a modified, microfabricated Hartmann mask, resulting in a pattern of dark spots that measures phase gradients along perpendicular directions,[83] allowing the measurement of both intensity and phase (Figure 2c). Importantly, this mask enables high-resolution images to support the live cell application of wavefront sensing in measurements of phase using QWLSI on erythrocyte cells.[84]

Wavefront sensing has multiple advantages, such as higher sensitivity, speed, and temporal resolution with less complex instrumentation than typical interferometry methods.[14] Importantly, wavefront sensing techniques do not require a reference arm[14] and therefore are less affected by vibrations and other disturbances than double-path systems. Wavefront sensing typically also uses single image acquisition, resulting in high potential temporal resolution.[85] However, this approach has a trade-off with lower spatial resolution, as the light from each phase measurement spot is spread over many pixels on a digital camera sensor. Similar to DHM losing resolution due to sideband cropping in Fourier space during imaging and reconstruction,[86] this loss can be compensated for by using a higher NA objective for imaging.[73] Diffraction limited resolution in QWLSI can, therefore, be achieved in high magnification imaging, enabling phase sampling at double the diffraction limit and satisfying the Nyquist criteria.[87] Thus, wavefront sensing is a good choice for imaging high-speed cell dynamics requiring accurate phase information, but has the downside of lower spatial resolution. Theoretically single cell imaging with QWLSI phase images using an ideally matched reference image should result in flattened background, but there are often residual optical aberrations after reference subtraction[88] requiring a low degree polynomial fitting to flatten the image background for accurate biomass measurements.[75] In practice, these can result due to deviations in focal plane when screening across large surfaces or using multiwell plates, when changing media levels over the course of an experiment, or when using a previously acquired phase reference to enable faster imaging. Although other QPI methods like DHM can be improved with similar fitting procedures,[89] background fluctuations (when present) and an inherent amount of both spatial and temporal noise due to the recovery of phase by numerical integration can impact cell segmentation. Overall, however, this approach can achieve high accuracy for measurements of the dry mass of cells, even at high cell densities.[90]

Phase Retrieval Algorithms. Phase retrieval refers broadly to noninterferometric methods that computationally reconstruct the phase shift from a sequence of intensity images taken under varying conditions. The primary advantage of phase retrieval methods is that they can be performed using simpler optical systems or used to enhance the performance of more complex optical systems. Phase retrieval methods can be classified as either iterative or deterministic.[91] Iterative methods use iterative computation to satisfy constraints in object and Fourier space between intensity images at the sample and detector plane to resolve the phase problem.[92] Iterative methods of phase retrieval were originally developed for electron microscopy to reconstruct the wavefront propagation between image and diffraction planes from the corresponding amplitude images.[93] The Gerchberg−Saxton (GS) algorithm was a widely used iterative phase retrieval method. The GS method iteratively approximates both source (e.g., illumination) and target (e.g., image) intensities and complex phase distributions from measured intensity images of the source and target. However, the GS algorithm typically requires a large number of iterations and can become stuck at local minima and therefore not converge on the real phase solution.[94] This was addressed by the introduction of the steepest gradient search[94] and input-output methods.[95] One common implementation of iterative phase retrieval is in Fourier ptychography.[96−98] Ptychography was developed to solve the phase problem in electron diffraction measurements.[99] Fourier ptychography recovers high spatial resolution (or large field of view) phase information at the object plane from a series of intensity images, such as at varying angles, resulting in data from which a higher spatial frequency image can be reconstructed.[100,101] Fourier ptychography has also been used to visualize the 3D structures from light scattering signals[102] or complex transmittance functions.[98]

Deterministic methods directly solve for phase images without iteration, enabling real-time phase imaging. One commonly used approach is based on the transport of intensity (TIE) equation which relates phase data at the in-focus plane to the axial derivative of intensity distribution.[103] The TIE equation was proposed based on conservation of energy and describes the transport of energy in an optical field.[16] TIE methods can be used along with other phase retrieval algorithms to improve image quality.[104] Differential phase contrast (DPC) microscopy, another commonly used deterministic imaging method, evolved from the idea of contrast enhancement by asymmetric illumination.[105] In DPC microscopy, multiple images of the specimen are obtained at different angles of half-plane illumination to recover phase information[106] (Figure 2d). In this way, DPC imaging is similar to Schlieren imaging in which half-plane illumination is used to remove half the spatial frequencies from the intensity image in one direction, giving phase gradients in orthogonal dimensions.[107] The earliest work on DPC imaging used a half-

https://doi.org/10.1021/acsnano.1c11507
ACS Nano XXXX, XXX, XXX−XXX

plane electron source in a scanning transmission electron microscope[108] and was later applied to imaging with visible light[109] and applied to increase contrast in images of fixed cells.[110]

In contrast with interferometric methods, phase retrieval is typically less costly or uses more widely available optics, such as DIC,[111] phase contrast,[112,113] or custom-made imaging systems.[15] This is because phase retrieval algorithms eliminate the use of a reference based on knowledge, or approximation, of the optical transfer function of the imaging system.[114] Phase retrieval is also possible with partially coherent light sources.[115−117] However, the requirement of multiple images as inputs for phase retrieval methods lowers the imaging temporal resolution compared to interference and wavefront sensing methods.[75] The use of iterative algorithms for phase retrieval also increases the overall workflow time.

As a primarily computational method, phase retrieval has benefited greatly from advances in computing power. The practical application of phase retrieval for QPI therefore began in the 1990s with extensive use of computing resources.[118,119] Advances in optical systems further enhanced phase retrieval QPI, including the use of color-multiplexing to obtain phase data from a single image,[120] lens-less phase retrieval with super-resolution reconstruction,[121] and volumetric holography using asymmetric illumination.[122] Looking forward, phase retrieval stands to benefit greatly from future advances in computation. This is especially evident in recent applications of machine learning, where phase retrieval is possible without an optical physics model.[123,124] A possible limitation that needs addressing as this field moves forward is that with more computation, more noise tends to occur. Additionally, the more opaque the method, the harder it is to track down sources of error, a particular concern with machine learning approaches. Overall, however, these advances, combined with the ability to work with data acquired from diverse sets of optical approaches, points toward a larger role for phase retrieval methods in the future of QPI.

Comparison and Evaluation of QPI Methods. Each lineage of QPI methods has advantages and disadvantages compared to one another, which have diminished in magnitude over time from technological advances and verified standardizations. Briefly summarizing the four QPI lineages described above: interferometry is accurate but sensitive to reference arm noise; wavefront sensing has good temporal resolution and no reference arm, but has low spatial resolution; phase retrieval provides a large field of view and higher spatial resolution, but has low temporal resolution; and DHM has high temporal resolution but, as an interferometric approach, is susceptible to noise from a reference arm.

A number of technical improvements address key limitations of these four QPI lineage approaches. For example, adapting DPC microscopy to work with multicolor illumination instead of separately imaging individual illumination patterns[125−128] achieved temporal resolution as high as 100 frames per second (fps).[129] A high-speed interferometry method using a diffraction grating generated a temporal resolution of 10^4 fps.[128] Recent developments in DHM systems enabled removal of a reference arm, for instance, by using a self-referencing module.[130] It was shown that holography could mathematically retrieve phase using single intensity images through an illumination control without a reference.[131] The use of coherent and partially coherent illumination can also help to reduce noise in QPI. Coherent illumination, such as from a laser, while useful for generating interference, has a disadvantage of being sensitive to noise from system optics, especially speckle noise.[132] Use of partially coherent illumination, such as from an LED or lamp, can eliminate these artifacts, at the cost of a moderate increase in difficulty aligning the optical system. Sub-Rayleigh resolution has been achieved by adjusting the illumination source.[133] Mach−Zehnder interferometry has been adapted for biosensing within microchannels, increasing sensitivity.[125,126]

Another approach to generate improvements in QPI is to combine principles from different QPI lineages. For example, interferometry using a diffraction grating in a Mach−Zehnder system can eliminate the need for a reference arm and increase phase sensitivity, by reducing measurement noise.[127] The use of iterative phase retrieval algorithms on single-shot holograms also enables the 3D reconstruction of QPI images without needing a reference standard.[92] Applying iterative phase retrieval algorithms to holographic techniques has also increased spatial resolution.[134] The same iterative phase retrieval method has also been successfully applied to transport of intensity algorithms using holographic microscopy[135] to improve image quality.[136] The transport of intensity equation can be used to capture 3D QPI images at the diffraction limit using an electrically tunable microlens array, similar to that used in wavefront sensing, thereby significantly increasing temporal resolution.[137]

The software package used for assessing QPI measurements is another key system consideration. Some QPI approaches have available commercial analytic packages including those from Wyko Corporation, Phasics Corporation, Phase Holographic Imaging (PHI), Inc. and other vendors, whereas some analytical packages are custom-coded in MATLAB or Python. The choice of commercial versus custom-written software is critical for individual use cases, as custom software may be more flexible, at the cost of additional complexity. Table 1 summarizes the available software, for example, methods from the four QPI lineages discussed in this review.

Polystyrene beads are a widely used phase calibration standard for many QPI methods[138,139] and have been used with DHM,[140] QWLSI,[14] and DPC[141] techniques. However, there is variability in the refractive index of polystyrene,[142] and typically large refractive index differences between polystyrene beads relative to cell culture media, combined with sharp "imaging edges" of these round beads, can lead to phase unwrapping artifacts that are not usually encountered with live cell samples. Potential phase unwrapping artifacts using polystyrene bead calibration standards can be mitigated by, for example, mounting the beads within material with a closer refractive index.[139,143] However, this approach also moves the calibration data range further from actual cell imaging conditions, which could impact experimental accuracy. Red blood cells have also been used as a phase calibration standard in the development of QPI methods because of their availability and fairly uniform shape and size.[12,144] Typically, nondiseased RBCs show a population dry mass variation of ~15%.[145] However, as a biological sample, this can be more challenging to work with than an inanimate calibration standard. A number of studies have used USAF resolution test targets that are readily available because of their wide use in calibrating imaging systems.[138,146] However, these standards are typically used for calibrating intensity images and are made of thin metal films, meaning that they do not function as pure phase objects. A phase specific calibration standard for QPI

https://doi.org/10.1021/acsnano.1c11507
ACS Nano XXXX, XXX, XXX−XXX

Table 1. Example Methods, Key Benefits, Performance, and Software for Different QPI Lineages

Lineage	Example methods	Key improvements	Temporal resolution	Bkg std dev	Accuracy	SNR	Software
Interferometry	Michelson interferometer, Mach–Zehnder interferometer, Baker interferometer	Phase shifting interferometry method	100 fps,[138] 250 fps[153]	0.043[41]	2%,[153] 0.5%[152]	Peak SNR < 30[154]	Wyko Vision software[35,155]
Digital holography	Same as interferometry, reconstruction in addition	Self-referencing module,[130] less susceptible to noise	10^6 fps[74]	4 nm, Polychromatic DHM[156]	0.3%[157]	Peak SNR < 55,[150] SNR < 10[158]	HoloStudio (Holomonitor, phi),[159] Koala (Lyncee tech),[160] Python[17]
Wavefront sensing	Lateral shearing interferometry, QWLSI	Increased spatial resolution	10^4 fps[128]	0.88 nm,[88] 0.38 nm[151]	2% (1 nm sensitivity)[14]	SNR < 8[161]	Phasics,[14] MATLAB[162]
Phase retrieval algorithms	Iterative algorithms: Defocus methods (GS algorithm, hybrid input-output algorithm, others), Fourier ptychographic microscopy Deterministic methods: TIE, DPC	Increased temporal resolution	100 fps[129]	1.81 pg[163]	0.1–0.2[164]	SNR < 6,[165,166] SNR < 100[167]	Python,[168] ImageJ,[168] MATLAB[169,170]

was developed and used in a comparison with atomic force microscopy (AFM), which showed that QPI has nanometer sensitivity over a wide range of spatial frequencies.[97] A 3D phase "phantom" that captures subcellular features of cells for calibration in 3D QPI methods has also been demonstrated,[147] however further development and characterization of widely accessible standards is needed to support continued advances in QPI.

Critical Performance Metrics for QPI. Quantitative comparison of QPI systems can be performed using a number of critical performance metrics that define the quality of images and data provided by QPI. These include accuracy, signal-to-noise ratio (SNR), phase measurement sensitivity, and both spatial and temporal resolution of the resulting QPI data.

Accuracy indicates the ability of the combined microscopy method and reconstruction algorithm to compute the expected phase shift of a calibration sample. Accuracy can be computed from differences in the computed phase shift (ϕ_{Measured}) to the expected phase shift (ϕ_{Actual}):

$$\text{Accuracy} = \frac{|\phi_{\text{Measured}} - \phi_{\text{Actual}}|}{\phi_{\text{Actual}}} \times 100\% \tag{3}$$

Background standard deviation quantifies the phase image reconstruction accuracy as well and is calculated as standard deviation of the segmented blank spaces in phase images or reference phase images.[88] The background standard deviation can then be used to estimate the SNR as the absolute mean phase signal ($|\varphi|$) over the standard deviation of the measured background (σ):[142,148]

$$\text{SNR} = \frac{|\varphi|}{\sigma} \tag{4}$$

SNR is used to define image quality when analyzing images for measuring physical quantities, e.g., phase shift, optical volume, or cell mass.

The peak spatial SNR of phase images (PSNR) is another metric used to measure the quality of reconstructed images. Unlike SNR, PSNR is not affected by image intensity rescaling.[149] PSNR can calculated as[150]

$$\text{PSNR} = 10 \times \log_{10}\left(\frac{R}{\text{MSE}}\right) \tag{5}$$

where R is the maximum fluctuation in the image, and MSE is the mean squared error between the reconstructed image and the reference. The error in phase is the standard deviation of the phase signal to the mean of phase signal subtraction.[88]

Noise in QPI measurements can be reduced, increasing the SNR, by increasing the number of measurements. This is especially important when using coherent illumination.[75] Sources of noise may include temporal and spatial variations along with fluctuations over repeated measurements.[151] These combined sources of noise may account for <1% to 5% of total biomass measured, depending on the magnification of the measurement.[151] This noise also contributes to the overall phase measurement sensitivity of a system, which can be quantified by the Cramér–Rao bound algorithmic sensitivity and experimental sensitivity of the system.[152]

The theoretical spatial resolution of a QPI system can be determined from the objective numerical aperture (NA) and illumination (NA_i) as

https://doi.org/10.1021/acsnano.1c11507
ACS Nano XXXX, XXX, XXX–XXX

$$r = \frac{1.22\lambda}{\mathrm{NA} + \mathrm{NA}_i} \tag{6}$$

where r is the spatial resolution limit of the system, with low specimen contrast or improper illumination lowering this value. Spatial resolution also becomes diffraction limited when using a high NA imaging objective. A phase signal must be sampled at twice the diffraction limit of the system to satisfy Nyquist criteria, thereby yielding diffraction limited resolution.[87] This means two features in a sample separated by the diffraction limit will be captured by two separate phase imaging pixels.

In order to obtain phase data, all methods trade some imaging performance, which can limit the achievable spatial or temporal resolution. DHM requires cropping in the Fourier domain[86] (Figure 2b), while wavefront sensing requires integration over multiple pixels (Figure 2c), with data processing via cropping in Fourier space as well.[83] This means for a given camera sensor size (e.g., 1 megapixel), the resulting number of phase pixels will be lower for DHM or wavefront sensing, though the diffraction limit can be achieved with such methods, at the cost of fewer phase pixels and a smaller field of view available for viewing the sample. However, methods that use the full resolution of the camera sensor typically trade away some temporal resolution by requiring multiple exposures to reconstruct a single phase image. For example, in phase shifting interferometry (Figure 2a) up to nine images are acquired with small shifts of the path lengths of the reference arm relative to the sample arm in order to reconstruct a single phase image. Typical phase retrieval methods require multiple image acquisitions as well. For example, four images are required to reconstruct a single phase image in DPC microscopy (Figure 2d).

A summary of critical performance metrics, including the reported accuracy, SNR, resolution, and background standard deviation, for the discussed QPI modalities is summarized in Table 1.

Impact of Image Focus Position on QPI Performance. A key factor influencing performance of 2D QPI methods is the focal position or location of the image plane along the optical axis, used for capturing phase images. QPI images taken out of focus show up to a 40% difference in measured optical volume differences for uniform microspheres, and QPI images of cells can show up to a 25% decrease in measured biomass compared to in focus QPI images.[143] For 2D QPI, more planar adherent cells show greater measurement robustness with imperfect focal position relative to rounded cells, although there can be a significant difference in QPI dry mass data due to focus position even for flatter, adherent cells.[151] This dependence on focal position illustrates the importance of getting this parameter correct. A key parameter to consider for correct focal plane imaging is the depth of field (DFD), computed as[171]

$$\mathrm{DFD} = \frac{\lambda\sqrt{n - \mathrm{NA}_i^2}}{\mathrm{NA} \times \mathrm{NA}_i} \tag{7}$$

where n is the refractive index of the material between the objective and sample. A larger depth of field can introduce errors due to dust and debris above or below the sample,[151] whereas a smaller depth of field increases the sensitivity to out of focus imaging. Overall, the importance of focal position imaging necessitates the use of algorithms to determine the correct focal position for accurate and reproducible QPI data collection.

Selection of an appropriate algorithm and metric for optimal focusing, or autofocusing during automated image acquisition, depends on the QPI imaging modality. For example, in interferometric systems with a low coherence light source, such as phase shifting interferometry, focus can be achieved by maximizing the contrast of the interference fringe intensity as the focal position is adjusted.[172,173] Maximized fringe contrast results in a minimized optical path difference between the sample and reference light paths of an interferometer. The use of an external focusing tool such as a digital video disc pickup head can also be applied to determine optimal focal position of both reference and sample arms.[173] External focusing tools are not limited for use to interferometry and can also be used for optimizing the focal imaging plane in other QPI modalities, such as using a laser focusing device to determine the optimal focal imaging plane in wavefront sensing QWLSI systems.[85]

All QPI imaging modalities, including noninterferometric methods such as wavefront sensing and phase retrieval, can make use of more conventional autofocusing techniques based on image features. Focus optimizing algorithms are evaluated by their unimodality (focus functions require a singular peak), accuracy (the focus function extremum should match the location of best focus), robustness (the extremum of the focus function should be a sharp peak), and range (focus function should have a smooth, broad tail to enable focusing over a wide range).[174] For example, two focus functions that performed well in approaching these desired qualities were a differentiation based method, such as the squared gradient (SG), and a Laplacian (LA) focus method:[174]

$$\mathrm{SG} = \iint_{\mathrm{image}} \left|\frac{\partial g(x, y)}{\partial x}\right|^2 dxdy \tag{8}$$

$$\mathrm{LA} = \iint_{\mathrm{image}} \left|\frac{\partial^2 g(x, y)}{\partial x^2}\right|^2 dxdy \tag{9}$$

where g is the gray scaled image value measured as a function of spatial position, x and y. Faster wavefront sensing autofocusing algorithms have also optimized for the Tamura coefficient (TC)[175,176] defined as

$$\mathrm{TC} = \sqrt{\frac{\sigma(g)}{g}} \tag{10}$$

where $\sigma(g)$ is the standard deviation of the grayscale intensity, and g is the average grayscale image intensity. Reported DHM focus methods have also maximized image sharpness using the weighted spectral analysis (SPEC) and cumulated edge detection by gradient calculation (GRA):[177]

$$\mathrm{SPEC} = \sum_{u,v} \log(1 + F_B(g)(u, v)) \tag{11}$$

$$\mathrm{GRA} = \iint_{\mathrm{image}} \sqrt{\left|\frac{\partial g(x, y)}{\partial x}\right|^2 + \left|\frac{\partial g(x, y)}{\partial y}\right|^2} dxdy \tag{12}$$

where $F_B(g)(u, v)$ is the band-pass filtered Fourier transform of the grayscale image, g, summed over the Fourier domain coordinates, u,v.

Additionally, by capturing a hologram that reflects the complex optical field, DHM enables numerical refocusing after

https://doi.org/10.1021/acsnano.1c11507
ACS Nano XXXX, XXX, XXX−XXX

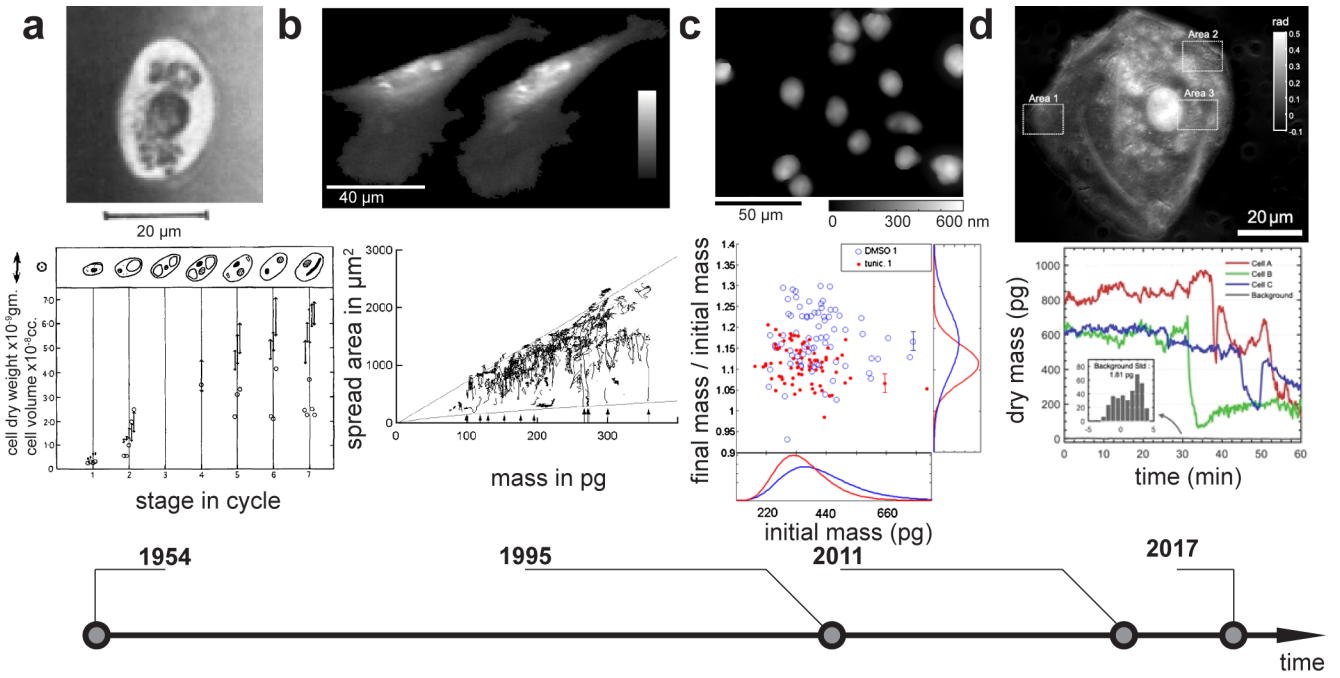

Figure 3. Evolution of complexity and information content from QPI measurements of cell dry mass and mass distributions within living cells. Representative images and data analyses are shown in a time series. (a) QPI film image of *Tradescantia bractea* pollen grain (top) along with QPI pollen grain dry mass measurements (bottom, upward arrowheads are no sucrose estimates and downward arrowheads show measurements within a 5% sucrose solution) and volume (circles) during different phases of development. Adapted with permission from ref 191 .Copyright 1954 Company of Biologists Ltd. (b) QPI of chicken fibroblasts with dry mass densities ranging from 0.01 (darkest gray) to 0.6 (white) pg/μm^2(top), processed to measure spread area relative to total cell mass (bottom). Adapted with permission from ref 202. Copyright 1995 Company of Biologists Ltd. (c) QPI of human H929 multiple myeloma cells (top) showing computationally processed data that simultaneously captures drug responses of hundreds of single cells, shown as initial cell mass versus normalized changes in mass during drug treatment (bottom). Adapted and data set with permission from ref 12. Copyright 2011 Elsevier. (d) High-resolution QPI of a human buccal epithelial cell (top) and an example of changes in dry mass of HeLa cells undergoing apoptosis triggered by exposure to cytotoxic paclitaxel (bottom). Adapted with permission under Creative Commons Attribution (CC BY) license from ref 163. Copyright 2017 Springer Nature.

image acquisition. This approach can be used to adjust for optical aberrations and enlarge the depth of examination[178] without the need for additional mechanical scanning. The range for which the refocusing distance produces accurate information is defined by[179,180]

$$|\Delta z| \ll \mathrm{DFD} \tag{13}$$

where Δz is the distance of refocusing and DFD is defined in eq 7.

There are many autofocus algorithms for numerical refocusing including those that use amplitude,[182] sparsity,[183,184] a correlation coefficient,[185] and other properties[186] to determine optimal focus in DHM. One example of a DHM numerical refocusing metric that achieves the desired properties of a focal position algorithm is the DarkFocus (DF) metric,[181] which optimizes for the sharpness of images as

$$\mathrm{DF} = var(\nabla|U(z)|) \tag{14}$$

where *var* is the variance operator and $U(z)$ is the complex optical field calculated for a focal distance, z. However, these methods of refocusing may suffer errors when applied to nonideal situations, such as using coherent light based algorithms for an extended or spatially incoherent light source,[179] and thus must be tailored for specific DHM applications.

Computational Convergence. Starting in the early 2000s, QPI began to rely increasingly on digital image acquisition and data processing, with the field also advancing from creative method combinations that were emerging from multiple technical lineages. For example, SLIM combines principles of digital holography with phase contrast methods,[71] and QWLSI combines the principles of wavefront sensing with interferometry and phase retrieval algorithms.[14] The combination of DHM with principles from lateral shearing interferometry addresses the twin image problem,[187] and this combined approach can reconstruct optimally sampled QPI data.[188] Further improvements in computation and machine learning are enabling approaches analogous to QWLSI using unstructured, random phase masks. These exciting developments point toward the future of QPI with increasing availability of computational resources and algorithms, including creative applications of machine learning, which will further advance quantitative studies in biology and medicine.

ADVANCES IN QUANTITATIVE BIOLOGY

As QPI approaches have advanced, so too have QPI applications. One advantage of QPI is that it is label-free. Therefore, QPI can study cell behavior with minimal impact, a leveraged feature in a number of biological applications. As summarized above, there are also a number of additional label-free microscopy approaches, including the more widely used methods of phase contrast and DIC microscopy. The primary advantage of QPI over these other approaches, however, is

https://doi.org/10.1021/acsnano.1c11507
ACS Nano XXXX, XXX, XXX−XXX

that, in contrast to phase contrast or DIC microscopy, the data contained in each pixel of a QPI image are a quantitative measure of the phase delay of light as it passes through that portion of a sample. Measurement of this phase delay can utilize any of the approaches already discussed above. Once captured, analysis of this phase data can provide quantitative insights into numerous biological processes and systems. Here we summarize key advances in the application of QPI to quantitative studies in biology, ranging from applications that quantify the behavior of individual cells to emerging opportunities in clinical diagnostics.

QPI Applications Using Measurements of Cell Mass or Growth Rate. The refractive index of a material is related to its mass through a quantity called the specific refractive increment.[5] For cells, a typical average value is $1.8-2.0 \times 10^{-4}$ m^3/kg.[2,3,5] The phase shift measured by QPI is the integral of the difference in refractive index between a cell and its surroundings through the thickness of a cell's projected area. The measured phase shift of a cell is proportional to the mass of the cell's contents excluding water, which is the dry mass of the cell. This provides a quantitative measure of cell size, which can provide valuable information on cell viability, growth over time, replication, and function. Measuring cell volume is an alternative method to cell mass quantification that can be used to measure cell growth.[189] However, measurements of cell volume typically require a simplifying assumption about cell shape (e.g., spherical mammalian cells, rod-shaped bacterial cells) and cell volume changes depend upon intra- and extracellular osmolality, which can be unrelated to internal dry mass amounts.[190] By contrast, dry mass is independent of osmolality and instead depends upon the balance of biosynthetic (anabolic) and degradative (catabolic) processes within a cell. In the early- to mid-1950s, several investigators began using QPI to measure the absolute total dry mass of live eukaryotic cells, including measurements of mass throughout the cell cycle[4,29,30,38,191] (Figure 3). Additionally, repeated QPI measurements of dry cell mass over time can provide dry mass accumulation or loss rates to quantify cell growth[12,190,192−196] (Figure 3), or the decrease in mass that occurs during cell death.[163,197−201] Below, we discuss example applications of QPI measurements of cell mass and growth in studies of basic biological processes, including in immunology and in the behavior of neurons.

Applications of QPI to Studies of Cell Growth and Associated Biological Processes. Several example studies discussed here demonstrate the utility of QPI measurements for providing insight into the regulation of cell size, growth, and additional fundamental biological processes. In studies of cell size regulation, QPI measurements during fibroblast cell spreading revealed that the spread area is actively regulated by an undefined mechanism that adjusts the total area of spreading proportionally to the total cell mass.[202] Separately, dry mass quantification using SLIM during the cell cycle showed that osteosarcoma cells exhibit a mass-dependent growth that was best approximated by an exponential rather than a linear model of cell growth.[192] More precise QPI measurements of cell mass revealed oscillations in growth rate that were previously unappreciated, suggesting that a pure exponential model of cell growth is insufficient to explain the regulation of mammalian cell growth.[88]

The impact of extracellular perturbations on cell size and growth have also been interrogated by QPI. For example, changes in available glucose,[194] or the addition of small molecule inhibitors such as tunicamycin to induce cell stress,[12] led to reproducible, QPI-quantifiable changes in cell dry mass and growth rate as indicators of cellular responses. These study results led to the use of QPI as a label-free method for screening different stimulants or inhibitors. Examples include QPI-based screens for agents that cause changes in cell growth rate and cytotoxicity.[12,160] QPI has also been applied to study the influence of mechanical properties of the extracellular matrix on growth rate, migration, and metastatic potential of melanoma cells.[203] Long-term SLIM studies of cell growth in epithelial and fibroblast cocultures examined the influence of cell clusters on neighboring cells, with a few clusters, termed "influencer clusters", showing a strong correlation between growth rate and distance, with potential implications for organogenesis and cancer cell metastasis.[203]

QPI has also enabled studies of the impact of genetic mutations on cell growth. For example, QPI tracked the growth and division of primary human melanocytes for 30 days in culture.[204] Results showed that a proliferative arrest associated with oncogene expression, previously thought to be caused by G0 cell cycle phase senescence, was a reversible and conditional mitotic arrest, an observation subsequently validated using clinical specimens. QPI also confirmed the impact of transcription factor YAP expression in HEK293 cells as a potential coordinating mechanism between cell and tissue size.[205] Additionally, QPI helped to demonstrate utility for assessing whether different cell states, and transitions between cell states, alter the absolute dry mass or dry mass accumulation or loss rates of cells. One study quantified cell dry mass partitioning between daughter cells during and following cytokinesis and showed that mass asymmetry present at the time of cleavage furrow formation persisted through cytokinesis.[11] Addition of cytoskeleton-disrupting agents with differing mechanisms of action, including latrunculin A, blebbistatin, nocadozole, and cytochalasin B increased the number of daughter cell pairs exhibiting asymmetric dry mass partitioning. This suggested an absence of an active mass partitioning mechanism after cleavage furrow positioning and the requirement for mass adjustments by dynamic changes in cell growth rate, and/or cell cycle time, over the succeeding cell cycle. The lineage nondirected differentiation of human pluripotent stem cells (hPSCs)[206] was also interrogated using QPI measurements of absolute dry mass and changes in growth and mass redistribution rates prior to and following the induction of differentiation. Study findings included that hPSCs grow at a consistent, exponential rate independent of colony size, with coordinated intracolony mass movement ceasing with the onset of differentiation. In contrast, growth and proliferation rates decreased by only ~15% during early differentiation despite global changes in gene expression and energy metabolism, suggesting that the regulation of mass and proliferation are independent of pluripotency during early differentiation.

Applications of QPI to Studies of Immune Cell Behavior. QPI measurements have also been used to gain insights into the functions of cells of the mammalian immune system. At the cellular level, the adaptive immune response requires rapid, massive cell growth to support the generation of both effector and long-lived memory cells. QPI, therefore, is well suited to studying the regulation and features of this process. For example, QPI measures of dry mass changes in a binary cytotoxic T lymphocyte (CTL) − cognate cancer-cell killing assay were illuminating. Study results revealed that the

https://doi.org/10.1021/acsnano.1c11507
ACS Nano XXXX, XXX, XXX−XXX

cancer cell mass decreased 20−60% over 1−4 h during a successful CTL attack, with a 4-fold increase in CTL mass accumulation rate at the start of killing and a 2−3-fold increase in CTL absolute mass relative to the mass of unresponsive T cells.[47] These results provide a kinetic, quantitative assessment of CTL activation in tumor cell killing and, potentially, a relatively rapid way to identify specific, activated patient-derived T cells for applications in cancer immunotherapy. Furthermore, QPI measurements of reconstituting donor T cells following hematopoietic stem cell transplantation showed mass changes correlated with immune reconstitution within the first few weeks post-transplant, a finding which could guide the withdrawal of immunosuppressive drugs and reduce the likelihood of graft-versus-host disease or cancer relapse.[207]

In studies of B lymphocytes, QPI measurements also uncovered rapid mass accumulation and cell proliferation within the first 24 h of B cell activation accompanied by sustained AMP-kinase activation in the absence of energetic stress, an unexpected result because AMP-kinase activity strongly opposes anabolism and constrains mass accumulation in most biological contexts.[208] QPI was also used to measure variability in naïve B cell size and partitioning of mass between daughter cells during B cell expansion, providing support for an in silico model suggesting that intrinsic biological noise plays a key role in determining the extent of B cell proliferation, which ultimately determines which cells contribute to an immune response.[209]

Applications of QPI to Measure Neuron Behavior. Neuron growth and behavior is yet another impactful area for QPI applications. Many studies would benefit from imaging with a label-free method that avoids phototoxicity and photobleaching from long duration fluorescence imaging. As an example, label-free QPI separately quantified neuronal body (soma) and projection (neurite) masses, which showed that most mass accumulation during a 5 d *in vitro* neuronal differentiation protocol goes toward the production of additional neurite connections rather than strengthening of existing connections.[210] The process of neuronal branching has also been quantified using QPI plus machine learning as an alternative to fluorescent staining.[211] The high sensitivity of QPI has been leveraged to track the transport of individual vesicles within neuronal processes.[212] QPI has also been applied to measure long-term (∼1 min) responses of neurons to stimulation related to transmembrane ion fluxes[213] as well as short-term (∼0.1 ms)[88] fluctuations in neuron shape during neuronal spikes.[128]

Applications of QPI in Measuring the Physical Structure of a Cell. In addition to measuring total cell mass, QPI can also measure the distribution of dry mass within cells. This enables QPI applications that measure the structural features of individual cells and use this information to inform physical models. For example, a recent study showed that the morphological differences in retinal nuclei of mice correspond to a pattern of nuclear architecture common to other nocturnal mammals.[214] Specifically, adult mouse retinal cells showed a spatially organized nuclear refractive index pattern, which contrasted with a more dispersed refractive index pattern uncovered in diurnal pig or immature mouse retinal cells. Simulations of light transmission found that the refractive index pattern in mouse retinal cells more effectively focused light and reduced scattering, suggesting a potential role in enhancing nocturnal vision. This result generated much discussion on the role of refractive index patterns in the nucleus. The appearance of a large phase shift through cell nuclei supports a physical model of a reduced nuclear refractive index,[215] which has been validated in other studies reporting a lower refractive index in nuclei than in the cytoplasm.[216−219] These results were further supported by 3D QPI results that also showed a lower nuclear refractive index outside of the nucleolus.[220,221]

Applications of QPI in Studies of Intracellular Transport. Intra- and intercellular transport of biomaterials are required for cell growth and function, with patterns of transport providing information on cell behavior, disease states, and cellular responses to changing environmental conditions. Two relatively common, non-QPI methods for studying cellular transport employ fluorescent labels typically attached to biomolecules, or to introduced particles, coupled with live cell imaging,[222,223] and label-free techniques, such as DIC microscopy.[224] Imaging of fluorescently tagged markers provides a high degree of specificity, and can be quite sensitive, but suffers the disadvantages of photobleaching, limiting transport study times, phototoxicity, which can induce cell stress and modify cell behavior, and autofluorescence, which excitation or emission filters may not completely remove.[225] These imaging limitations are irrelevant for QPI, although there is a loss of biomolecule specificity and sensitivity.[224] As discussed previously, QPI, unlike DIC and phase-contrast imaging, also quantifies the dry mass of cells and some tracked intra- and intercellular components, such as lipid droplets, revealing that lipid trafficking motion ranges from subdiffusive to active transport.[226] As a label-free method that provides additional quantitative data on cell behavior, QPI is a good option to consider for measurements of intracellular transport.

Imaging interferometry coupled to finite element analysis measured the intracellular transport of dry mass in fibroblasts at low resolution and showed that the kinetic energy of intracellular motility can be several hundred times greater than the kinetic energy of cellular translocation across a surface.[227] Recent improvements in image processing speed and methods are helping to increase the scope of intracellular transport studies available to QPI platform methods. For example, SLIM measured the label-free diffusion of organelles and vesicles in hippocampal neurons and cardiomyocytes using a Laplace operator, with extended transport study time enabling extraction of diffusion coefficients.[212] SLIM also revealed the 3D time series movement of dry mass in neurons. Results were analyzed using dispersion-relation phase spectroscopy, a method to measure the spatiotemporal decay of the autocorrelation signal of phase,[212] and revealed differences between transport in neuronal bodies and neurites, and also between longitudinal and transverse trafficking orientations.[228] Additional SLIM platform studies were inconsistent with purely passive diffusion and suggested advective transport of cargo within neuronal dendrites, also using the dispersion-relation phase spectroscopy analytic technique.[212] A holo-tomographic version of QPI combined with epifluorescence examined mitochondrial network and lipid droplet dynamics inside HeLa endocervical carcinoma cells. Features uncovered included the shape and dry mass dynamics of lipid droplets, endocytic structures, and a multiorganelle spinning phenomenon whose underlying mechanism remains undefined.[229]

An alternative to QPI tracking of individual particles is phase correlation imaging. This method measures the temporal decorrelation time of QPI collected data based on fluctuations

https://doi.org/10.1021/acsnano.1c11507
ACS Nano XXXX, XXX, XXX−XXX

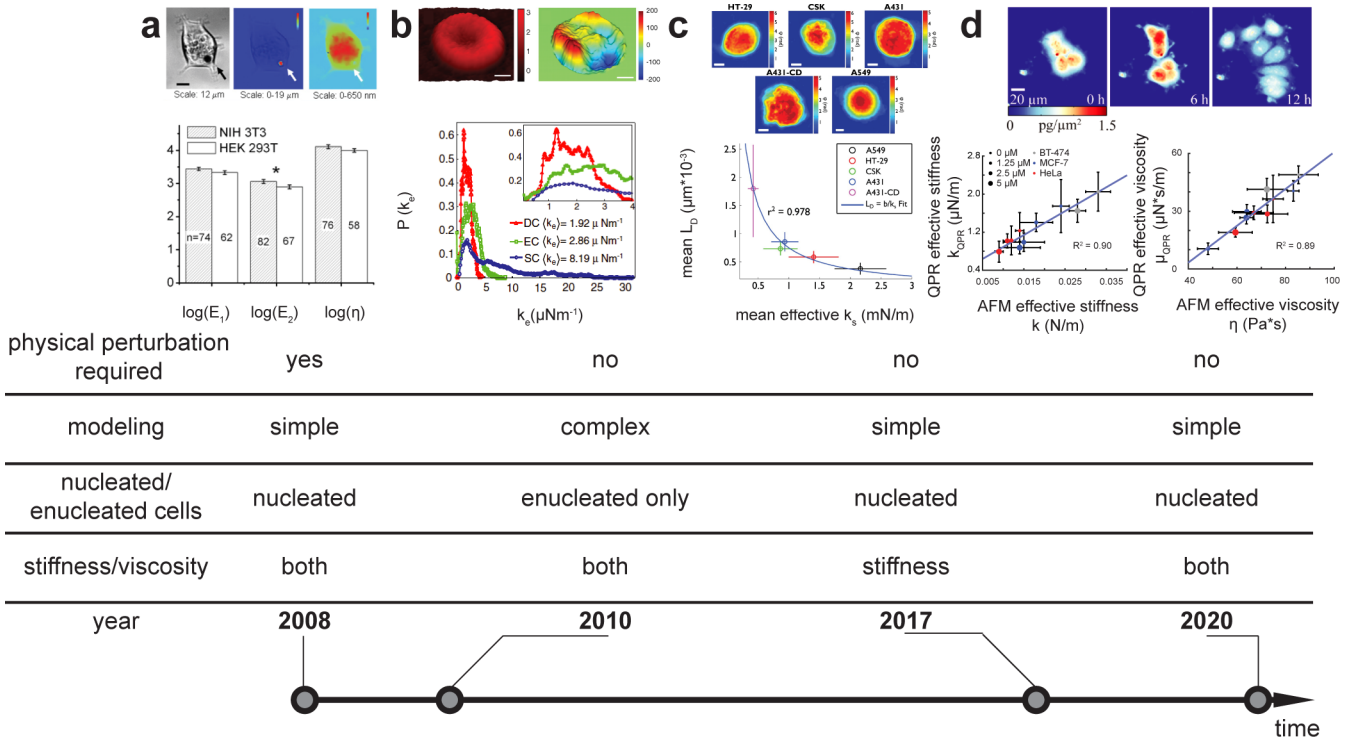

Figure 4. QPI biomechanics measurement evolution. (a) Early QPI biomechanical analyses required physical perturbations, such as actuation of a magnetic bead indenter on NIH3T3 fibroblasts (top) or HeLa carcinoma cells to extract Young's modulus (*E*; bottom). Adapted with permission from ref 244. Copyright 2008 IOP Publishing Ltd. (b) Detailed mechanical modeling from contactless measurements of biomechanical properties of red blood cells (RBCs; top left) using natural fluctuations in phase caused by membrane motion (top right) captures mechanical property variations (bottom) for populations of normal (DC), spiculated (EC), and spherical (SC) shaped RBCs. Adapted with permission from ref 246. Copyright 2010 National Academy of Sciences, U.S.A. Scale bar = 1.5 μm. (c) QPI phase (top-middle) of more complex cells HT-29 wild-type and shRNA (top left), HT-29 with CSK shRNA-mediated knock down (top middle), A431 epidermoid carcinoma control (top right) and cytochalasin D treated A431 (middle left) cells, and A549 lung adenocarcinoma cells (middle right) used to compute a mean phase disorder strength, related to intracellular cytoskeletal structure and independent measurements of shear stiffness (bottom). Adapted with permission from ref 247. Copyright 2017 Elsevier. (d) Time lapse QPI data (top) showing the redistribution of mass within single cells and cell clusters, which provides both resistance to deformation and decay terms. These terms were validated by comparisons with AFM measurements of stiffness (bottom left) and viscosity (bottom right) for MCF-7 and BT-474 breast carcinoma cells, and for HeLa endocervical carcinoma cells, treated with different concentrations of cytochalasin B. Adapted with permission under Creative Commons Attribution (CC BY) license from ref 250. Copyright 2020 Springer Nature.

of cell refractive index as an indicator of intracellular mass transport. A549 lung carcinoma cells were imaged using SLIM and treated with an actin polymerization inhibitor, cytochalasin-D, which showed only small local effects, but also uncovered a distribution of correlation times that is qualitatively different for quiescent and senescent cells, without cell labeling, providing a creative method for identifying quiescent versus senescent cells within a cell population.[230] Another application of phase correlation imaging revealed that intracellular mass transport rates were significantly different for osteoblast cells with different levels of migratory capacity.[231] Studies of aggressive, highly metastatic HeLa cells using SLIM and dispersion-relation phase spectroscopy revealed that mass transport in the cytoplasm was mainly active (ballistic, directed), compared to the nucleus which showed active and passive (diffusive) components, with faster mass transport in the cytoplasm than the nucleus.[232]

Applications of QPI to Cell Migration Assays. QPI provides a label-free alternative method to DIC or phase contrast microscopy for conventional cell motility or wound healing assays. An advantage of QPI in this application is that it additionally captures quantitative information on other cell features. For example, a commercially available digital holographic cytometry version of QPI was equipped with semiautomated image acquisition, segmentation, and analysis software. Measurements of melanoma cell motility and metastatic potential were highly accurate in a comparison with field-standard measures of wound healing, transwell migration, and invasion assays, with the added benefits of identifying rare hypermotile metastatic cells and an ability to distinguish motility from cell division associated cell displacement.[233] Measurements of cell mass and morphology with the same system could similarly track kinetic epithelial-to-mesenchymal cell transitions in heterogeneous cultures.[234] Finally, optical diffraction tomography, a 3D, label-free QPI-based imaging method, was used to study and quantify the dynamics of NIH3T3 cell migration in a wound healing assay, revealing single cell resolution of subcellular structure behavior and transport that underlies the mechanisms involved in gap closure and closure rate, with potential implications for pharmaceuticals development or repurposing.[235]

Applications of QPI for Measuring Biophysical Cell Properties. QPI can measure the distribution of mass within a cell, including mass due to structural elements such as the cytoskeleton, and how this distribution changes over time. It is, therefore, possible to extract information about the biophysical

https://doi.org/10.1021/acsnano.1c11507
ACS Nano XXXX, XXX, XXX−XXX

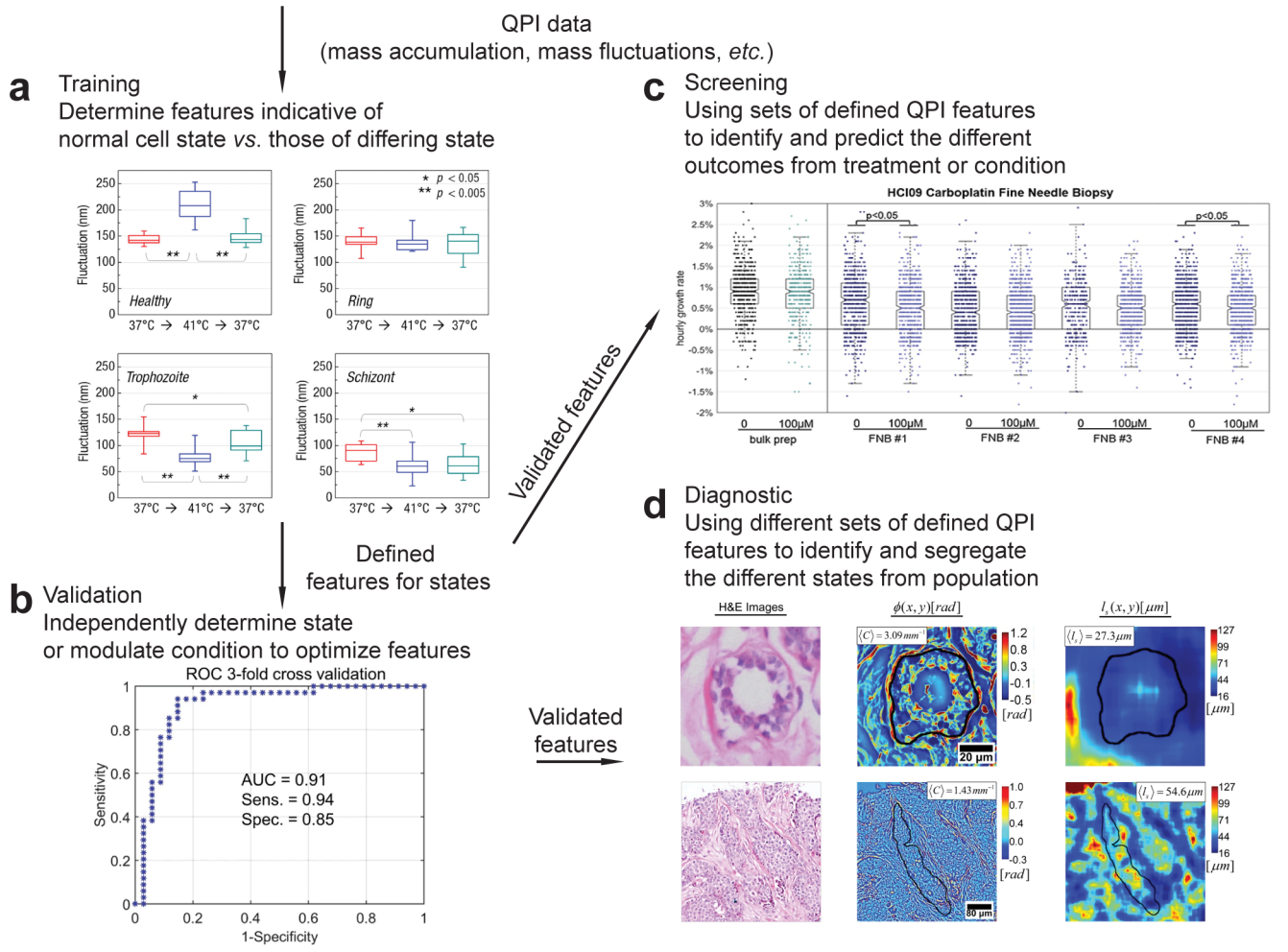

Figure 5. Progress toward QPI clinical applications as a screening and selection tool for treatments, and as a diagnostic tool to identify healthy versus diseased states. (a) Specific QPI features can identify disease or changes from a healthy or control state. For example, QPI measured differences in RBC membrane fluctuations at 37 and 41 °C *in vitro* can distinguish between healthy and ring, trophozoite, or schizont diseased states with *P. falciparum* parasitic infection. Adapted with permission from ref 261. Copyright 2008 National Academy of Sciences, U.S.A. (b) Once QPI features of interest are identified, validation is sought with an independent, orthogonal method, if available. For example, shown here is an area under the curve (AUC) or receiver operating characteristic (ROC) plot of the true positive (sensitivity) versus false positive (specificity) rate determining malignance from hematoxylin and eosin counter-stained tissue biopsy. This previously validated method is used to validate QPI determined malignant state for breast tissue biopsies. Adapted with permission under Creative Commons Attribution (CC BY) license from ref 267. Copyright 2018 Springer Nature. (c) Validation of a QPI measured feature in a specific context can broaden its utility. For example, validation of QPI measured changes in growth rate was successfully applied to identify effective treatments from a pool of candidate agents against carboplatin-resistant, patient-derived xenograft HCI09 breast carcinoma cells. Adapted with permission under Creative Commons Attribution (CC BY) license from ref 253. Copyright 2019 Elsevier. (d) Example of QPI as a diagnostic tool, with spatial light interference microscopy (SLIM; middle and right columns) identification of benign (top row) versus malignant (bottom row) glandular tissue, validated by pathological classification of hematoxylin and eosin stained biopsy material (left column). Adapted with permission under Creative Commons Attribution (CC BY) license from ref 267. Copyright 2018 Springer Nature.

properties of single cells,[230−232] such as effective cell stiffness and cell viscosity, from QPI data. These viscoelastic properties, in turn, underlie cell structure, movement, and function and have increasingly served as biomarkers for diseases,[236] cell states,[237] and biological transitions.[238] A standard method for measuring cell viscous and elastic properties is to examine stiffness and elastic, dissipative responses to an applied stress. Numerous physically interactive methods have evolved to make such measurements, including by cell deformation using an AFM,[239,240] or by using external and intracellular introduced probes, as in particle tracking microrheology.[240−242] The use of probes[243] and applied stress,[244] however, can affect cell behavior and impact measurements of cell viscoelasticity. Thus, the use of noninteractive techniques, such as those based on QPI, could circumvent or at least minimize these potential confounding influences.

QPI measurements of viscoelasticity divide into two main categories: (1) static measurements based on the spatial distribution and structure of mass within cells, including the cell cytoskeleton, and (2) dynamic measurements of changing cell mass distributions based on the temporal redistribution of mass. Early QPI dynamic measurements of viscoelasticity utilized sustained and rhythmic, temporal actuation and relaxation of magnetic beads as a form of spherical indenter, to induce local, transmitted stress on fibroblasts and observe the resulting mass redistribution and cell stiffening over time.[35] Actuated magnetic beads and QPI measurements also probed different cell types with and without cytoskeletal disruptions[244]

https://doi.org/10.1021/acsnano.1c11507
ACS Nano XXXX, XXX, XXX−XXX

(Figure 4a), whereas an optical stretching method was also applied in conjunction with DHM to examine differentiating bone marrow precursor cells for changes in subcellular structure and refractive index.[245] A key disadvantage in these studies, however, is that they required the use of non-native probes. By contrast, probe-independent, noncontact studies of RBCs used QPI to measure fluctuations in cell shape, coupled to a mechanical model of the relatively simple discoid structure of RBCs. This method was then used to quantify changes in RBC membrane shear, area, and bending moduli during transitions from discoid to abnormal echinocyte and spherical shapes, with potential implications for circulation and oxygen delivery to tissues[246] (Figure 4b). However, this method requires a mechanical model, which in this case is limited to enucleated RBCs. More recent noncontact studies linked static QPI measurements of mass distribution in nucleated cells to spatial disorder strength, a measure of mass organization within cells including the cytoskeleton (Figures 4c), to HT-29 colon cancer cell shear stiffness[247] and the elastic moduli of two breast cancer cell lines (MCF-7 and BT-474 cells)[248] as well as observe changes in the cell cytoskeleton under applied electrical fields.[249] Dynamic QPI measurements of mass redistribution rates for MCF-7, BT-474, and HeLa cells quantified both cell stiffness and elastic moduli during growth (Figure 4d) and during an epithelial-to-mesenchymal cell state transition.[250] Combined, these and future studies suggest a powerful and emerging opportunity for QPI to quantify cellular biophysical and biomechanical properties that traditional biochemical, molecular, and cell biology measurements alone cannot provide.

QPI Applications in Screening and Drug Sensitivity Measurement. There are a growing number of emerging applications for QPI in clinical studies for which quantitative and label-free measurements of individual cells and cell clusters provides significant advantages. Current work is mainly at the level of technology development, applications and validation stages (Figure 5). QPI properties such can be used to categorize specific cellular states (Figure 5a) and are validated (Figure 5b) to determine viability in screening for these states. One major direction under development for QPI screening is measurements of cell dry mass changes in response to therapeutic agents (Figure 5c). Changes in dry cell mass detected by QPI has been used to measure single tumor cell sensitivity to cancer therapeutics.[251] The range of applications shown includes evaluating mitotic inhibitors with different mechanisms of action,[252] examining the rate and extent of cancer cell escape and regrowth following senescence induction,[253] and uncovering the response heterogeneity of a mixed sensitive and resistant cancer cell population to specific drug treatment.[85] Because QPI can track the kinetics of dry mass growth responses of individual cells or clusters of cells within large populations of cells over time, heterogeneous cell responses to therapeutics are readily identified. For example, rare drug-resistant diffuse large B cell lymphoma (DLBCL) cells within a population of DLBCL cells sensitive to a PI3-kinase inhibitor, idelalisib, were identifiable by continued mass accumulation and could, in concept, be isolated and recovered for further studies[85,251,254] Preclinical dry mass accumulation rate studies using patient derived xenografts predicted drug sensitivity for triple negative breast cancers, providing a potential QPI application for drug selection in personalized oncology[253,255] (Figure 5c). A separate drug screening in breast cancer study applied QPI to capture drug sensitivity that was consistent with findings from current standard approaches, as well as multiple additional physiologically relevant parameters that characterized cell responses to therapy.[256] As discussed above, QPI measured viscoelasticity can differentiate between epithelial and mesenchymal states,[250] a state transition that is a cardinal feature of cancer cell metastasis, and phase correlation imaging discriminated between quiescent and senescent cells, with potential implications for drug resistance and tumor reemergence.[230]

QPI Morphological Applications in Diagnostics. Measurements of cell morphologies and disease states provides another emerging clinical application of QPI (Figures 5a,d). Anatomic pathologists have long used changes in cellular morphology and tissue architecture to diagnose disease, as changes in morphology represent changes in cell state and function, for example, plasma membrane blebs can indicate dynamic cytoskeleton-regulated cell protrusions in apoptosis, cytokinesis, and cell movement.[257] Accordingly, diagnostic applications of QPI focus on cell state to provide a diagnostic tool with early attempts using features from QPI images to screen for cancerous tissue.[258] QPI tissue spatial correlation, a measure of refractive index map correlation length that may represent nanoscale cell morphology in fixed tissue samples, provided a biomarker that distinguished between malignant and benign breast cancer biopsy samples.[259] When combined with dry mass measurements, QPI identified and classified different kinetic states for a population of melanoma cells in culture.[260] In applications with RBCs, morphology studies using QPI identified *Plasmodium falciparum* infection of RBCs[261] and suggested the possibility that QPI measurements of cell membrane dynamics could identify additional pathologies that cause or accompany other human diseases[260,261] (Figure 5a). QPI using white light interferograms with red, green and blue wavelengths separated electronically helped determine morphological features of RBCs,[262] as did using DHM with data clustering and discriminant analysis.[263] "Real-time" QPI measurements of blood samples have been demonstrated, utilizing parallel computing strategies to calculate diagnostically relevant cell parameters without storing phase images, allowing for smaller electronic storage and data transmission requirements, which could benefit remote diagnoses of RBC diseases.[264] QPI has also been used to measure morphology changes in *HTori* thyroid cells during treatment with plasma from a nanosecond dielectric barrier discharge,[265] changes in macrophages from chemically induced apoptosis and dynamic phagocytosis,[201] and for sperm selection for bovine *in vitro* fertilization.[266] SLIM and tissue spatial correlation analysis was used to assess breast cancer fixed tissue microarrays and showed a 94% sensitivity and 85% specificity for cancer detection[267] (Figure 5d), independent of tissue staining quality.

ONGOING DEVELOPMENTS

Quantitative Phase Tomography. The transition from generating 2D quantitative phase images to tomographic images that capture the 3D structure of specimens is an ongoing development in QPI. While 3D imaging is fairly common with fluorescent biomarkers using confocal or widefield microscopy and digital image processing reconstruction,[268] the use of fluorescence tags has disadvantages that include photobleaching and phototoxicity with increased imaging time.[269] Imaging based on the inherent contrast provided by natural variation in refractive index eliminates

https://doi.org/10.1021/acsnano.1c11507
ACS Nano XXXX, XXX, XXX−XXX

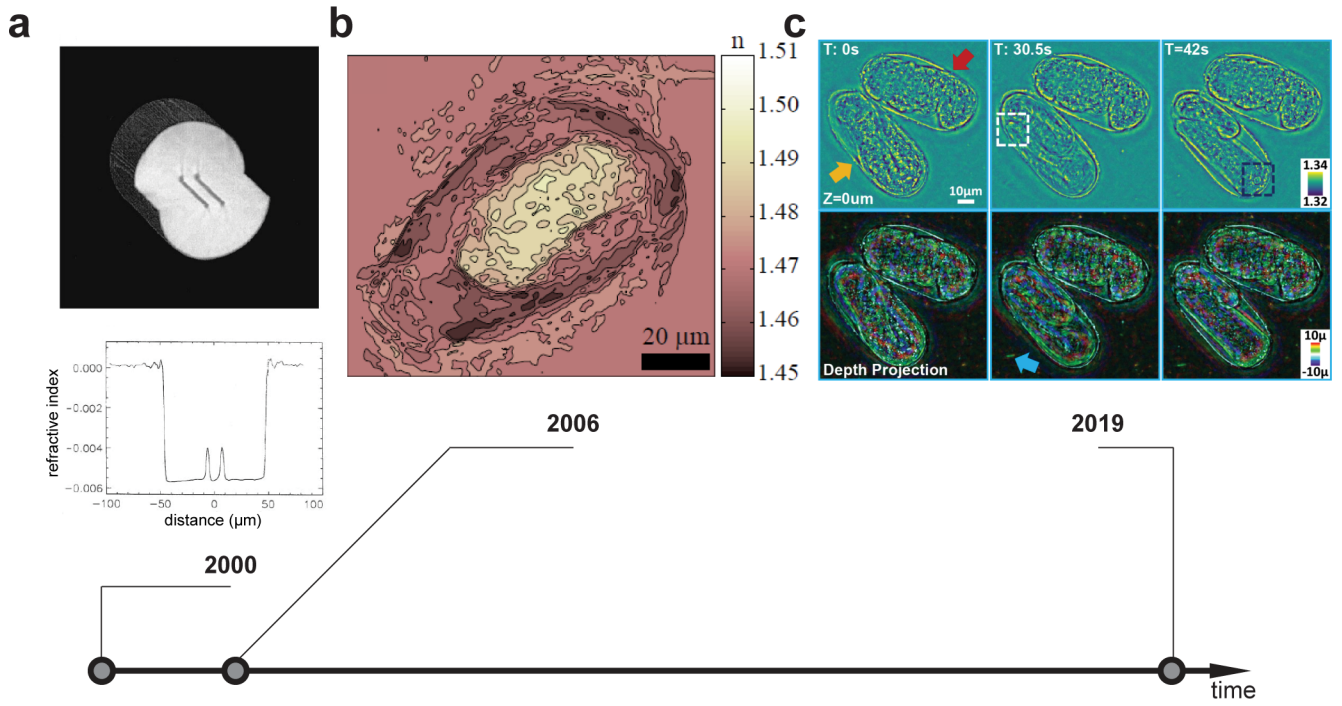

Figure 6. Progress in QPI tomography from applications with static optical fibers to multicellular organisms. (a) QPI tomography analysis of cross sections of optical fibers (top). A common feature of QPI tomography is recovery of the 3D refractive index distribution, rather than the integrated refractive index through the sample thickness, as in 2D QPI. This is shown by the refractive index distribution measured as a line profile through the sample (bottom). Reproduced from ref 275. Copyright 2000 Elsevier. (b) QPI tomography of single cell protozoan, *Hyalosphenia papilio*, with refractive index reconstructions shown as different 2D slices. Adapted from ref 276. Copyright 2006 The Optical Society. (c) Multiplexed intensity diffraction tomography of multicellular *Caenorhabditis elegans* embryos. Shown are in-focus refractive index (top row) and depth-coded projections of volumetric reconstruction (bottom row). Red and orange arrows indicate developmental stages of the embryos. Individual developing tissues, the buccal cavity (white box), intestine (blue box), and native bacteria (blue arrow), are visible. Reproduced with permission from ref 279. Copyright 2019 The Optical Society.

these label-related problems. Tomography refers to the stacking of 2D planes or images acquired at multiple imaging angles to reconstruct 3D structures of specimens called tomographs. Although the principle of interferometric tomography was proposed in the 1960s[270] and experimentally demonstrated in the 1980s,[271] tomographic image reconstruction was too computationally intensive to be routinely used for QPI until decades later.[272] Reconstruction of quantitative phase tomography from scattering images of polystyrene beads using Mach−Zehnder interferometry,[273] and then polystyrene foam from DHM images was demonstrated,[274] followed by measurements of the 3D refractive index and the absorbance profile of optical fibers using phase retrieval and tomographic reconstruction[275] (Figure 6a).

Whereas 2D QPI measures the integral of Δn, the refractive index of the sample relative to the surrounding media through the thickness of the sample in each imaging pixel, quantitative phase tomography maps Δn within each voxel. Advances in tomography have focused on increased precision and accuracy of 3D refractive index mapping using DHM assisted tomography[276] (Figure 6b). Tomography has also been developed from phase shifting interferometry,[277] and light-emitting diode (LED) array microscopy, which forms the basis of DPC phase reconstruction.[98,278] LED array systems are capable of an impressive 0.25 s acquisition time, made possible with optimized sample illumination[279] (Figure 6c). Another method for acquiring tomographic images for use in image reconstruction is by acquisition of holographic phase images at a series of angular projections using illumination with a rotating fiber optic, resulting in a 1 Hz imaging rate.[280] Further advances in this direction also enable high resolution image reconstruction using low numerical aperture intensity images as an alternative method.[281] Intensity diffraction tomography using annular LED illumination has improved imaging speed and achieved diffraction limited resolution as well.[282]

A promising application of tomographic QPI to measure subcellular structures is the interrogation of biomolecular condensates, which are membrane-less organelles or organelle subdomains that have been implicated in a wide range of cell behaviors including bone metastasis[283] and autophagy.[284] This process of intracellular phase separation was examined by 3D QPI with identification confirmed by fluorescence.[285] Future applications of QPI tomography includes combinations with other QPI data analysis methods to reveal the essential biological mechanism(s) behind these structures. Another promising application of QPI tomography is the measurement of mass within multicellular specimens, such as whole animals[277] (see *in vivo* section, below), or 3D organoids that are often used as *in vitro* models of development or disease.[286] Gradient light interference microscopy developed by combining aspects of DHM, DIC microscopy and low coherence interferometry enables 3D imaging of samples ranging from single cells to intact embryos for measurements of internal structures and their evolution in time.[287] Optical projection tomography uses DHM and analyzes movies of flowing samples to acquire images at multiple angles, resulting in reduced imaging time and a noninvasive solution for phase measurements of RBC aggregation,[288] an offshoot of which is

https://doi.org/10.1021/acsnano.1c11507
ACS Nano XXXX, XXX, XXX−XXX

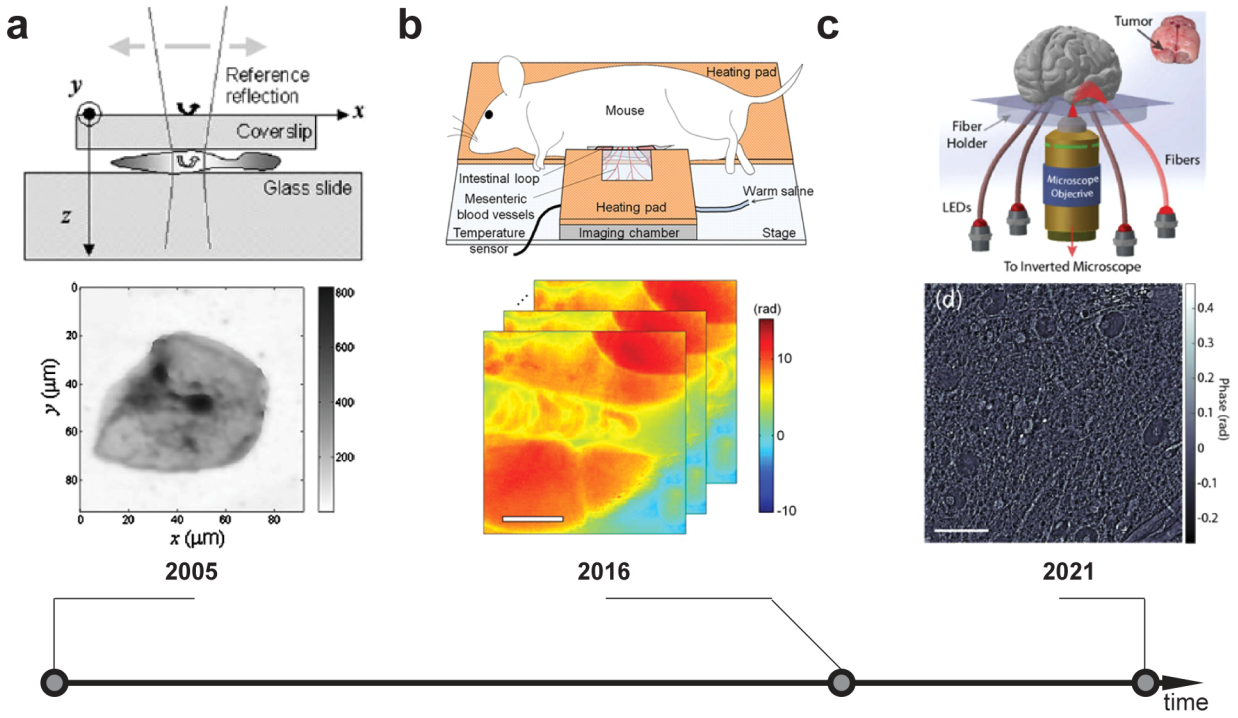

Figure 7. Progression of *in vivo* QPI approaches. (a) Sample preparation for an *in vivo* technique called spectral-domain optical coherence phase microscopy (SD-OCPM; top) which generated optical path difference maps for human epithelial check cells (bottom). Adapted from ref 294. Copyright 2005 The Optical Society). (b) Diagram of live mouse heating stage setup for *in vivo* QPI (top). Representative QPI data from a live mouse mesentery showing mouse microvasculature represented as optical phase delay maps reconstructed from holograms (bottom). Adapted with permission under Creative Commons Attribution (CC BY) license from ref 298 . Copyright 2016 Springer Nature. Scale bar = 10 μm. (c) Schematic of a fiber-based quantitative oblique back-illumination microscopy (qOBM) platform for imaging tumor tissue in excised rat brain (top), thereby generating QPI images from deconvolution of intensity images (bottom). Adapted from ref 301 . Copyright 2021 The Optical Society. Scale bar = 50 μm.

called limited-angle holographic tomography. White light diffraction tomography performed by deconvolution of QPI stacks generates high-resolution QPI data of intracellular structures.[220] Quantitative oblique back-illumination microscopy (qOBM) enables tomography of a wide range of samples, from thick highly scattering[286] to opaque[289] samples, by using multiple scattering paths generated within the sample to create an effective light source deep within the sample despite illuminating the sample in epi-mode. Overall, these selected example applications and approaches in quantitative phase tomography show that the ability to view and quantify sample features in 3D is very powerful with further studies codifying metrics for comparison.[290] Since quantitative phase tomography is another QPI approach that relies heavily on computation for generating and processing 3D data, this area will continue to benefit from ongoing advances in computing power and analytic software.

QPI in Tissues and *In Vivo*. There are ongoing efforts to apply QPI to tissue slices and the *in vivo* environment to limit the confounding effects of studying cell behavior *in vitro* (Figure 7). However, there exist several roadblocks to fully realizing this goal, including light scattering of thick samples, phase unwrapping errors due to long optical path lengths through thick tissues, and the small size of microscopes needed for imaging inside living organisms. One approach is to continue modifying techniques that have already been adapted for *in vivo* imaging for phase retrieval. A key example of this approach is the use of optical coherence tomography (OCT). OCT and its' high speed variants[291] are low-coherence interferometry methods that leverage low temporal coherence to exclude scattered light outside a tissue slice of interest, coupled with backscattering of light, to image cross-sectional areas of tissues *in situ*.[292,293] An early approach added phase retrieval to OCT to enable QPI of human cheek cells[294] (Figure 7a) and isolated chicken cardiomyocytes.[295] Phase-sensitive OCT has also been extended into *in vivo* imaging of the human retina[296] and its associated motion.[297] However, despite great improvements in phase stability, there is a still often a need for either manual or automatic phase unwrapping to correct for phase errors with this emerging technique.

The most definitive application of *in vivo* QPI has been DHM imaging of red blood cells (RBCs) in microcapillaries within the mesentery of live mice[298] (Figure 7b). By using 2D holograms from different angles, Sung *et al.* was able to reconstruct a 3D tomogram via optical diffraction tomography.[299] This method of *in vivo* QPI however is constrained to areas that are sufficiently thin or near the surface of the animal. Another adaptive approach is to use QPI methods developed in an *in vitro* setting to address issues of light scattering in thick samples and phase unwrapping and then translate them for *in vivo* imaging through miniaturization. This has led to attempts to miniaturize certain platforms, such as diffraction phase microscopy (DPM), into an endoscope (i.e., eDPM),[300] or to making a fiber optics based qOBM system.[301] Demonstrations of these techniques have so far been limited to *ex vivo* imaging. The eDPM system has been used to measure stained white blood cells[300] and a similar holographic endoscope method was applied to mouse esophageal tumor samples,[302] whereas

https://doi.org/10.1021/acsnano.1c11507
ACS Nano XXXX, XXX, XXX−XXX

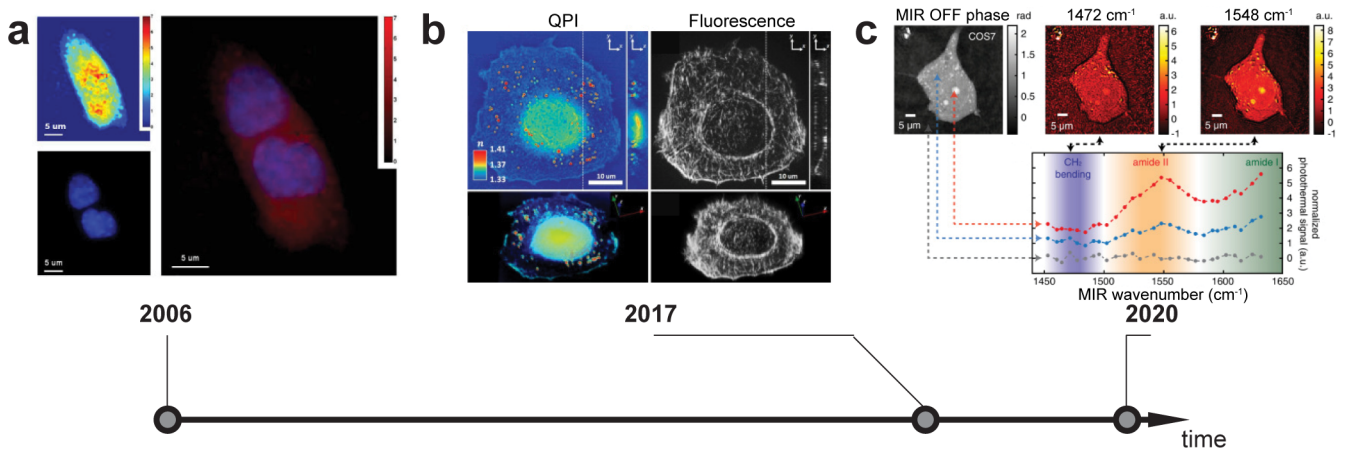

Figure 8. Examples of the opportunities available from coupling QPI with additional imaging modalities. (a) QPI of kidney cells paired with fluorescence detection enables the identification and quantification of dry mass changes, represented by phase shifts, within subcellular regions (right), such as the nucleus, identified by Hoechst staining (bottom left). Reproduced with permission from ref 303. Copyright 2006 The Optical Society. (b) Enhanced fast image acquisition of dual 3D fluorescence (top right) and refractive index measurements from tomographic QPI (top left). This accelerated approach provides the necessary capture speed in image scanning to reconstruct 3D tomograms of A549 cells for both fluorescence (bottom right) and QPI (bottom left) measurements from z-step data Adapted with permission from ref 310. Copyright 2017 The Optical Society. (c) Molecular vibrational spectroscopy paired with QPI of COS7 cells (top left) examined for molecular signatures, such as CH_2 (top center) and peptide bending (top left), corresponding to subcellular phase shifts within the nucleus (orange), cytoplasm (blue), relative to empty space control (gray) (bottom). Reproduced with permission from ref 311. Copyright 2020 The Optical Society. .

the fiber optics qOBM imaging system has examined gliosarcoma cells from excised and formalin-fixed rat brain tissue[301] (Figure 7c). Overall, work so far in this area points toward a bright future of applying various *in vitro* quantitative phase approaches to studies of mass regulation, biophysics, and the building of diagnostics based on QPI measurements of cells *in vivo*.

Multimodality Approaches. A key advantage of QPI is that it is label-free and captures data on all components that contribute to cell mass. However, a related limitation is that QPI data are not specific for any individual component of the cell. Therefore, a number of approaches and studies have combined QPI with other imaging modalities to learn more about cell structure and behavior (Figure 8). Two of the most promising connections are the combination of QPI with fluorescence detection through the tagging of specific molecules and the combination of QPI with vibrational spectroscopy, for label-free measurements of chemical composition within the cell.

Early combinations of fluorescence detection methods with QPI approaches[303] (Figure 8a) to interrogate RBCs measured physical and optical thickness,[304] resolved substructures within cells,[305] and identified and characterized the mass distribution of subcellular components[303,306] (Figure 8). These initial approaches demonstrated QPI identification and measurement of different subcellular components within a cell that were manipulated to fluoresce. Fluorescence combined with QPI has also been used to segregate different populations of cells in a mixed culture experiment,[85] track the behavior of rare subpopulations of primary human cells *ex vivo*,[204] or to determine different cell states[250] concurrently with mass accumulation and mass density measurements from niche cell populations. Dual fluorescence plus QPI combinations have also enabled biomechanical interrogations of cell responses to optical tweezers[307] and dual traction force and growth measurements.[308] The combination of SLIM and an epifluorescence traction stress imaging method, Hilbert phase dynamometry,[309] was used to study mesenchymal stem cell growth and differentiation into osteocytes and adipocytes. Results showed that during osteogenesis and adipogenesis, greater force is exerted by these cell types on their growth substrates than by mesenchymal stem cells, which develop the least force and show the lowest growth rate.[308]

In general, combined 3D QPI/3D fluorescence techniques can differentiate subcellular components while rendering a map of cell refractive index[312] and identifying the refractive index of subcellular regions.[313] Combined 3D fluorescence detection and refractive index tomography on cells with fluorescently labeled nuclei, mitochondria, and actin enabled registration of the refractive index profile with the labeled subcellular components.[314] Optical diffraction tomography has also been used in combination with 2D fluorescence to validate measurements of lipid content.[312] Moving toward the acquisition of functional data from 3D structure, studies using combinations of refractive index tomography with fluorescence subdiffraction microscopy enable concurrent studies of cell biophysical properties and biochemical functions.[305,310] Further advances include high-speed correlative 3D QPI/3D fluorescence techniques[310] (Figure 8b), which have evolved to enable 200 Hz imaging of 4D maps of cell structures.[315] With the addition of machine learning, more advances are possible due to the vast amount of morphological and molecular data collected by dual fluorescence QPI combination modalities, thereby enabling more complex analyses.

Another multimodal approach of interest is the combination of QPI with molecular vibrational spectroscopy to measure chemical composition[311] (Figure 8c). Extracting chemical composition from QPI alone has been attempted as quantitative phase spectroscopy (QPS), but with limited success. QPS uses phase measurements over a range of wavelengths to estimate the component distributions in samples. This approach has been applied to measure hemoglobin[316] or BSA[317] concentrations in solution, and has

https://doi.org/10.1021/acsnano.1c11507
ACS Nano XXXX, XXX, XXX−XXX

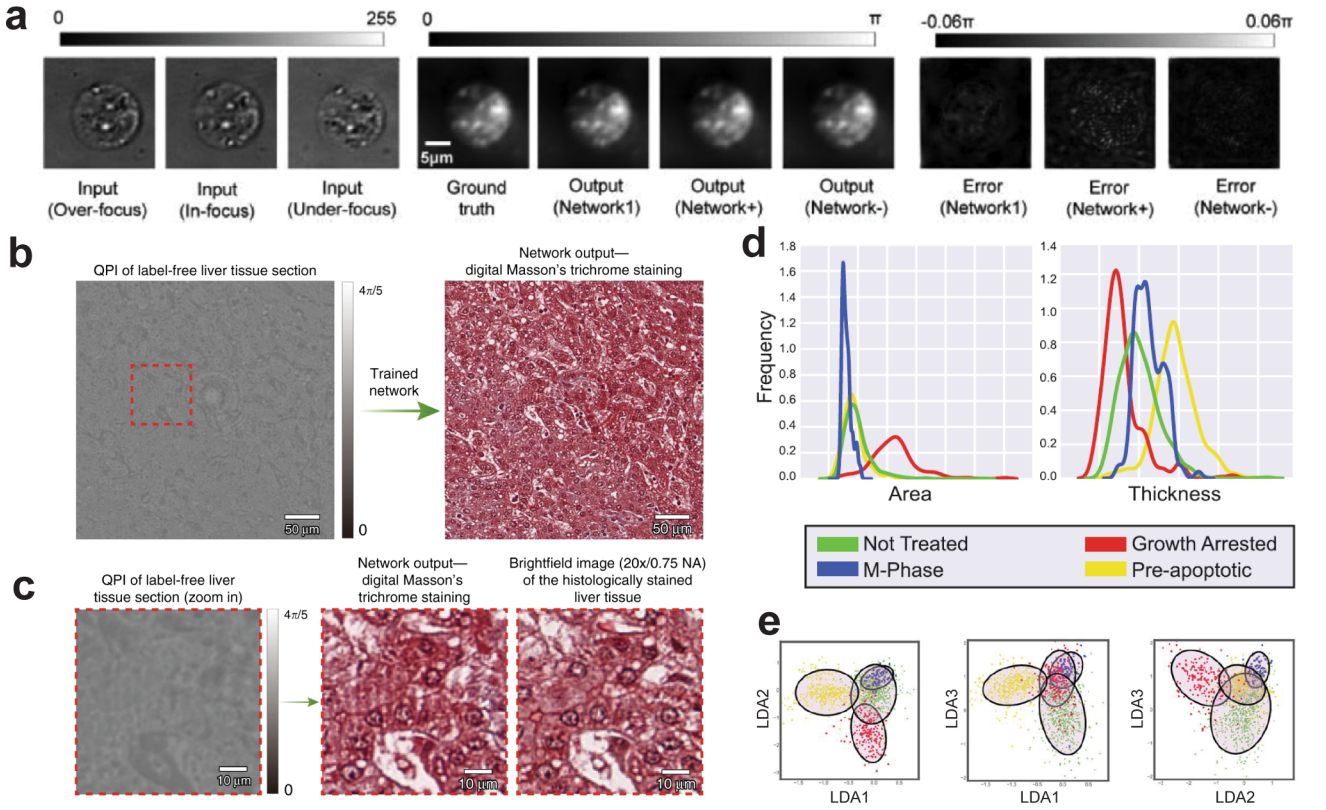

Figure 9. Machine learning has been applied to all three stages of a typical QPI processing and analysis pipeline: (1) computation of phase data, (2) labeling of phase images, and (3) feature-based cell classification. (a) Phase image reconstruction from a single overfocus or under-focus image using deep learning and TIE algorithm. The error of phase calculation using the combined deep learning TIE method is under 0.06 π for the 'Network+' learning-based method using one overfocus image and the 'Network-' method using an under-focus image when compared to the ground truth calculated from three images using TIE. Reproduced with permission from ref 123. Copyright 2020 Elsevier. (b) PhaseStain is a digital staining method developed using deep learning on holographic microscopy images, to perform virtual staining of tissues from label-free QPI images. The stained images produced are similar to histological staining observed under a brightfield microscope. (c) A zoomed-in view comparing the liver tissue section stained using PhaseStain and Masson's trichrome staining. Reproduced with permission under Creative Commons Attribution (CC BY) license from ref 338. Copyright 2019 Nature. (d, e) Machine learning to classify cell states during the epithelial-to-mesenchymal transition (EMT). M-phase, pro-apoptotic, and growth-arrested cell states occurring during EMT can be distinguished from untreated control cells using machine learning, utilizing cell features identified from QPI. Reproduced with permission under Creative Commons Attribution (CC BY) license from ref 260. Copyright 2017 Springer Nature.

been applied to measure healthy[317] and diseased[318] RBCs. This approach has also been extended to 3D tomography.[319] However, using this approach to decipher more complex cellular contents is limited by the relatively small variation in phase delay of biomolecules in visible light. Molecular vibrational spectroscopy techniques generate vibrational spectra of molecules measured from their linear absorption and inelastic light scattering.[320] These vibrational spectra are dependent on the chemical structure and environmental interactions of the molecules and thus can provide information on the chemical composition of materials. Raman spectroscopy, which is a type of vibrational spectroscopy, relies upon the inelastic scattering of photons to determine the vibrational modes of molecules, allowing for the detailed identification of chemical composition. However, use of scattering spectroscopy methods may generate an issue with limited signal in applications with live cells. Overcoming this limitation typically requires either high illumination power, which induces phototoxicity, or metal probes for surface enhanced Raman, which can foul in solution environments. Nonetheless, label-free identification of chemical compositions within cells is an ideal complement to the less specific biomass information obtained with QPI.

Dual modality QPI plus molecular vibrational spectroscopy has been applied with a mid-infrared light source to characterize specific molecular contents with cellular mass distributions.[311] Raman spectroscopy has been applied to characterize both the morphological dry mass and chemical composition within cells.[321] Combined Raman QPI approaches have also examined dry mass, mass density, and protein and lipid composition under ultraviolet radiation,[322] and with the help of machine learning classified normal and cancerous tissues.[323] Combining QPI with molecular vibrational spectroscopy enables the examination of chemical composition and biomass kinetics (Figure 8c) to further dissect core biological mechanisms and processes.

Brillouin microscopy is a noninvasive, label-free microscopy method to measure viscoelastic properties of cells and tissues[324] that has also been combined with QPI. Brillouin microscopy uses inelastic scattering to determine the viscoelasticity of heterogeneous materials of known density and refractive index. Brillouin microscopy was combined with optical coherence tomography to study biomechanical properties in tissues, including stiffness, elasticity and structural changes in embryos.[325,326] Brillouin microscopy has also been combined with optical diffraction tomography and fluores-

https://doi.org/10.1021/acsnano.1c11507
ACS Nano XXXX, XXX, XXX−XXX

cence microscopy to measure the refractive index, density and elasticity of specific fluorescently labeled structures inside cells.[327] QPI Brillouin approaches have also been used to measure cell softening during transmigration.[328]

As a label-free method based on brightfield microscopy, QPI can be added to other microscope imaging modalities beyond fluorescence and vibrational imaging methods. For example, quantitative label-free imaging with phase and polarization, a combination of defocused QPI and polarization microscopy, can measure volumetric phase, retardance and orientation, which is useful for studying structures in cells and tissue slices.[329] There is, therefore, a broad potential future for multimodality work in biological and potential clinical applications of QPI.

Machine Learning. Machine learning has propelled many recent advances in QPI, such as improving phase reconstruction for QPI images, improving segmentation and tracking for processing QPI data, and improving data labeling and classification (Figure 9). In terms of preprocessing, machine learning can help improve the reliability of phase reconstruction algorithms. Most work applying machine learning to QPI uses convolution neural network (CNN) variants, such as U-Net.[330] CNN is well suited for phase recovery as it considers multiple pixels in the process of data condensation, unlike perceptron models that use individual pixel input.[331] For example, in the area of phase retrieval, machine learning has been used to reconstruct TIE results with a single intensity image, and can eliminate errors arising at the boundaries of images during TIE reconstructions as well as reduce the impact of noise.[123] Machine learning can also benefit wavefront sensing.[331,332] For example, a diffuser can be used to generate random speckles that then work as a wavefront sensor, when combined with a neural network trained on phase objects.[333] Phase unwrapping is often an issue in interferometric methods,[48] and a one-step correction for phase unwrapping errors has therefore been introduced using machine learning methods.[334] Holographic image reconstruction has also been performed from single intensity images using machine learning, with validation on pap smears and human tissue samples.[124]

Machine learning is also helpful in QPI data postprocessing steps. Here, CNNs are the most widely used approaches as well. Machine learning networks have been designed to segment microscope images,[335] and process cell tracking data, counting, and characterization.[336] Machine learning algorithms on unlabeled QPI images can compute or false-colorize staining patterns created by computer labeling of different organelles and components within cells. For example, machine learning can be used to identify lipid droplets in unlabeled QPI images.[337] A related machine learning approach, called PhaseStain, was developed for label-free staining of QPI images.[338] This method was extended for real-time staining and classification of sperm cells,[339] identification of cells from subcellular components,[340] and generation of pseudofluorescence images from label-free QPI data.[338,341] The change in dry mass of subcellular structures has been measured over time using phase imaging with computational specificity, which segments QPI data with machine learning approaches.[342]

One especially promising application of machine learning methods for QPI studies is in the classification and identification of cells and tissues. Classification schemes using machine learning algorithms can help reduce the time and labor involved in traditional pathology, while the label-free nature of QPI simplifies data collection. Statistical classification from QPI data was demonstrated using basic feature recognition algorithms for the classification of microorganisms.[343,344] Similar classification schemes were later improved using machine learning approaches.[345,346] Machine learning has since been used with QPI data for classifying specific cell death pathways;[347] categorizing the health and quality of human spermatozoa for *in vitro* fertilization;[348,349] screening RBCs for hematologic disorders[350,351] including sickle cell disease[352] and malaria;[353] and identifying and classifying microorganisms.[354] In cancer studies, machine learning has been applied to QPI data for scoring cancer cells as epithelial or mesenchymal in origin,[355] phenotypic profiling of cancer and noncancer cell lines,[356] as a diagnostic tool in pancreatic cancer,[357] and to quantify dynamic responses of melanoma cells to therapy[260] (Figure 9d,e). Machine learning with QPI in combination with data from additional techniques helps increase the accuracy of classification, as it increases the number of data inputs into selected classification methods. For example, QPI, fluorescence, and Raman spectroscopy have been combined as inputs into a machine learning algorithm to detect macrophage activation.[358] Raman imaging and QPI combined with machine learning has also been applied to recognize stages of B cell acute lymphoblastic leukemia.[359] Overall, machine learning is poised to play an ever-increasing role in both the generation and interpretation of QPI data, and has already touched upon nearly every major application of QPI.

CONCLUSIONS AND PERSPECTIVE

QPI is an approach with a long history. However, the last two decades have seen great leaps in both the abilities and applications of QPI. The rapid recent development of QPI is from impressive advances in image processing capabilities enabled by digitalization and increasing computational power (Figure 1a). This development and application of computational tools has substantially increased the utility and power of QPI in its application to biomedicine and permitted the development and commercialization of prebuilt and user-friendly QPI platforms. Consequently, recent years have witnessed a surging interest in QPI, coupled to a dramatic increase in QPI enabled publications and discoveries (Figure 1b). This marked expansion of QPI applications is also being fueled by leveraging machine learning approaches and is increasingly impacting areas that are beginning to include disease diagnoses and measurements of biological state transitions. While exciting, this recent and rapid adoption of QPI platforms and associated published studies has also highlighted the dearth of standardization tools and practices beyond the adaptation of polystyrene beads[143] as phase standards. Developing and circulating such tools will be critical for reproducible studies and validation of future QPI-based diagnostics and other applications.

Current areas of QPI utility include studies of cell size and its regulation, cellular diagnostics and screens, and biomechanics and biophysics. One key strength of QPI approaches includes label-free classification of key cellular behaviors such as programmed cell death pathways, differentiation, cell cycle progression, and immunological responses. Assessing these behaviors in the context of changes in biomass density, morphology, transport, and viscoelastic properties provides a deeper understanding of adaptations during cell or organismal life. A second key strength is the ability to study

https://doi.org/10.1021/acsnano.1c11507
ACS Nano XXXX, XXX, XXX−XXX

single cells or individual cell clusters over long periods of time. As techniques in single cell profiling continue development resulting in increasing reports on molecularly distinct subpopulations of cells, QPI provides a platform for assessing distinct phenotypes and behaviors within these heterogeneous populations. Further development of multimodal approaches will be critical for merging the observations made using single cell molecular profiling with QPI single cell phenotyping.

Finally, although there have been a large number of studies pointing toward clinical utility of QPI, this approach is ready for more robust validation and testing with clinical samples. As a label-free approach that can quantify multiple physiologically relevant parameters describing the behavior of living cells, QPI is well positioned to work with clinical samples. QPI therefore has the potential to enable a wide range of clinical applications in functional and diagnostic medicine, both as an addition to current approaches that rely on staining and as an independent *ex vivo* approach. Further work is therefore needed to build on the demonstrated capabilities of QPI to translate this technology to clinical utility and ultimately to improve the standard of patient care.

AUTHOR INFORMATION

Corresponding Authors

Michael A. Teitell − *Deparment of Bioengineering, Molecular Biology Institute, Broad Center for Regenerative Medicine and Stem Cell Research, California NanoSystems Institute, Deparment of Pathology and Laboratory Medicine, Department of Pediatrics, and Jonsson Comprehensive Cancer Center, David Geffen School of Medicine, University of California at Los Angeles, Los Angeles, California 90095, United States;* orcid.org/0000-0002-4495-8750; Email: mteitell@mednet.ucla.edu

Thomas A. Zangle − *Department of Chemical Engineering and Huntsman Cancer Institute, University of Utah, Salt Lake City, Utah 84112, United States;* orcid.org/0000-0001-5899-3517; Email: tzangle@chemeng.utah.edu

Authors

Thang L. Nguyen − *Deparment of Bioengineering, University of California at Los Angeles, Los Angeles, California 90095, United States;* orcid.org/0000-0002-9809-3836

Soorya Pradeep − *Department of Chemical Engineering, University of Utah, Salt Lake City, Utah 84112, United States*

Robert L. Judson-Torres − *Department of Dermatology and Huntsman Cancer Institute, University of Utah, Salt Lake City, Utah 84112, United States*

Jason Reed − *Department of Physics, Massey Cancer Center, and VCU Institute for Engineering and Medicine, Virginia Commonwealth University, Richmond, Virginia 23284, United States;* orcid.org/0000-0002-3314-8699

Complete contact information is available at: https://pubs.acs.org/10.1021/acsnano.1c11507

Author Contributions

#These authors contributed equally.

Funding

This work was supported by the Whitcome Predoctoral Training Program and the UCLA Molecular Biology Institute (T.L.N.), NIH grant CA246182, NIH-NCI Cancer Center Support grant P30 CA016059 and the C. Kenneth and Dianne Wright Center for Clinical and Translational Research (J.R.), the University of Utah Office of the Vice President for Research and the Office of the Assistant Secretary of Defense for Health Affairs through the Breast Cancer Research Program under award number W81XWH1910065 (T.A.Z.), and by NIH grants R21CA227480, R01GM114188, R01CA185189, and P30CA016042 (M.A.T.).

Notes

The authors declare no competing financial interest.

VOCABULARY

Phase (of light), Property that, along with amplitude (intensity), wavelength (color), and polarization, defines light as an electromagnetic wave. Shifts in phase occur from a delay in propagation speed, such as when light passes through a sample of higher refractive index; **Quantitative phase imaging (QPI)**, Method in which the phase shift of light as it interacts with matter is measured. This provides measurements of the integrated refractive index through a sample's optical thickness at each imaging pixel; **Interferometry**, Method in which source light is split into a sample and reference beam, then recombined at or before a detector, generating interference patterns. This method can be applied to acquire QPI data; **Digital holography**, Method in which a hologram is captured on a digital imaging sensor using an interferometer. The resulting digital hologram enables reconstruction of QPI data; **Wavefront sensing**, Method that measures aberrations in the wavefront of light due to the distribution of phase shifts caused by interaction with a sample, typically without the need for the reference beam used in interferometry; **Phase retrieval**, A class of methods in which intensity images, often with some perturbations such as partial defocusing, chromatic aberrations, or partial illumination, coupled with knowledge of the optical transfer function, enables reconstruction of the distribution of phase shifts through a sample; **Quantitative phase tomography**, Method to measure the three-dimensional distribution of phase shifts within a sample. Returns measurements of average refractive index within each imaging voxel.

REFERENCES

(1) Barer, R.; Joseph, S. Refractometry of Living Cells. *Q. J. Microsc. Sci.* **1954**, *s3*−*95* (32), 399.

(2) Zangle, T. A.; Teitell, M. A. Live-Cell Mass Profiling: An Emerging Approach in Quantitative Biophysics. *Nat. Methods* **2014**, *11* (12), 1221−8.

(3) Barer, R.; Tkaczyk, S. Refractive Index of Concentrated Protein Solutions. *Nature* **1954**, *173* (4409), 821−822.

(4) Barer, R. Determination of Dry Mass, Thickness, Solid and Water Concentration in Living Cells. *Nature* **1953**, *172* (4389), 1097−1098.

(5) Zhao, H.; Brown, P. H.; Schuck, P. On the Distribution of Protein Refractive Index Increments. *Biophys. J.* **2011**, *100* (9), 2309−17.

(6) Zernike, F. Phase Contrast, a New Method for the Microscopic Observation of Transparent Objects. *Physica* **1942**, *9* (7), 686−698.

(7) Zernike, F. Phase Contrast, a New Method for the Microscopic Observation of Transparent Objects Part Ii. *Physica* **1942**, *9* (10), 974−986.

(8) Allen, R. D.; David, G. B.; Nomarski, G. The Zeiss-Nomarski Differential Interference Equipment for Transmitted-Light Microscopy. *Z. Wiss. Mikroskopie u. Mikrotechnologie* **1969**, *69* (4), 193−221.

(9) King, S. V.; Libertun, A.; Piestun, R.; Cogswell, C. J.; Preza, C. Quantitative Phase Microscopy through Differential Interference Imaging. *J. Biomed. Opt.* **2008**, *13* (2), 024020.

(10) Fu, D.; Oh, S.; Choi, W.; Yamauchi, T.; Dorn, A.; Yaqoob, Z.; Dasari, R. R.; Feld, M. S. Quantitative DIC Microscopy Using an Off-

Axis Self-Interference Approach. *Opt. Lett.* **2010**, *35* (14), 2370−2372.
(11) Zangle, T. A.; Teitell, M. A.; Reed, J. Live Cell Interferometry Quantifies Dynamics of Biomass Partitioning During Cytokinesis. *PLoS One* **2014**, *9* (12), e115726.
(12) Reed, J.; Chun, J.; Zangle, T. A.; Kalim, S.; Hong, J. S.; Pefley, S. E.; Zheng, X.; Gimzewski, J. K.; Teitell, M. A. Rapid, Massively Parallel Single-Cell Drug Response Measurements Via Live Cell Interferometry. *Biophys. J.* **2011**, *101* (5), 1025−31.
(13) Platt, B. C.; Shack, R. History and Principles of Shack-Hartmann Wavefront Sensing. *J. Refract. Surg.* **2001**, *17* (5), S573−S577.
(14) Bon, P.; Maucort, G.; Wattellier, B.; Monneret, S. Quadriwave Lateral Shearing Interferometry for Quantitative Phase Microscopy of Living Cells. *Opt. Express* **2009**, *17* (15), 13080−94.
(15) Tian, L.; Waller, L. Quantitative Differential Phase Contrast Imaging in an LED Array Microscope. *Opt. Express* **2015**, *23* (9), 11394−403.
(16) Streibl, N. Phase Imaging by the Transport Equation of Intensity. *Opt. Commun.* **1984**, *49* (1), 6−10.
(17) Muller, P.; Cojoc, G.; Guck, J. Drymass: Handling and Analyzing Quantitative Phase Microscopy Images of Spherical, Cell-Sized Objects. *BMC Bioinf* **2020**, *21* (1), 226.
(18) Weart, S. R. *Selected Papers of Great American Physicists: The Bicentennial Commemorative Vol. of the American Physical Society 1976*. American Institute of Physics: New York, 1976; p 176.
(19) Lahiri, A. Quantum Optics. In *In Basic Optics*; Lahiri, A., Ed. Elsevier: Amsterdam, Netherlands, 2016; pp 697−899.
(20) Françon, M. Polarization Interference Microscopes. *Appl. Opt.* **1964**, *3* (9), 1033−1036.
(21) Sagnac, G. Luminous Ether Demonstrated by the Effect of Relative Wind of Ether in a Uniform Rotation of an Interferometer. *C. R. Hebd. Seances Acad. Sci.* **1913**, *157*, 708−710.
(22) Dyson, J. Common-Path Interferometer for Testing Purposes. *J. Opt. Soc. Am.* **1957**, *47* (5), 386−390.
(23) Dyson, J. An Interferometer Microscope. *Proc. R. Soc. London, Ser. A* **1950**, *204* (1077), 170−187.
(24) Mann, P.; Singh, V.; Tayal, S.; Thapa, P.; Mehta, D. S. White Light Phase Shifting Interferometric Microscopy with Whole Slide Imaging for Quantitative Analysis of Biological Samples. *J. Biophotonics* **2022**, *15*, e202100386.
(25) Kumar, R.; Srivastava, V.; Mehta, D. S.; Shakher, C. Role of Arbitrary Intensity Profile Laser Beam in Trapping of Rbc for Phase-Imaging. *J. Opt. Soc. Korea* **2016**, *20* (1), 78−87.
(26) de Groot, P. Phase Shifting Interferometry. In *Optical Measurement of Surface Topography*, 8 ed.; Leach, R., Ed.; Springer: Teddington, UK, 2011; pp 167−186.
(27) Marquet, P.; Rappaz, B.; Magistretti, P. J.; Cuche, E.; Emery, Y.; Colomb, T.; Depeursinge, C. Digital Holographic Microscopy: A Noninvasive Contrast Imaging Technique Allowing Quantitative Visualization of Living Cells with Subwavelength Axial Accuracy. *Opt. Lett.* **2005**, *30* (5), 468−470.
(28) Girshovitz, P.; Shaked, N. T. Fast Phase Processing in Off-Axis Holography Using Multiplexing with Complex Encoding and Live-Cell Fluctuation Map Calculation in Real-Time. *Opt. Express* **2015**, *23* (7), 8773−87.
(29) Barer, R. Interference Microscopy and Mass Determination. *Nature* **1952**, *169* (4296), 366−367.
(30) Davies, H. G.; Wilkins, M. H. F. Interference Microscopy and Mass Determination. *Nature* **1952**, *169* (4300), 541−541.
(31) Mitchison, J. The Growth of Single Cells: Ii. Saccharomyces Cerevisiae. *Exp. Cell Res.* **1958**, *15* (1), 214−221.
(32) Mitchison, J. The Growth of Single Cells: Iii. Streptococcus Faecalis. *Exp. Cell Res.* **1961**, *22*, 208−225.
(33) Davies, H. G.; Deeley, E. M. An Integrator for Measuring the "Dry Mass" of Cells and Isolated Components. *Exp. Cell Res.* **1956**, *11* (1), 169−185.
(34) Caspersson, T.; Carlson, L.; Svensson, G. A Scanning Interference Microscope Arrangement. *Exp. Cell Res.* **1954**, *7* (2), 601−602.
(35) Reed, J.; Troke, J. J.; Schmit, J.; Han, S.; Teitell, M. A.; Gimzewski, J. K. Live Cell Interferometry Reveals Cellular Dynamism During Force Propagation. *ACS Nano* **2008**, *2* (5), 841−846.
(36) Ross, K. F. A., Qualitatitve Interference Microscopy in the Cytology and the Measurement of Phase Change. In *Phase Contrast and Interference Microscopy for Cell Biologists*, 1 ed.; Edward Arnold: London, 1967; pp 87−116.
(37) Smith, F. H. Two Half-Shade Devices for Optical Polarizing Instruments. *Nature* **1954**, *173* (4399), 362−363.
(38) Mitchison, J. M.; Passano, L. M.; Smith, F. H. An Integration Method for the Interference Microscope. *Q. J. Microsc. Sci.* **1956**, *s3−97* (38), 287.
(39) Mitchison, J. M. Growth During the Cell Cycle. *Int. Rev. Cytol.* **2003**, *226*, 165−258.
(40) de Groot, P. J. Vibration in Phase-Shifting Interferometry. *J. Opt. Soc. Am. A* **1995**, *12* (2), 354−365.
(41) Ri, S.; Takimoto, T.; Xia, P.; Wang, Q.; Tsuda, H.; Ogihara, S. Accurate Phase Analysis of Interferometric Fringes by the Spatiotemporal Phase-Shifting Method. *J. Opt.* **2020**, *22* (10), 105703.
(42) Cherry, R. J., Video and Opto-Digital Imaging Microscopy. In *New Techniques of Optical Microscopy and Microspectroscopy*; Cherry, R. J., Ed.; Macmillan International Higher Education: London, 1991; pp 2−3.
(43) Mitchison, J. M. The Growth of Single Cells: I. Schizosaccharomyces Pombe. *Exp. Cell Res.* **1957**, *13* (2), 244−262.
(44) Cohen, D. K.; Cochran, E. R.; Ayres, J. D. Development of an Automatic Focusing Mechanism for an Interference Microscope, In Surface Characterization and Testing II. *Proc. SPIE* **1989**, *1164*, 962815.
(45) Creath, K. Step Height Measurement Using Two-Wavelength Phase-Shifting Interferometry. *Appl. Opt.* **1987**, *26* (14), 2810−2816.
(46) Wyant, J. C.; Creath, K. Advances in Interferometric Optical Profiling. *Int. J. Mach. Tools Manuf.* **1992**, *32* (1), 5−10.
(47) Zangle, T. A.; Burnes, D.; Mathis, C.; Witte, O. N.; Teitell, M. A. Quantifying Biomass Changes of Single Cd8+T Cells During Antigen Specific Cytotoxicity. *PLoS One* **2013**, *8* (7), e68916.
(48) Kim, D. N.; Teitell, M. A.; Reed, J.; Zangle, T. A. Hybrid Random Walk-Linear Discriminant Analysis Method for Unwrapping Quantitative Phase Microscopy Images of Biological Samples. *J. Biomed. Opt.* **2015**, *20* (11), 111211.
(49) Cuche, E.; Marquet, P.; Depeursinge, C. Simultaneous Amplitude-Contrast and Quantitative Phase-Contrast Microscopy by Numerical Reconstruction of Fresnel Off-Axis Holograms. *Appl. Opt.* **1999**, *38* (34), 6994−7001.
(50) Gabor, D. A New Microscopic Principle. *Nature* **1948**, *161* (4098), 777−778.
(51) Ash, E. A. Dennis Gabor, 1900−1979. *Nature* **1979**, *280* (5721), 431−433.
(52) Leith, E. N.; Upatnieks, J. Reconstructed Wavefronts and Communication Theory. *J. Opt. Soc. Am.* **1962**, *52* (10), 1123−1130.
(53) Leith, E. N.; Upatnieks, J. Wavefront Reconstruction with Diffused Illumination and 3-Dimensional Objects. *J. Opt. Soc. Am.* **1964**, *54* (11), 1295−1301.
(54) Hariharan, P., Holographic Imaging. In *Basics of Holography*; Cambridge University Press: Cambridge, UK, 2002; pp 1−8.
(55) Leith, E. N.; Upatnieks, J. Wavefront Reconstruction with Continuous-Tone Objects. *J. Opt. Soc. Am.* **1963**, *53* (12), 1377−1381.
(56) Knox, C. Holographic Microscopy as a Technique for Recording Dynamic Microscopic Subjects. *Science* **1966**, *153* (3739), 989−90.
(57) Goodman, J. W.; Lawrence, R. W. Digital Image Formation from Electronically Detected Holograms. *Appl. Phys. Lett.* **1967**, *11* (3), 77−79.

https://doi.org/10.1021/acsnano.1c11507
ACS Nano XXXX, XXX, XXX−XXX

(58) Goodman, J. W.; Huntley, W. H.; Jackson, D. W.; Lehmann, M. Wavefront-Reconstruction Imaging through Random Media. *Appl. Phys. Lett.* **1966**, *8* (12), 311−313.
(59) Schnars, U.; Jüptner, W. Direct Recording of Holograms by a Ccd Target and Numerical Reconstruction. *Appl. Opt.* **1994**, *33* (2), 179−181.
(60) Kim, M.-K. Applications of Digital Holography in Biomedical Microscopy. *J. Opt. Soc. Korea* **2010**, *14* (2), 77−89.
(61) Evans, E. A. Quantitative Reconstruction and Superresolution of Red-Blood-Cell Image Holograms. *J. Opt. Soc. Am.* **1971**, *61* (8), 991−7.
(62) Zhang, T.; Yamaguchi, I. Three-Dimensional Microscopy with Phase-Shifting Digital Holography. *Opt. Lett.* **1998**, *23* (15), 1221−1223.
(63) Cuche, E.; Bevilacqua, F.; Depeursinge, C. Digital Holography for Quantitative Phase-Contrast Imaging. *Opt. Lett.* **1999**, *24* (5), 291−293.
(64) Milgram, J. H.; Li, W. Computational Reconstruction of Images from Holograms. *Appl. Opt.* **2002**, *41* (5), 853−864.
(65) Lichte, H.; Lehmann, M. Electron Holography—Basics and Applications. *Rep. Prog. Phys.* **2008**, *71* (1), 016102.
(66) Rappaz, B.; Marquet, P.; Cuche, E.; Emery, Y.; Depeursinge, C.; Magistretti, P. J. Measurement of the Integral Refractive Index and Dynamic Cell Morphometry of Living Cells with Digital Holographic Microscopy. *Opt. Express* **2005**, *13* (23), 9361−9373.
(67) Turko, N. A.; Shaked, N. T. Erythrocyte Volumetric Measurements in Imaging Flow Cytometry Using Simultaneous Three-Wavelength Digital Holographic Microscopy. *Biomed. Opt. Express* **2020**, *11* (11), 6649−6658.
(68) Story, J. B.; Ballard, G. S.; Gibbons, R. H. Schlieren Photographs from Holograms. *J. Appl. Phys.* **1966**, *37* (5), 2183−2184.
(69) Tsuruta, T.; Itoh, Y. Hologram Schlieren and Phase-Contrast Methods. *Jpn. J. Appl. Phys.* **1969**, *8* (1), 96.
(70) Kemper, B.; Langehanenberg, P.; Kosmeier, S.; Schlichthaber, F.; Remmersmann, C.; von Bally, G.; Rommel, C.; Dierker, C.; Schnekenburger, J., Digital Holographic Microscopy: Quantitative Phase Imaging and Applications in Live Cell Analysis. In *Handbook of Coherent-Domain Optical Methods: Biomedical Diagnostics, Environmental Monitoring, and Materials Science*; Tuchin, V. V., Ed. Springer: New York, 2013; pp 215−257.
(71) Wang, Z.; Millet, L.; Mir, M.; Ding, H.; Unarunotai, S.; Rogers, J.; Gillette, M. U.; Popescu, G. Spatial Light Interference Microscopy (SLIM). *Opt. Express* **2011**, *19* (2), 1016−1026.
(72) Meier, R. W. Twin-Image Elimination in Holography Using Single-Sideband Waves. *J. Opt. Soc. Am.* **1969**, *59* (3), 358−359.
(73) Sánchez-Ortiga, E.; Doblas, A.; Saavedra, G.; Martínez-Corral, M.; Garcia-Sucerquia, J. Off-Axis Digital Holographic Microscopy: Practical Design Parameters for Operating at Diffraction Limit. *Appl. Opt.* **2014**, *53* (10), 2058−2066.
(74) Awatsuji, Y.; Xia, P.; Matoba, O. In *Parallel Phase-Shifting Digital Holography and Its Applications to High-Speed 3d Imaging and Microscopy*, Digital Holography and Three-Dimensional Imaging; Optica Publishing Group: JeJu Island, 2017; p M3A.2.
(75) Belanger, E.; Berube, J. P.; de Dorlodot, B.; Marquet, P.; Vallee, R. Comparative Study of Quantitative Phase Imaging Techniques for Refractometry of Optical Waveguides. *Opt. Express* **2018**, *26* (13), 17498−17510.
(76) Jim, S. History of the Shack Hartmann wavefront sensor and its impact in ophthalmic optics, Proc.SPIE, In Fifty Years of Optical Sciences at The University of Arizona; SPIE Optical Engineering + Applications. *Proc. SPIE* **2014**, *9186*, 2064536.
(77) Ronchi, V. 40 Years of History of Grating Interferometer. *Appl. Opt.* **1964**, *3* (4), 437.
(78) Akondi, V.; Dubra, A. Accounting for Focal Shift in the Shack-Hartmann Wavefront Sensor. *Opt. Lett.* **2019**, *44* (17), 4151−4154.
(79) Bates, W. J. A Wavefront Shearing Interferometer. *Proc. Phys. Soc.* **1947**, *59* (6), 940−950−2.
(80) Primot, J.; Sogno, L. Achromatic 3-Wave (or More) Lateral Shearing Interferometer. *J. Opt. Soc. Am. A* **1995**, *12* (12), 2679−2685.
(81) Freischlad, K. R.; Koliopoulos, C. L. Modal Estimation of a Wave Front from Difference Measurements Using the Discrete Fourier Transform. *J. Opt. Soc. Am. A* **1986**, *3* (11), 1852−1861.
(82) Primot, J. Three-Wave Lateral Shearing Interferometer. *Appl. Opt.* **1993**, *32* (31), 6242−6249.
(83) Primot, J.; Guerineau, N. Extended Hartmann Test Based on the Pseudoguiding Property of a Hartmann Mask Completed by a Phase Chessboard. *Appl. Opt.* **2000**, *39* (31), 5715−5720.
(84) Curl, C. L.; Bellair, C. J.; Harris, P. J.; Allman, B. E.; Roberts, A.; Nugent, K. A.; Delbridge, L. M. Single Cell Volume Measurement by Quantitative Phase Microscopy (QPM): A Case Study of Erythrocyte Morphology. *Cell. Physiol. Biochem.* **2006**, *17* (5−6), 193−200.
(85) Huang, D.; Leslie, K. A.; Guest, D.; Yeshcheulova, O.; Roy, I. J.; Piva, M.; Moriceau, G.; Zangle, T. A.; Lo, R. S.; Teitell, M. A.; Reed, J. High-Speed Live-Cell Interferometry: A New Method for Quantifying Tumor Drug Resistance and Heterogeneity. *Anal. Chem.* **2018**, *90* (5), 3299−3306.
(86) Bryngdahl, O.; Lohmann, A. Single-Sideband Holography*. *J. Opt. Soc. Am.* **1968**, *58* (5), 620−624.
(87) Pradeep, S.; Zangle, T. A. Quantitative Phase Velocimetry Measures Bulk Intracellular Transport of Cell Mass During the Cell Cycle. *Sci. Rep.* **2022**, *12* (1), 6074.
(88) Liu, X.; Oh, S.; Peshkin, L.; Kirschner, M. W. Computationally Enhanced Quantitative Phase Microscopy Reveals Autonomous Oscillations in Mammalian Cell Growth. *Proc. Natl. Acad. Sci. U. S. A.* **2020**, *117* (44), 27388−27399.
(89) Ma, S. J.; Liu, Q.; Yu, Y. T.; Luo, Y.; Wang, S. L. Quantitative Phase Imaging in Digital Holographic Microscopy Based on Image Inpainting Using a Two-Stage Generative Adversarial Network. *Opt. Express* **2021**, *29* (16), 24928−24946.
(90) Aknoun, S.; Yonnet, M.; Djabari, Z.; Graslin, F.; Taylor, M.; Pourcher, T.; Wattellier, B.; Pognonec, P. Quantitative Phase Microscopy for Non-Invasive Live Cell Population Monitoring. *Sci. Rep.* **2021**, *11* (1), 4409.
(91) Zuo, C.; Li, J.; Sun, J.; Fan, Y.; Zhang, J.; Lu, L.; Zhang, R.; Wang, B.; Huang, L.; Chen, Q. Transport of Intensity Equation: A Tutorial. *Opt. Lasers Eng.* **2020**, *135*, 106187.
(92) Latychevskaia, T. Iterative Phase Retrieval for Digital Holography: Tutorial. *J. Opt. Soc. Am. A* **2019**, *36* (12), D31−D40.
(93) Gerchberg, R. W. A Practical Algorithm for the Determination of Phase from Image and Diffraction Plane Pictures. *Optik* **1972**, *35*, 237−246.
(94) Fienup, J. R. Reconstruction of an Object from the Modulus of Its Fourier Transform. *Opt. Lett.* **1978**, *3* (1), 27−29.
(95) Fienup, J. R. Iterative Method Applied to Image Reconstruction and to Computer-Generated Holograms. *Opt. Eng.* **1980**, *19* (3), 297−305.
(96) Marrison, J.; Raty, L.; Marriott, P.; O'Toole, P. Ptychography - a Label Free, High-Contrast Imaging Technique for Live Cells Using Quantitative Phase Information. *Sci. Rep.* **2013**, *3*, 2369.
(97) Godden, T. M.; Muniz-Piniella, A.; Claverley, J. D.; Yacoot, A.; Humphry, M. J. Phase Calibration Target for Quantitative Phase Imaging with Ptychography. *Opt. Express* **2016**, *24* (7), 7679−7692.
(98) Tian, L.; Waller, L. 3d Intensity and Phase Imaging from Light Field Measurements in an LED Array Microscope. *Optica* **2015**, *2* (2), 104−111.
(99) Hegerl, R.; Hoppe, W. Dynamische Theorie Der Kristallstrukturanalyse Durch Elektronenbeugung Im Inhomogenen Primärstrahlwellenfeld. *Berichte der Bunsengesellschaft für physikalische Chemie* **1970**, *74* (11), 1148−1154.
(100) Konda, P. C.; Loetgering, L.; Zhou, K. C.; Xu, S. Q.; Harvey, A. R.; Horstmeyer, R. Fourier Ptychography: Current Applications and Future Promises. *Opt. Express* **2020**, *28* (7), 9603−9630.

https://doi.org/10.1021/acsnano.1c11507
ACS Nano XXXX, XXX, XXX−XXX

(101) Zheng, G.; Shen, C.; Jiang, S.; Song, P.; Yang, C. Concept, Implementations and Applications of Fourier Ptychography. *Nat. Rev. Phys.* **2021**, *3* (3), 207−223.
(102) Horstmeyer, R.; Chung, J.; Ou, X.; Zheng, G.; Yang, C. Diffraction Tomography with Fourier Ptychography. *Optica* **2016**, *3* (8), 827−835.
(103) Bostan, E.; Froustey, E.; Rappaz, B.; Shaffer, E.; Sage, D.; Unser, M. Phase Retrieval by Using Transport-of-Intensity Equation and Differential Interference Contrast Microscopy. Proceedings from the *2014 IEEE International Conference on Image Processing (ICIP)*, October 27−30, 2014, Paris, France; IEEE: New York, 2014; pp 3939−3943.
(104) Lu, L. P.; Fan, Y.; Sun, J. S.; Zhang, J. L.; Wu, X. J.; Chen, Q.; Zuo, C. Accurate Quantitative Phase Imaging by the Transport of Intensity Equation: A Mixed-Transfer-Function Approach. *Opt. Lett.* **2021**, *46* (7), 1740−1743.
(105) Kachar, B. Asymmetric Illumination Contrast: A Method of Image Formation for Video Light Microscopy. *Science* **1985**, *227* (4688), 766−768.
(106) Mehta, S. B.; Sheppard, C. J. R. Quantitative Phase-Gradient Imaging at High Resolution with Asymmetric Illumination-Based Differential Phase Contrast. *Opt. Lett.* **2009**, *34* (13), 1924−1926.
(107) Guenther, B. D., Phase Contrast Microscopy. In *Encyclopedia of Modern Optics*; Elsevier: Amsterdam, Netherlands, 2005; pp 103−111.
(108) Dekkers, N.; De Lang, H. Differential Phase Contrast in a Stem. *Optik* **1974**, *41* (4), 452−456.
(109) Stewart, W. C. On Differential Phase Contrast with an Extended Illumination Source. *J. Opt. Soc. Am.* **1976**, *66* (8), 813−818.
(110) Hamilton, D.; Sheppard, C. Differential Phase Contrast in Scanning Optical Microscopy. *J. Microsc.* **1984**, *133* (1), 27−39.
(111) Kwon, H.; Arbabi, E.; Kamali, S. M.; Faraji-Dana, M.; Faraon, A. Single-Shot Quantitative Phase Gradient Microscopy Using a System of Multifunctional Metasurfaces. *Nat. Photonics* **2020**, *14* (2), 109−114.
(112) Hai, N.; Rosen, J. Phase Contrast-Based Phase Retrieval: A Bridge between Qualitative Phase Contrast and Quantitative Phase Imaging by Phase Retrieval Algorithms. *Opt. Lett.* **2020**, *45* (20), 5812−5815.
(113) Zhang, Y. a. n.; Pedrini, G.; Osten, W.; Tiziani, H. J. Phase Retrieval Microscopy for Quantitative Phase-Contrast Imaging. *Optik* **2004**, *115* (2), 94−96.
(114) Sheppard, C. J. R. Defocused Transfer Function for a Partially Coherent Microscope and Application to Phase Retrieval. *J. Opt. Soc. Am. A* **2004**, *21* (5), 828−831.
(115) Anand, V.; Katkus, T.; Linklater, D. P.; Ivanova, E. P.; Juodkazis, S. Lensless Three-Dimensional Quantitative Phase Imaging Using Phase Retrieval Algorithm. *J. Imaging* **2020**, *6* (9), 99.
(116) Kou, S. S.; Waller, L.; Barbastathis, G.; Marquet, P.; Depeursinge, C.; Sheppard, C. J. R. Quantitative Phase Restoration by Direct Inversion Using the Optical Transfer Function. *Opt. Lett.* **2011**, *36* (14), 2671−2673.
(117) Martinez-Carranza, J.; Falaggis, K.; Kozacki, T. Fast and Accurate Phase-Unwrapping Algorithm Based on the Transport of Intensity Equation. *Appl. Opt.* **2017**, *56* (25), 7079−7088.
(118) Gureyev, T. E.; Nugent, K. A. Rapid Quantitative Phase Imaging Using the Transport of Intensity Equation. *Opt. Commun.* **1997**, *133* (1), 339−346.
(119) Carol, J. C.; Nicholas, I. S.; Kieran, G. L.; Parameswaran, H. Quantitative DIC microscopy using a geometric phase shifter, In Three-Dimensional Microscopy: Image Acquisition and Processing IV; BiOS '97, Part of Photonics West. *Proc. SPIE* **1997**, *2984*, 271252.
(120) Fan, Y.; Sun, J.; Chen, Q.; Pan, X.; Trusiak, M.; Zuo, C. Single-Shot Isotropic Quantitative Phase Microscopy Based on Color-Multiplexed Differential Phase Contrast. *APL Photonics* **2019**, *4* (12), 121301.
(121) Kocsis, P.; Shevkunov, I.; Katkovnik, V.; Egiazarian, K. Single Exposure Lensless Subpixel Phase Imaging: Optical System Design, Modelling, and Experimental Study. *Opt. Express* **2020**, *28* (4), 4625−4637.
(122) Chia, Y. H.; Vyas, S.; Tsai, J. C.; Huang, Y. Y.; Yeh, J. A.; Luo, Y. Multiplane Differential Phase Contrast Imaging Using Asymmetric Illumination in Volume Holographic Microscopy. *J. Biomed. Opt.* **2020**, *25* (12), 123704.
(123) Wang, K.; Di, J.; Li, Y.; Ren, Z.; Kemao, Q.; Zhao, J. Transport of Intensity Equation from a Single Intensity Image Via Deep Learning. *Opt. Lasers Eng.* **2020**, *134*, 106233.
(124) Rivenson, Y.; Zhang, Y.; Gunaydin, H.; Teng, D.; Ozcan, A. Phase Recovery and Holographic Image Reconstruction Using Deep Learning in Neural Networks. *Light: Sci. Appl.* **2018**, *7*, 17141.
(125) Janik, M.; Koba, M.; Celebanska, A.; Bock, W. J.; Smietana, M. Live E. Coli Bacteria Label-Free Sensing Using a Microcavity in-Line Mach-Zehnder Interferometer. *Sci. Rep.* **2018**, *8* (1), 17176.
(126) Goodwin, M. J.; Besselink, G. A. J.; Falke, F.; Everhardt, A. S.; Cornelissen, J.; Huskens, J. Highly Sensitive Protein Detection by Asymmetric Mach-Zehnder Interferometry for Biosensing Applications. *ACS Appl. Bio Mater.* **2020**, *3* (7), 4566−4572.
(127) Bhaduri, B.; Edwards, C.; Pham, H.; Zhou, R.; Nguyen, T. H.; Goddard, L. L.; Popescu, G. Diffraction Phase Microscopy: Principles and Applications in Materials and Life Sciences. *Adv. Opt. Photonics* **2014**, *6* (1), 57−119.
(128) Ling, T.; Boyle, K. C.; Zuckerman, V.; Flores, T.; Ramakrishnan, C.; Deisseroth, K.; Palanker, D. High-Speed Interferometric Imaging Reveals Dynamics of Neuronal Deformation During the Action Potential. *Proc. Natl. Acad. Sci. U. S. A.* **2020**, *117* (19), 10278−10285.
(129) Phillips, Z. F.; Chen, M.; Waller, L. Single-Shot Quantitative Phase Microscopy with Color-Multiplexed Differential Phase Contrast (Cdpc). *PLoS One* **2017**, *12* (2), No. e0171228.
(130) Fan, X.; Tang, Z.; O'Dwyer, K.; Hennelly, B. M. An Inexpensive Portable Self-Reference Module for Digital Holographic Microscopy. *Photonics* **2021**, *8* (7), 277.
(131) Baek, Y.; Park, Y. Intensity-Based Holographic Imaging Via Space-Domain Kramers−Kronig Relations. *Nat. Photonics* **2021**, *15* (5), 354−360.
(132) Rodrigo, J. A.; Alieva, T. Rapid Quantitative Phase Imaging for Partially Coherent Light Microscopy. *Opt. Express* **2014**, *22* (11), 13472−83.
(133) Liang, C.; Wu, G.; Wang, F.; Li, W.; Cai, Y.; Ponomarenko, S. A. Overcoming the Classical Rayleigh Diffraction Limit by Controlling Two-Point Correlations of Partially Coherent Light Sources. *Opt. Express* **2017**, *25* (23), 28352.
(134) Wu, X. J.; Sun, J. S.; Zhang, J. L.; Lu, L. P.; Chen, R.; Chen, Q.; Zuo, C. Wavelength-Scanning Lensfree on-Chip Microscopy for Wide-Field Pixel-Super-Resolved Quantitative Phase Imaging. *Opt. Lett.* **2021**, *46* (9), 2023−2026.
(135) Waller, L.; Luo, Y.; Yang, S. Y.; Barbastathis, G. Transport of Intensity Phase Imaging in a Volume Holographic Microscope. *Opt. Lett.* **2010**, *35* (17), 2961−2963.
(136) Yoneda, N.; Onishi, A.; Saita, Y.; Komuro, K.; Nomura, T. Single-Shot Higher-Order Transport-of-Intensity Quantitative Phase Imaging Based on Computer-Generated Holography. *Opt. Express* **2021**, *29* (4), 4783−4801.
(137) Zuo, C.; Chen, Q.; Qu, W.; Asundi, A. High-Speed Transport-of-Intensity Phase Microscopy with an Electrically Tunable Lens. *Opt. Express* **2013**, *21* (20), 24060−75.
(138) Ahmad, A.; Dubey, V.; Butola, A.; Ahluwalia, B. S.; Mehta, D. S. Highly Temporal Stable, Wavelength-Independent, and Scalable Field-of-View Common-Path Quantitative Phase Microscope. *J. Biomed. Opt.* **2020**, *25* (11), 116501 DOI: 10.1117/1.JBO.25.11.116501.
(139) Godden, T. M.; Suman, R.; Humphry, M. J.; Rodenburg, J. M.; Maiden, A. M. Ptychographic Microscope for Three-Dimensional Imaging. *Opt. Express* **2014**, *22* (10), 12513−23.
(140) Singh, D. K.; Ahrens, C. C.; Li, W.; Vanapalli, S. A. Label-Free Fingerprinting of Tumor Cells in Bulk Flow Using Inline Digital Holographic Microscopy. *Biomed. Opt. Express* **2017**, *8* (2), 536−554.

https://doi.org/10.1021/acsnano.1c11507
ACS Nano XXXX, XXX, XXX−XXX

(141) Cao, R.; Kellman, M.; Ren, D.; Eckert, R.; Waller, L. Self-Calibrated 3d Differential Phase Contrast Microscopy with Optimized Illumination. *Biomed. Opt. Express* **2022**, *13* (3), 1671.
(142) Wang, Z.; Marks, D. L.; Carney, P. S.; Millet, L. J.; Gillette, M. U.; Mihi, A.; Braun, P. V.; Shen, Z.; Prasanth, S. G.; Popescu, G. Spatial Light Interference Tomography (SLIT). *Opt. Express* **2011**, *19* (21), 19907−19918.
(143) Kwee, E.; Peterson, A.; Halter, M.; Elliott, J. Practical Application of Microsphere Samples for Benchmarking a Quantitative Phase Imaging System. *Cytometry Part A* **2021**, *99* (10), 1022−1032.
(144) Dubey, V.; Singh, G.; Singh, V.; Ahmad, A.; Mehta, D. S. Multispectral Quantitative Phase Imaging of Human Red Blood Cells Using Inexpensive Narrowband Multicolor LEDs. *Appl. Opt.* **2016**, *55* (10), 2521−5.
(145) Rappaz, B.; Barbul, A.; Emery, Y.; Korenstein, R.; Depeursinge, C.; Magistretti, P. J.; Marquet, P. Comparative Study of Human Erythrocytes by Digital Holographic Microscopy, Confocal Microscopy, and Impedance Volume Analyzer. *Cytometry Part A* **2008**, *73A* (10), 895−903.
(146) Allier, C.; Herve, L.; Mandula, O.; Blandin, P.; Usson, Y.; Savatier, J.; Monneret, S.; Morales, S. Quantitative Phase Imaging of Adherent Mammalian Cells: A Comparative Study. *Biomed. Opt. Express* **2019**, *10* (6), 2768−2783.
(147) Ziemczonok, M.; Kus, A.; Wasylczyk, P.; Kujawinska, M. 3d-Printed Biological Cell Phantom for Testing 3d Quantitative Phase Imaging Systems. *Sci. Rep.* **2019**, *9*, 18872.
(148) Popescu, G., Image Characteristics. In *Quantitative Phase Imaging of Cells and Tissues*; McGraw-Hill: New York, 2011; pp 57−59.
(149) Chauhan, K.; Chauhan, R. K.; Saini, A., Enhancement and Despeckling of Echocardiographic Images. In *Soft Computing Based Medical Image Analysis*, Dey, N., Ashour, A. S., Shi, F., Balas, V. E., Eds. Academic Press: London, 2018; pp 61−79.
(150) Chen, L.; Chen, Z.; Singh, R. K.; Vinu, R. V.; Pu, J. Increasing Field of View and Signal to Noise Ratio in the Quantitative Phase Imaging with Phase Shifting Holography Based on the Hanbury Brown-Twiss Approach. *Opt. Lasers Eng.* **2022**, *148*, 106771.
(151) Aknoun, S.; Savatier, J.; Bon, P.; Galland, F.; Abdeladim, L.; Wattellier, B.; Monneret, S. Living Cell Dry Mass Measurement Using Quantitative Phase Imaging with Quadriwave Lateral Shearing Interferometry: An Accuracy and Sensitivity Discussion. *J. Biomed. Opt.* **2015**, *20* (12), 126009.
(152) Chen, S.; Li, C.; Zhu, Y. Sensitivity Evaluation of Quantitative Phase Imaging: A Study of Wavelength Shifting Interferometry. *Opt. Lett.* **2017**, *42* (6), 1088−1091.
(153) Chen, S.; Li, C.; Zhu, Y. Low-Coherence Wavelength Shifting Interferometry for High-Speed Quantitative Phase Imaging. *Opt. Lett.* **2016**, *41* (15), 3431−4.
(154) Jiao, Y.; He, Y. R.; Kandel, M. E.; Liu, X.; Lu, W.; Popescu, G. Computational Interference Microscopy Enabled by Deep Learning. *APL Photonics* **2021**, *6* (4), 046103.
(155) Malinovski, I.; França, R. S.; Couceiro, I. B. Software for Imaging Phase-Shift Interference Microscope. *J. Phys.: Conf. Ser.* **2018**, *975*, 012034.
(156) Lariviere-Loiselle, C.; Belanger, E.; Marquet, P. Polychromatic Digital Holographic Microscopy: A Quasicoherent-Noise-Free Imaging Technique to Explore the Connectivity of Living Neuronal Networks. *Neurophotonics* **2020**, *7* (4), 040501.
(157) Balasubramani, V.; Kujawinska, M.; Allier, C.; Anand, V.; Cheng, C. J.; Depeursinge, C.; Hai, N.; Juodkazis, S.; Kalkman, J.; Kus, A.; Lee, M.; Magistretti, P. J.; Marquet, P.; Ng, S. H.; Rosen, J.; Park, Y. K.; Ziemczonok, M. Roadmap on Digital Holography-Based Quantitative Phase Imaging. *J. Imaging* **2021**, *7* (12), 252.
(158) Charrière, F.; Colomb, T.; Montfort, F.; Cuche, E.; Marquet, P.; Depeursinge, C. Shot-Noise Influence on the Reconstructed Phase Image Signal-to-Noise Ratio in Digital Holographic Microscopy. *Appl. Opt.* **2006**, *45* (29), 7667−7673.
(159) Alfoldi, R.; Balog, J. A.; Farago, N.; Halmai, M.; Kotogany, E.; Neuperger, P.; Nagy, L. I.; Feher, L. Z.; Szebeni, G. J.; Puskas, L. G. Single Cell Mass Cytometry of Non-Small Cell Lung Cancer Cells Reveals Complexity of in Vivo and Three-Dimensional Models over the Petri-Dish. *Cells* **2019**, *8* (9), 1093.
(160) Kuhn, J.; Shaffer, E.; Mena, J.; Breton, B.; Parent, J.; Rappaz, B.; Chambon, M.; Emery, Y.; Magistretti, P.; Depeursinge, C.; Marquet, P.; Turcatti, G. Label-Free Cytotoxicity Screening Assay by Digital Holographic Microscopy. *Assay Drug Dev. Technol.* **2013**, *11* (2), 101−107.
(161) Velghe, S.; Guérineau, N.; Haïdar, R.; Toulon, B.; Demoustier, S.; Primot, J. Two-Color Multi-Wave Lateral Shearing Interferometry for Segmented Wave-Front Measurements. *Opt. Express* **2006**, *14* (21), 9699−9708.
(162) Baffou, G. Quantitative Phase Microscopy Using Quadriwave Lateral Shearing Interferometry (QLSI): Principle, Terminology, Algorithm and Grating Shadow Description. *J. Phys. D: Appl. Phys.* **2021**, *54* (29), 294002.
(163) Zuo, C.; Sun, J. S.; Li, J. J.; Zhang, J. L.; Asundi, A.; Chen, Q. High-Resolution Transport-of-Intensity Quantitative Phase Microscopy with Annular Illumination. *Sci. Rep.* **2017**, *7* (1), 7654.
(164) Komuro, K.; Nomura, T. Quantitative Phase Imaging Using Transport of Intensity Equation with Multiple Bandpass Filters. *Appl. Opt.* **2016**, *55* (19), 5180−6.
(165) Komuro, K.; Yamazaki, Y.; Nomura, T. Transport-of-Intensity Computational Ghost Imaging. *Appl. Opt.* **2018**, *57* (16), 4451−4456.
(166) Gupta, A. K.; Nishchal, N. K.; Banerjee, P. P. Transport of Intensity Equation Based Photon-Counting Phase Imaging. *OSA Continuum* **2020**, *3* (2), 236.
(167) Zhang, F.; Pedrini, G.; Osten, W. Phase Retrieval of Arbitrary Complex-Valued Fields through Aperture-Plane Modulation. *Phys. Rev. A* **2007**, *75* (4), 043805.
(168) Grant, S. D.; Richford, K.; Burdett, H. L.; McKee, D.; Patton, B. R. Low-Cost, Open-Access Quantitative Phase Imaging of Algal Cells Using the Transport of Intensity Equation. *R. Soc. Open Sci.* **2020**, *7* (1), 191921.
(169) Tian, L.; Li, X.; Ramchandran, K.; Waller, L. Multiplexed Coded Illumination for Fourier Ptychography with an LED Array Microscope. *Biomed. Opt. Express* **2014**, *5* (7), 2376−2389.
(170) Fitzpatrick, C. R. M.; Wilson, A.; Sawyer, T. W.; Christopher, P. J.; Wilkinson, T. D.; Bohndiek, S. E.; Gordon, G. S. D. Robustness to Misalignment of Low-Cost, Compact Quantitative Phase Imaging Architectures. *OSA Continuum* **2020**, *3* (10), 2660−2679.
(171) Shillaber, C. P. Light, Lenses, Images, and Objectives. In *Photomicrography in Theory and Practice*, 2 ed.; John Wiley & Sons, Inc.: New York, 1944; Vol. *1*, pp 148−286.
(172) Erickson, E. F.; Brown, R. M. Calculation of Fringe Visibility in a Laser-Illuminated Interferometer. *J. Opt. Soc. Am.* **1967**, *57* (3), 367.
(173) Dong, J. T.; Lu, R. S.; Li, Y.; Wu, K. Automated Determination of Best Focus and Minimization of Optical Path Difference in Linnik White Light Interferometry. *Appl. Opt.* **2011**, *50* (30), 5861−5871.
(174) Groen, F. C. A.; Young, I. T.; Ligthart, G. A Comparison of Different Focus Functions for Use in Autofocus Algorithms. *Cytometry Part A* **1985**, *6* (2), 81−91.
(175) Xu, J.; Tian, X. L.; Meng, X.; Kong, Y.; Gao, S. M.; Cui, H. Y.; Liu, F.; Xue, L.; Liu, C.; Wang, S. Y. Wavefront-Sensing-Based Autofocusing in Microscopy. *J. Biomed. Opt.* **2017**, *22* (8), 1.
(176) Tamura, H.; Mori, S.; Yamawaki, T. Textural Features Corresponding to Visual-Perception. *IEEE Trans. Syst. Man Cybern.* **1978**, *8* (6), 460−473.
(177) Langehanenberg, P.; Kemper, B.; Dirksen, D.; von Bally, G. Autofocusing in Digital Holographic Phase Contrast Microscopy on Pure Phase Objects for Live Cell Imaging. *Appl. Opt.* **2008**, *47* (19), D176−D182.
(178) Tang, M.; Tang, Z. Y.; Qiao, X.; Lang, K. Q.; Sun, Y.; Wang, X. P. Extension of Refocus Depth Range in Digital Holographic Microscopy. *Appl. Opt.* **2020**, *59* (28), 8540−8552.

https://doi.org/10.1021/acsnano.1c11507
ACS Nano XXXX, XXX, XXX−XXX

(179) Tyc, M.; Kvasnica, L.; Slaba, M.; Chmelik, R. Numerical Refocusing in Digital Holographic Microscopy with Extended-Sources Illumination. *Opt. Express* **2013**, *21* (23), 28258−28271.
(180) Dubois, F.; Joannes, L.; Legros, J. C. Improved Three-Dimensional Imaging with a Digital Holography Microscope with a Source of Partial Spatial Coherence. *Appl. Opt.* **1999**, *38* (34), 7085−7094.
(181) Trusiak, M.; Picazo-Bueno, J. A.; Zdankowski, P.; Mico, V. Darkfocus: Numerical Autofocusing in Digital in-Line Holographic Microscopy Using Variance of Computational Dark-Field Gradient. *Opt. Lasers Eng.* **2020**, *134*, 106195.
(182) Dubois, F.; Schockaert, C.; Callens, N.; Yourassowsky, C. Focus Plane Detection Criteria in Digital Holography Microscopy by Amplitude Analysis. *Opt. Express* **2006**, *14* (13), 5895−5908.
(183) Liebling, M.; Unser, M. Autofocus for Digital Fresnel Holograms by Use of a Fresnelet-Sparsity Criterion. *J. Opt. Soc. Am. A* **2004**, *21* (12), 2424−2430.
(184) Memmolo, P.; Paturzo, M.; Javidi, B.; Netti, P. A.; Ferraro, P. Refocusing Criterion Via Sparsity Measurements in Digital Holography. *Opt. Lett.* **2014**, *39* (16), 4719−4722.
(185) Yang, Y.; Kang, B. S.; Choo, Y. J. Application of the Correlation Coefficient Method for Determination of the Focal Plane to Digital Particle Holography. *Appl. Opt.* **2008**, *47* (6), 817−824.
(186) Liu, J.; Zhao, Y. X.; Guo, C.; Zhao, W. S.; Zhang, Y. T.; Guo, C. L.; Li, H. Y. Robust Autofocusing Method for Multi-Wavelength Lensless Imaging. *Opt. Express* **2019**, *27* (17), 23814−23829.
(187) Ferraro, P.; Alferi, D.; De Nicola, S.; De Petrocellis, L.; Finizio, A.; Pierattini, G. Quantitative Phase-Contrast Microscopy by a Lateral Shear Approach to Digital Holographic Image Reconstruction. *Opt. Lett.* **2006**, *31* (10), 1405−1407.
(188) Ferraro, P.; Del Core, C.; Miccio, L.; Grilli, S.; De Nicola, S.; Finizio, A.; Coppola, G. Phase Map Retrieval in Digital Holography: Avoiding the Undersampling Effect by a Lateral Shear Approach. *Opt. Lett.* **2007**, *32* (15), 2233−5.
(189) Tzur, A.; Kafri, R.; LeBleu, V. S.; Lahav, G.; Kirschner, M. W. Cell Growth and Size Homeostasis in Proliferating Animal Cells. *Science* **2009**, *325* (5937), 167−171.
(190) Cooper, K. L.; Oh, S.; Sung, Y.; Dasari, R. R.; Kirschner, M. W.; Tabin, C. J. Multiple Phases of Chondrocyte Enlargement Underlie Differences in Skeletal Proportions. *Nature* **2013**, *495* (7441), 375−378.
(191) Davies, H. G.; Wilkins, M. H. F.; Chayen, J.; Lacour, L. F. The Use of the Interference Microscope to Determine Dry Mass in Living Cells and as a Quantitative Cytochemical Method. *Q. J. Microsc. Sci.* **1954**, *95* (3), 271.
(192) Mir, M.; Wang, Z.; Shen, Z.; Bednarz, M.; Bashir, R.; Golding, I.; Prasanth, S. G.; Popescu, G. Optical Measurement of Cycle-Dependent Cell Growth. *Proc. Natl. Acad. Sci. U. S. A.* **2011**, *108* (32), 13124−9.
(193) Kemper, B.; Bauwens, A.; Vollmer, A.; Ketelhut, S.; Langehanenberg, P.; Muthing, J.; Karch, H.; von Bally, G. Label-Free Quantitative Cell Division Monitoring of Endothelial Cells by Digital Holographic Microscopy. *J. Biomed. Opt.* **2010**, *15* (3), 036009.
(194) Popescu, G.; Park, Y.; Lue, N.; Best-Popescu, C.; Deflores, L.; Dasari, R. R.; Feld, M. S.; Badizadegan, K. Optical Imaging of Cell Mass and Growth Dynamics. *Am. J. Physiol.: Cell Physiol.* **2008**, *295* (2), C538−C544.
(195) Tian, L.; Liu, Z. J.; Yeh, L. H.; Chen, M.; Zhong, J. S.; Waller, L. Computational Illumination for High-Speed in Vitro Fourier Ptychographic Microscopy. *Optica* **2015**, *2* (10), 904−911.
(196) Rappaz, B.; Cano, E.; Colomb, T.; Kuhn, J.; Depeursinge, C.; Simanis, V.; Magistretti, P. J.; Marquet, P. Noninvasive Characterization of the Fission Yeast Cell Cycle by Monitoring Dry Mass with Digital Holographic Microscopy. *J. Biomed. Opt.* **2009**, *14* (3), 034049.
(197) Pavillon, N.; Kuhn, J.; Moratal, C.; Jourdain, P.; Depeursinge, C.; Magistretti, P. J.; Marquet, P. Early Cell Death Detection with Digital Holographic Microscopy. *PLoS One* **2012**, *7* (1), No. e30912.
(198) Vicar, T.; Raudenska, M.; Gumulec, J.; Balvan, J. The Quantitative-Phase Dynamics of Apoptosis and Lytic Cell Death. *Sci. Rep.* **2020**, *10* (1), 1566.
(199) Kemper, B.; von Bally, G. Digital Holographic Microscopy for Live Cell Applications and Technical Inspection. *Appl. Opt.* **2008**, *47* (4), A52−A61.
(200) Kemper, B.; Carl, D.; Schnekenburger, J.; Bredebusch, I.; Schafer, M.; Domschke, W.; von Bally, G. Investigation of Living Pancreas Tumor Cells by Digital Holographic Microscopy. *J. Biomed. Opt.* **2006**, *11* (3), 034005.
(201) Zuo, C.; Chen, Q.; Qu, W. J.; Asundi, A. Noninterferometric Single-Shot Quantitative Phase Microscopy. *Opt. Lett.* **2013**, *38* (18), 3538−3541.
(202) Dunn, G. A.; Zicha, D. Dynamics of Fibroblast Spreading. *J. Cell Sci.* **1995**, *108*, 1239−1249.
(203) Kandel, M. E.; Lu, W.; Liang, J.; Aydin, O.; Saif, T. A.; Popescu, G. Cell-to-Cell Influence on Growth in Large Populations. *Biomed. Opt. Express* **2019**, *10* (9), 4664−4675.
(204) McNeal, A. S.; Belote, R. L.; Zeng, H.; Urquijo, M.; Barker, K.; Torres, R.; Curtin, M.; Shain, A. H.; Andtbacka, R. H.; Holmen, S.; Lum, D. H.; McCalmont, T. H.; VanBrocklin, M. W.; Grossman, D.; Wei, M. L.; Lang, U. E.; Judson-Torres, R. L. Braf(V600e) Induces Reversible Mitotic Arrest in Human Melanocytes Via Microrna-Mediated Suppression of Aurkb. *Elife* **2021**, *10*, 70385.
(205) Mugahid, D.; Kalocsay, M.; Liu, X. L.; Gruver, J. S.; Peshkin, L.; Kirschner, M. W. Yap Regulates Cell Size and Growth Dynamics Via Non-Cell Autonomous Mediators. *Elife* **2020**, *9*, 53404.
(206) Zangle, T. A.; Chun, J.; Zhang, J.; Reed, J.; Teitell, M. A. Quantification of Biomass and Cell Motion in Human Pluripotent Stem Cell Colonies. *Biophys. J.* **2013**, *105* (3), 593−601.
(207) Leslie, K. A.; Rasheed, M.; Sabo, R. T.; Roberts, C. C.; Toor, A. A.; Reed, J. Reconstituting Donor T Cells Increase Their Biomass Following Hematopoietic Stem Cell Transplantation. *Analyst* **2018**, *143* (11), 2479−2485.
(208) Waters, L. R.; Ahsan, F. M.; ten Hoeve, J.; Hong, J. S.; Kim, D. N. H.; Minasyan, A.; Braas, D.; Graeber, T. G.; Zangle, T. A.; Teitell, M. A. Ampk Regulates Igd Expression but Not Energy Stress with B Cell Activation. *Sci. Rep.* **2019**, *9*, 8176.
(209) Mitchell, S.; Roy, K.; Zangle, T. A.; Hoffmann, A. Nongenetic Origins of Cell-to-Cell Variability in B Lymphocyte Proliferation. *Proc. Natl. Acad. Sci. U. S. A.* **2018**, *115* (12), E2888−E2897.
(210) Pradeep, S.; Tasnim, T.; Zhang, H.; Zangle, T. A. Simultaneous Measurement of Neurite and Neural Body Mass Accumulation Via Quantitative Phase Imaging. *Analyst* **2021**, *146* (4), 1361−1368.
(211) Kandel, M. E.; Kim, E.; Lee, Y. J.; Tracy, G.; Chung, H. J.; Popescu, G. Multiscale Assay of Unlabeled Neurite Dynamics Using Phase Imaging with Computational Specificity. *ACS Sens* **2021**, *6* (5), 1864−1874.
(212) Wang, Z.; Millet, L.; Chan, V.; Ding, H.; Gillette, M. U.; Bashir, R.; Popescu, G. Label-Free Intracellular Transport Measured by Spatial Light Interference Microscopy. *J. Biomed. Opt.* **2011**, *16* (2), 026019.
(213) Jourdain, P.; Boss, D.; Rappaz, B.; Moratal, C.; Hernandez, M. C.; Depeursinge, C.; Magistretti, P. J.; Marquet, P. Simultaneous Optical Recording in Multiple Cells by Digital Holographic Microscopy of Chloride Current Associated to Activation of the Ligand-Gated Chloride Channel Gaba(a) Receptor. *PLoS One* **2012**, *7* (12), No. e51041.
(214) Solovei, I.; Kreysing, M.; Lanctot, C.; Kosem, S.; Peichl, L.; Cremer, T.; Guck, J.; Joffe, B. Nuclear Architecture of Rod Photoreceptor Cells Adapts to Vision in Mammalian Evolution. *Cell* **2009**, *137* (2), 356−68.
(215) Yurkin, M. A. How a Phase Image of a Cell with Nucleus Refractive Index Smaller Than That of the Cytoplasm Should Look Like? A Comment on Two Papers by Steelman Et Al. And Schurmann Et Al. Read the Responses to This Comment: E201800091 and E201800095. *J. Biophotonics* **2018**, *11* (6), e201800033.

https://doi.org/10.1021/acsnano.1c11507
ACS Nano XXXX, XXX, XXX−XXX

(216) Schurmann, M.; Scholze, J.; Muller, P.; Guck, J.; Chan, C. J. Cell Nuclei Have Lower Refractive Index and Mass Density Than Cytoplasm. *J. Biophotonics* **2016**, *9* (10), 1068−1076.
(217) Steelman, Z. A.; Eldridge, W. J.; Weintraub, J. B.; Wax, A. Is the Nuclear Refractive Index Lower Than Cytoplasm? Validation of Phase Measurements and Implications for Light Scattering Technologies. *J. Biophotonics* **2017**, *10* (12), 1714−1722.
(218) Muller, P.; Guck, J. Response to Comment on "Cell Nuclei Have Lower Refractive Index and Mass Density Than Cytoplasm" a Comment on "How a Phase Image of a Cell with Nucleus Refractive Index Smaller Than That of the Cytoplasm Should Look Like?", E201800033. *J. Biophotonics* **2018**, *11* (6), e201800095.
(219) Steelman, Z. A.; Eldridge, W. J.; Wax, A. Response to Comment on "Is the Nuclear Refractive Index Lower Than Cytoplasm? Validation of Phase Measurements and Implications for Light Scattering Technologies" a Comment on "How a Phase Image of a Cell with Nucleus Refractive Index Smaller Than That of the Cytoplasm Should Look Like?", E201800033. *J. Biophotonics* **2018**, *11* (6), e201800091.
(220) Kim, T.; Zhou, R. J.; Mir, M.; Babacan, S. D.; Carney, P. S.; Goddard, L. L.; Popescu, G. White-Light Diffraction Tomography of Unlabelled Live Cells. *Nat. Photonics* **2014**, *8* (3), 256−263.
(221) Kim, K.; Guck, J. The Relative Densities of Cytoplasm and Nuclear Compartments Are Robust against Strong Perturbation. *Biophys. J.* **2020**, *119* (10), 1946−1957.
(222) Liebel, M.; Ortega Arroyo, J.; Beltrán, V. S.; Osmond, J.; Jo, A.; Lee, H.; Quidant, R.; van Hulst, N. F. 3d Tracking of Extracellular Vesicles by Holographic Fluorescence Imaging. *Sci. Adv.* **2020**, *6* (45), No. eabc2508.
(223) Koslover, E. F.; Chan, C. K.; Theriot, J. A. Cytoplasmic Flow and Mixing Due to Deformation of Motile Cells. *Biophys. J.* **2017**, *113* (9), 2077−2087.
(224) Vicar, T.; Balvan, J.; Jaros, J.; Jug, F.; Kolar, R.; Masarik, M.; Gumulec, J. Cell Segmentation Methods for Label-Free Contrast Microscopy: Review and Comprehensive Comparison. *BMC Bioinf* **2019**, *20* (1), 360.
(225) Jensen, E. C. Types of Imaging, Part 2: An Overview of Fluorescence Microscopy. *Anat. Rec.* **2012**, *295* (10), 1621−1627.
(226) Kim, K.; Lee, S.; Yoon, J.; Heo, J.; Choi, C.; Park, Y. Three-Dimensional Label-Free Imaging and Quantification of Lipid Droplets in Live Hepatocytes. *Sci. Rep.* **2016**, *6*, 36815.
(227) Brown, A. F.; Dunn, G. A. Microinterferometry of the Movement of Dry Matter in Fibroblasts. *J. Cell Sci.* **1989**, *92*, 379−89.
(228) Kandel, M. E.; Fernandes, D.; Taylor, A. M.; Shakir, H.; Best-Popescu, C.; Popescu, G. Three-Dimensional Intracellular Transport in Neuron Bodies and Neurites Investigated by Label-Free Dispersion-Relation Phase Spectroscopy. *Cytometry Part A* **2017**, *91* (5), 519−526.
(229) Sandoz, P. A.; Tremblay, C.; van der Goot, F. G.; Frechin, M. Image-Based Analysis of Living Mammalian Cells Using Label-Free 3d Refractive Index Maps Reveals New Organelle Dynamics and Dry Mass Flux. *PLoS Biol.* **2019**, *17* (12), No. e3000553.
(230) Ma, L.; Rajshekhar, G.; Wang, R.; Bhaduri, B.; Sridharan, S.; Mir, M.; Chakraborty, A.; Iyer, R.; Prasanth, S.; Millet, L.; Gillette, M. U.; Popescu, G. Phase Correlation Imaging of Unlabeled Cell Dynamics. *Sci. Rep.* **2016**, *6*, 32702.
(231) Li, Y.; Di, J.; Wu, W.; Shang, P.; Zhao, J. Quantitative Investigation on Morphology and Intracellular Transport Dynamics of Migrating Cells. *Appl. Opt.* **2019**, *58* (34), G162−G168.
(232) Ceballos, S.; Kandel, M.; Sridharan, S.; Monroy, F.; Popescu, G. Nuclear Dynamics in Metastatic Cells Studied by Quantitative Phase Imaging. *SPIE BiOS* **2015**, *9336*, 93361Q.
(233) Zhang, Y.; Judson, R. L. Evaluation of Holographic Imaging Cytometer Holomonitor M4(R) Motility Applications. *Cytometry Part A* **2018**, *93* (11), 1125−1131.
(234) Kamlund, S.; Janicke, B.; Alm, K.; Judson-Torres, R. L.; Oredsson, S. Quantifying the Rate, Degree, and Heterogeneity of Morphological Change During an Epithelial to Mesenchymal Transition Using Digital Holographic Cytometry. *Appl. Sci.* **2020**, *10* (14), 4726.
(235) Lee, A. J.; Hugonnet, H.; Park, W.; Park, Y. Three-Dimensional Label-Free Imaging and Quantification of Migrating Cells During Wound Healing. *Biomed. Opt. Express* **2020**, *11* (12), 6812−6824.
(236) Park, K.; Lonsberry, G. E.; Gearing, M.; Levey, A. I.; Desai, J. P. Viscoelastic Properties of Human Autopsy Brain Tissues as Biomarkers for Alzheimer's Diseases. *IEEE. Trans. Biomed. Eng.* **2019**, *66* (6), 1705−1713.
(237) Cross, S. E.; Jin, Y. S.; Rao, J.; Gimzewski, J. K. Nanomechanical Analysis of Cells from Cancer Patients. *Nat. Nanotechnol.* **2007**, *2* (12), 780−3.
(238) Barriga, E. H.; Franze, K.; Charras, G.; Mayor, R. Tissue Stiffening Coordinates Morphogenesis by Triggering Collective Cell Migration in Vivo. *Nature* **2018**, *554* (7693), 523−527.
(239) Haase, K.; Pelling, A. E. Investigating Cell Mechanics with Atomic Force Microscopy. *J. R. Soc. Interface* **2015**, *12* (104), 20140970.
(240) Wu, P. H.; Aroush, D. R. B.; Asnacios, A.; Chen, W. C.; Dokukin, M. E.; Doss, B. L.; Durand-Smet, P.; Ekpenyong, A.; Guck, J.; Guz, N. V.; Janmey, P. A.; Lee, J. S. H.; Moore, N. M.; Ott, A.; Poh, Y. C.; Ros, R.; Sander, M.; Sokolov, I.; Staunton, J. R.; Wang, N.; Whyte, G.; Wirtz, D. A Comparison of Methods to Assess Cell Mechanical Properties. *Nat. Methods* **2018**, *15* (7), 491.
(241) Mason, T. G.; Weitz, D. A. Optical Measurements of Frequency-Dependent Linear Viscoelastic Moduli of Complex Fluids. *Phys. Rev. Lett.* **1995**, *74* (7), 1250−1253.
(242) Weihs, D.; Mason, T. G.; Teitell, M. A. Bio-Microrheology: A Frontier in Microrheology. *Biophys. J.* **2006**, *91* (11), 4296−4305.
(243) Squires, T. M.; Mason, T. G. Fluid Mechanics of Microrheology. *Annu. Rev. Fluid Mech.* **2010**, *42*, 413−438.
(244) Reed, J.; Frank, M.; Troke, J. J.; Schmit, J.; Han, S.; Teitell, M. A.; Gimzewski, J. K. High Throughput Cell Nanomechanics with Mechanical Imaging Interferometry. *Nanotechnology* **2008**, *19* (23), 235101.
(245) Chalut, K. J.; Ekpenyong, A. E.; Clegg, W. L.; Melhuish, I. C.; Guck, J. Quantifying Cellular Differentiation by Physical Phenotype Using Digital Holographic Microscopy. *Integr. Biol.* **2012**, *4* (3), 280−284.
(246) Park, Y.; Best, C. A.; Badizadegan, K.; Dasari, R. R.; Feld, M. S.; Kuriabova, T.; Henle, M. L.; Levine, A. J.; Popescu, G. Measurement of Red Blood Cell Mechanics During Morphological Changes. *Proc. Natl. Acad. Sci. U. S. A.* **2010**, *107* (15), 6731−6736.
(247) Eldridge, W. J.; Steelman, Z. A.; Loomis, B.; Wax, A. Optical Phase Measurements of Disorder Strength Link Microstructure to Cell Stiffness. *Biophys. J.* **2017**, *112* (4), 692−702.
(248) Eldridge, W. J.; Ceballos, S.; Shah, T.; Park, H. S.; Steelman, Z. A.; Zauscher, S.; Wax, A. Shear Modulus Measurement by Quantitative Phase Imaging and Correlation with Atomic Force Microscopy. *Biophys. J.* **2019**, *117* (4), 696−705.
(249) Steelman, Z. A.; Coker, Z. N.; Kiester, A.; Noojin, G.; Ibey, B. L.; Bixler, J. N. Quantitative Phase Microscopy Monitors Subcellular Dynamics in Single Cells Exposed to Nanosecond Pulsed Electric Fields. *J. Biophotonics* **2021**, *14* (10), e202170027.
(250) Nguyen, T. L.; Polanco, E. R.; Patananan, A. N.; Zangle, T. A.; Teitell, M. A. Cell Viscoelasticity Is Linked to Fluctuations in Cell Biomass Distributions. *Sci. Rep.* **2020**, *10* (1), 7403.
(251) Chun, J.; Zangle, T. A.; Kolarova, T.; Finn, R. S.; Teitell, M. A.; Reed, J. Rapidly Quantifying Drug Sensitivity of Dispersed and Clumped Breast Cancer Cells by Mass Profiling. *Analyst* **2012**, *137* (23), 5495−8.
(252) Huang, D.; Roy, I. J.; Murray, G. F.; Reed, J.; Zangle, T. A.; Teitell, M. A. Identifying Fates of Cancer Cells Exposed to Mitotic Inhibitors by Quantitative Phase Imaging. *Analyst* **2020**, *145* (1), 97−106.
(253) Saleh, T.; Tyutyunyk-Massey, L.; Murray, G. F.; Alotaibi, M. R.; Kawale, A. S.; Elsayed, Z.; Henderson, S. C.; Yakovlev, V.; Elmore, L. W.; Toor, A.; Harada, H.; Reed, J.; Landry, J. W.; Gewirtz, D. A.

https://doi.org/10.1021/acsnano.1c11507
ACS Nano XXXX, XXX, XXX−XXX

Tumor Cell Escape from Therapy-Induced Senescence. *Biochem. Pharmacol.* **2019**, *162*, 202−212.
(254) Murray, G. F.; Guest, D.; Mikheykin, A.; Toor, A.; Reed, J. Single Cell Biomass Tracking Allows Identification and Isolation of Rare Targeted Therapy-Resistant Dlbcl Cells within a Mixed Population. *Analyst* **2021**, *146* (4), 1157−1162.
(255) Murray, G. F.; Turner, T. H.; Leslie, K. A.; Alzubi, M. A.; Guest, D.; Sohal, S. S.; Teitell, M. A.; Harrell, J. C.; Reed, J. Live Cell Mass Accumulation Measurement Non-Invasively Predicts Carboplatin Sensitivity in Triple-Negative Breast Cancer Patient-Derived Xenografts. *ACS Omega* **2018**, *3* (12), 17687−17692.
(256) Polanco, E. R.; Moustafa, T. E.; Butterfield, A.; Scherer, S.; Cortes-Sanchez, E.; Bodily, T.; Welm, B. E.; Bernard, P. S.; Zangle, T. A. Multiparametric Quantitative Phase Imaging for Real-Time, Single Cell, Drug Screening in Breast Cancer. *bioRxiv*, 2021.11.26.467625, ver. 1. https://www.biorxiv.org/content/10.1101/2021.11.26.467625v1 (accessed 2022-05-26).
(257) Fackler, O. T.; Grosse, R. Cell Motility through Plasma Membrane Blebbing. *J. Cell Biol.* **2008**, *181* (6), 879−884.
(258) Wang, Z.; Tangella, K.; Balla, A.; Popescu, G. Tissue Refractive Index as Marker of Disease. *J. Biomed. Opt.* **2011**, *16* (11), 116017.
(259) Takabayashi, M.; Majeed, H.; Kajdacsy-Balla, A.; Popescu, G. Tissue Spatial Correlation as Cancer Marker. *J. Biomed. Opt.* **2019**, *24* (1), 1.
(260) Hejna, M.; Jorapur, A.; Song, J. S.; Judson, R. L. High Accuracy Label-Free Classification of Single-Cell Kinetic States from Holographic Cytometry of Human Melanoma Cells. *Sci. Rep.* **2017**, *7*, 11943.
(261) Park, Y.; Diez-Silva, M.; Popescu, G.; Lykotrafitis, G.; Choi, W.; Feld, M. S.; Suresh, S. Refractive Index Maps and Membrane Dynamics of Human Red Blood Cells Parasitized by Plasmodium Falciparum. *Proc. Natl. Acad. Sci. U. S. A.* **2008**, *105* (37), 13730−5.
(262) Mehta, D. S.; Srivastava, V. Quantitative Phase Imaging of Human Red Blood Cells Using Phase-Shifting White Light Interference Microscopy with Colour Fringe Analysis. *Appl. Phys. Lett.* **2012**, *101* (20), 203701.
(263) Liu, R.; Dey, D. K.; Boss, D.; Marquet, P.; Javidi, B. Recognition and Classification of Red Blood Cells Using Digital Holographic Microscopy and Data Clustering with Discriminant Analysis. *J. Opt. Soc. Am. A* **2011**, *28* (6), 1204−10.
(264) Pham, H. V.; Bhaduri, B.; Tangella, K.; Best-Popescu, C.; Popescu, G. Real Time Blood Testing Using Quantitative Phase Imaging. *PLoS One* **2013**, *8* (2), e55676.
(265) Ohene, Y.; Marinov, I.; de Laulanie, L.; Dupuy, C.; Wattelier, B.; Starikovskaia, S. Phase Imaging Microscopy for the Diagnostics of Plasma-Cell Interaction. *Appl. Phys. Lett.* **2015**, *106* (23), 233703.
(266) Rubessa, M.; Kandel, M. E.; Schreiber, S.; Meyers, S.; Beck, D. H.; Popescu, G.; Wheeler, M. B. Morphometric Analysis of Sperm Used for Ivp by Three Different Separation Methods with Spatial Light Interference Microscopy. *Syst. Biol. Reprod. Med.* **2020**, *66* (1), 26−36.
(267) Majeed, H.; Nguyen, T. H.; Kandel, M. E.; Kajdacsy-Balla, A.; Popescu, G. Label-Free Quantitative Evaluation of Breast Tissue Using Spatial Light Interference Microscopy (SLIM). *Sci. Rep.* **2018**, *8* (1), 6875.
(268) Erhardt, A.; Zinser, G.; Komitowski, D.; Bille, J. Reconstructing 3-D Light-Microscopic Images by Digital Image Processing. *Appl. Opt.* **1985**, *24* (2), 194−200.
(269) Pawley, J. B. *Handbook of Biological Confocal Microscopy*; Springer: New York, 2005.
(270) Wolf, E. Three-Dimensional Structure Determination of Semi-Transparent Objects from Holographic Data. *Opt. Commun.* **1969**, *1* (4), 153−156.
(271) Radon, J. On the Determination of Functions from Their Integral Values Along Certain Manifolds. *IEEE Trans. Med. Imaging* **1986**, *5* (4), 170−176.
(272) Richmond, C. Sir Godfrey Hounsfield. *BMJ: Br. Med. J.* **2004**, *329* (7467), 687.
(273) Fercher, A. F.; Bartelt, H.; Becker, H.; Wiltschko, E. Image Formation by Inversion of Scattered Field Data: Experiments and Computational Simulation. *Appl. Opt.* **1979**, *18* (14), 2427−39.
(274) Peter, C.; Wolfgang, L.; Dirk Van, D.; Jean-Pierre, G.; Michel, S.; Jose, B. Quantitative Phase Tomography by Holographic Reconstruction. *Proc. SPIE* **1999**, *3772*, 363731.
(275) Barty, A.; Nugent, K. A.; Roberts, A.; Paganin, D. Quantitative Phase Tomography. *Opt. Commun.* **2000**, *175* (4), 329−336.
(276) Charrière, F.; Pavillon, N.; Colomb, T.; Depeursinge, C.; Heger, T. J.; Mitchell, E. A. D.; Marquet, P.; Rappaz, B. Living Specimen Tomography by Digital Holographic Microscopy: Morphometry of Testate Amoeba. *Opt. Express* **2006**, *14* (16), 7005−7013.
(277) Choi, W.; Fang-Yen, C.; Badizadegan, K.; Oh, S.; Lue, N.; Dasari, R. R.; Feld, M. S. Tomographic Phase Microscopy. *Nat. Methods* **2007**, *4* (9), 717−9.
(278) Chen, M.; Tian, L.; Waller, L. 3d Differential Phase Contrast Microscopy. *Biomed. Opt. Express* **2016**, *7* (10), 3940−3950.
(279) Matlock, A.; Tian, L. High-Throughput, Volumetric Quantitative Phase Imaging with Multiplexed Intensity Diffraction Tomography. *Biomed. Opt. Express* **2019**, *10* (12), 6432−6448.
(280) Kuś, A.; Dudek, M.; Kemper, B.; Kujawińska, M.; Vollmer, A. Tomographic Phase Microscopy of Living Three-Dimensional Cell Cultures. *J. Biomed. Opt.* **2014**, *19* (4), 046009.
(281) Zuo, C.; Sun, J. S.; Li, J. J.; Asundi, A.; Chen, Q. Wide-Field High-Resolution 3d Microscopy with Fourier Ptychographic Diffraction Tomography. *Opt. Lasers Eng.* **2020**, *128*, 106003.
(282) Li, J.; Matlock, A.; Li, Y.; Chen, Q.; Zuo, C.; Tian, L. High-Speed in Vitro Intensity Diffraction Tomography. *Adv. Photonics* **2019**, *1* (06), 066004.
(283) Esposito, M.; Fang, C.; Cook, K. C.; Park, N.; Wei, Y.; Spadazzi, C.; Bracha, D.; Gunaratna, R. T.; Laevsky, G.; DeCoste, C. J.; Slabodkin, H.; Brangwynne, C. P.; Cristea, I. M.; Kang, Y. B. Tgf-Beta-Induced Dact1 Biomolecular Condensates Repress Wnt Signalling to Promote Bone Metastasis. *Nat. Cell Biol.* **2021**, *23* (3), 257.
(284) Choi, W. H.; Yun, Y.; Park, S.; Jeon, J. H.; Lee, J.; Lee, J. H.; Yang, S. A.; Kim, N. K.; Jung, C. H.; Kwon, Y. T.; Han, D.; Lim, S. M.; Lee, M. J. Aggresomal Sequestration and Stub1-Mediated Ubiquitylation During Mammalian Proteaphagy of Inhibited Proteasomes. *Proc. Natl. Acad. Sci. U. S. A.* **2020**, *117* (32), 19190−19200.
(285) Hong, Y.; Dao, K. P.; Kim, T.; Lee, S.; Shin, Y.; Park, Y.; Hwang, D. S. Label-Free Quantitative Analysis of Coacervates Via 3d Phase Imaging. *Adv. Opt. Mater.* **2021**, *9* (20), 2100697.
(286) Ledwig, P.; Robles, F. E. Epi-Mode Tomographic Quantitative Phase Imaging in Thick Scattering Samples. *Biomed. Opt. Express* **2019**, *10* (7), 3605−3621.
(287) Nguyen, T. H.; Kandel, M. E.; Rubessa, M.; Wheeler, M. B.; Popescu, G. Gradient Light Interference Microscopy for 3d Imaging of Unlabeled Specimens. *Nat. Commun.* **2017**, *8* (1), 210.
(288) Funamizu, H.; Aizu, Y. Three-Dimensional Quantitative Phase Imaging of Blood Coagulation Structures by Optical Projection Tomography in Flow Cytometry Using Digital Holographic Microscopy. *J. Biomed. Opt.* **2019**, *24* (3), 1−6.
(289) Ledwig, P.; Robles, F. E. Quantitative 3d Refractive Index Tomography of Opaque Samples in Epi-Mode. *Optica* **2021**, *8* (1), 6−14.
(290) Ziemczonok, M.; Kus, A.; Kujawinska, M. Optical Diffraction Tomography Meets Metrology - Measurement Accuracy on Cellular and Subcellular Level. *Measurement* **2022**, *195*, 111106.
(291) Wojtkowski, M. High-Speed Optical Coherence Tomography: Basics and Applications. *Appl. Opt.* **2010**, *49* (16), D30−D61.
(292) Huang, D.; Swanson, E. A.; Lin, C. P.; Schuman, J. S.; Stinson, W. G.; Chang, W.; Hee, M. R.; Flotte, T.; Gregory, K.; Puliafito, C. A.; et al. Optical Coherence Tomography. *Science* **1991**, *254* (5035), 1178−81.
(293) Fujimoto, J. G.; Pitris, C.; Boppart, S. A.; Brezinski, M. E. Optical Coherence Tomography: An Emerging Technology for Biomedical Imaging and Optical Biopsy. *Neoplasia* **2000**, *2* (1−2), 9−25.

https://doi.org/10.1021/acsnano.1c11507
ACS Nano XXXX, XXX, XXX−XXX

(294) Joo, C.; Akkin, T.; Cense, B.; Park, B. H.; de Boer, J. E. Spectral-Domain Optical Coherence Phase Microscopy for Quantitative Phase-Contrast Imaging. *Opt. Lett.* **2005**, *30* (16), 2131−2133.
(295) Choma, M. A.; Ellerbee, A. K.; Yang, C. H.; Creazzo, T. L.; Izatt, J. A. Spectral-Domain Phase Microscopy. *Opt. Lett.* **2005**, *30* (10), 1162−1164.
(296) Jonnal, R. S.; Kocaoglu, O. P.; Wang, Q.; Lee, S.; Miller, D. T. Phase-Sensitive Imaging of the Outer Retina Using Optical Coherence Tomography and Adaptive Optics. *Biomed. Opt. Express* **2012**, *3* (1), 104−124.
(297) Desissaire, S.; Schwarzhans, F.; Steiner, S.; Vass, C.; Fischer, G.; Pircher, M.; Hitzenberger, C. K. Temporal Phase Evolution Oct for Measurement of Tissue Deformation in the Human Retina in-Vivo. *Biomed. Opt. Express* **2021**, *12* (11), 7092−7112.
(298) Kim, K.; Choe, K.; Park, I.; Kim, P.; Park, Y. Holographic Intravital Microscopy for 2-D and 3-D Imaging Intact Circulating Blood Cells in Microcapillaries of Live Mice. *Sci. Rep.* **2016**, *6*, 33084.
(299) Sung, Y. J.; Choi, W.; Fang-Yen, C.; Badizadegan, K.; Dasari, R. R.; Feld, M. S. Optical Diffraction Tomography for High Resolution Live Cell Imaging. *Opt. Express* **2009**, *17* (1), 266−277.
(300) Hu, C. F.; Zhu, S. S.; Gao, L.; Popescu, G. Endoscopic Diffraction Phase Microscopy. *Opt. Lett.* **2018**, *43* (14), 3373−3376.
(301) Costa, P. C.; Guang, Z.; Ledwig, P.; Zhang, Z. B.; Neill, S.; Olson, J. J.; Robles, F. E. Towards in-Vivo Label-Free Detection of Brain Tumor Margins with Epi-Illumination Tomographic Quantitative Phase Imaging. *Biomed. Opt. Express* **2021**, *12* (3), 1621−1634.
(302) Gordon, G. S. D.; Joseph, J.; Alcolea, M. P.; Sawyer, T.; Williams, C.; Fitzpatrick, C. R. M.; Jones, P. H.; di Pietro, M.; Fitzgerald, R. C.; Wilkinson, T. D.; Bohndiek, S. E. Quantitative Phase and Polarization Imaging through an Optical Fiber Applied to Detection of Early Esophageal Tumorigenesis. *J. Biomed. Opt.* **2019**, *24* (12), 1.
(303) Park, Y.; Popescu, G.; Badizadegan, K.; Dasari, R. R.; Feld, M. S. Diffraction Phase and Fluorescence Microscopy. *Opt. Express* **2006**, *14* (18), 8263−8.
(304) Lue, N.; Choi, W.; Popescu, G.; Yaqoob, Z.; Badizadegan, K.; Dasari, R. R.; Feld, M. S. Live Cell Refractometry Using Hilbert Phase Microscopy and Confocal Reflectance Microscopy. *J. Phys. Chem. A* **2009**, *113* (47), 13327−30.
(305) Chowdhury, S.; Eldridge, W. J.; Wax, A.; Izatt, J. A. Structured Illumination Multimodal 3d-Resolved Quantitative Phase and Fluorescence Sub-Diffraction Microscopy. *Biomed. Opt. Express* **2017**, *8* (5), 2496−2518.
(306) Kemper, B.; Schmidt, L.; Przibilla, S.; Rommel, C.; Vollmer, A.; Ketelhut, S.; Schnekenburger, J.; von Bally, G. Influence of Sample Preparation and Identification of Subcelluar Structures in Quantitative Holographic Phase Contrast Microscopy. *Biophotonics: Photonic Solutions for Better Health Care Ii* **2010**, *7715*, 771504.
(307) Barroso, A.; Woerdemann, M.; Vollmer, A.; von Bally, G.; Kemper, B.; Denz, C. Three-Dimensional Exploration and Mechano-Biophysical Analysis of the Inner Structure of Living Cells. *Small* **2013**, *9* (6), 885−93.
(308) Weaver, S. S.; Li, Y. F.; Foucard, L.; Majeed, H.; Bhaduri, B.; Levine, A. J.; Kilian, K. A.; Popescu, G. Simultaneous Cell Traction and Growth Measurements Using Light. *J. Biophotonics* **2019**, *12* (3), e201800182.
(309) Sridharan, S.; Li, Y. F.; Bhaduri, B.; Majeed, H.; Dupenloup, P.; Levine, A.; Kilian, K. A.; Popescu, G. Hilbert Phase Dynamometry (Hpd) for Real-Time Measurement of Cell Generated Forces. *SPIE BiOS* **2016**, *9718*, 97182F.
(310) Chowdhury, S.; Eldridge, W. J.; Wax, A.; Izatt, J. A. Structured Illumination Microscopy for Dual-Modality 3d Sub-Diffraction Resolution Fluorescence and Refractive-Index Reconstruction. *Biomed. Opt. Express* **2017**, *8* (12), 5776−5793.
(311) Tamamitsu, M.; Toda, K.; Shimada, H.; Honda, T.; Takarada, M.; Okabe, K.; Nagashima, Y.; Horisaki, R.; Ideguchi, T. Label-Free Biochemical Quantitative Phase Imaging with Mid-Infrared Photothermal Effect. *Optica* **2020**, *7* (4), 359−366.
(312) Jung, J.; Hong, S. J.; Kim, H. B.; Kim, G.; Lee, M.; Shin, S.; Lee, S.; Kim, D. J.; Lee, C. G.; Park, Y. Label-Free Non-Invasive Quantitative Measurement of Lipid Contents in Individual Microalgal Cells Using Refractive Index Tomography. *Sci. Rep.* **2018**, *8*, 6524.
(313) Schurmann, M.; Cojoc, G.; Girardo, S.; Ulbricht, E.; Guck, J.; Muller, P. Three-Dimensional Correlative Single-Cell Imaging Utilizing Fluorescence and Refractive Index Tomography. *J. Biophotonics* **2018**, *11* (3), e201700145.
(314) Kim, K.; Park, W. S.; Na, S.; Kim, S.; Kim, T.; Do Heo, W.; Park, Y. Correlative Three-Dimensional Fluorescence and Refractive Index Tomography: Bridging the Gap between Molecular Specificity and Quantitative Bioimaging. *Biomed. Opt. Express* **2017**, *8* (12), 5688−5697.
(315) Descloux, A.; Grussmayer, K. S.; Bostan, E.; Lukes, T.; Bouwens, A.; Sharipov, A.; Geissbuehler, S.; Mahul-Mellier, A. L.; Lashuel, H. A.; Leutenegger, M.; Lasser, T. Combined Multi-Plane Phase Retrieval and Super-Resolution Optical Fluctuation Imaging for 4d Cell Microscopy. *Nat. Photonics* **2018**, *12* (3), 165.
(316) Rinehart, M.; Zhu, Y.; Wax, A. Quantitative Phase Spectroscopy. *Biomed. Opt. Express* **2012**, *3* (5), 958−965.
(317) Jung, J. H.; Jang, J.; Park, Y. Spectro-Refractometry of Individual Microscopic Objects Using Swept-Source Quantitative Phase Imaging. *Anal. Chem.* **2013**, *85* (21), 10519−25.
(318) Rinehart, M. T.; Park, H. S.; Walzer, K. A.; Chi, J. T.; Wax, A. Hemoglobin Consumption by P. Falciparum in Individual Erythrocytes Imaged Via Quantitative Phase Spectroscopy. *Sci. Rep.* **2016**, *6*, 24461.
(319) Jung, J.; Kim, K.; Yoon, J.; Park, Y. Hyperspectral Optical Diffraction Tomography. *Opt. Express* **2016**, *24* (3), 2006−12.
(320) Baiz, C. R.; Blasiak, B.; Bredenbeck, J.; Cho, M.; Choi, J. H.; Corcelli, S. A.; Dijkstra, A. G.; Feng, C. J.; Garrett-Roe, S.; Ge, N. H.; Hanson-Heine, M. W. D.; Hirst, J. D.; Jansen, T. L. C.; Kwac, K.; Kubarych, K. J.; Londergan, C. H.; Maekawa, H.; Reppert, M.; Saito, S.; Roy, S.; Skinner, J. L.; Stock, G.; Straub, J. E.; Thielges, M. C.; Tominaga, K.; Tokmakoff, A.; Torii, H.; Wang, L.; Webb, L. J.; Zanni, M. T. Vibrational Spectroscopic Map, Vibrational Spectroscopy, and Intermolecular Interaction. *Chem. Rev.* **2020**, *120* (15), 7152−7218.
(321) Kang, J. W.; Lue, N.; Kong, C. R.; Barman, I.; Dingari, N. C.; Goldfless, S. J.; Niles, J. C.; Dasari, R. R.; Feld, M. S. Combined Confocal Raman and Quantitative Phase Microscopy System for Biomedical Diagnosis. *Biomed. Opt. Express* **2011**, *2* (9), 2484−92.
(322) Singh, S. P.; Kang, S.; Kang, J. W.; So, P. T. C.; Dasari, R. R.; Yaqoob, Z.; Barman, I. Label-Free Characterization of Ultra Violet-Radiation-Induced Changes in Skin Fibroblasts with Raman Spectroscopy and Quantitative Phase Microscopy. *Sci. Rep.* **2017**, *7* (1), 10829.
(323) Dubey, V.; Ahmad, A.; Butola, A.; Qaiser, D.; Srivastava, A.; Mehta, D. S. Low Coherence Quantitative Phase Microscopy with Machine Learning Model and Raman Spectroscopy for the Study of Breast Cancer Cells and Their Classification. *Appl. Opt.* **2019**, *58* (5), A112−A119.
(324) Prevedel, R.; Diz-Munoz, A.; Ruocco, G.; Antonacci, G. Brillouin Microscopy: An Emerging Tool for Mechanobiology. *Nat. Methods* **2019**, *16* (10), 969−977.
(325) Raghunathan, R.; Zhang, J.; Wu, C.; Rippy, J.; Singh, M.; Larin, K. V.; Scarcelli, G. Evaluating Biomechanical Properties of Murine Embryos Using Brillouin Microscopy and Optical Coherence Tomography. *J. Biomed. Opt.* **2017**, *22* (8), 1−6.
(326) Zhang, J.; Raghunathan, R.; Rippy, J.; Wu, C.; Finnell, R. H.; Larin, K. V.; Scarcelli, G. Tissue Biomechanics During Cranial Neural Tube Closure Measured by Brillouin Microscopy and Optical Coherence Tomography. *Birth Defects Res.* **2019**, *111* (14), 991−998.
(327) Schlüßler, R.; Kim, K.; Nötzel, M.; Taubenberger, A.; Abuhattum, S.; Beck, T.; Müller, P.; Maharana, S.; Cojoc, G.; Girardo, S.; Hermann, A.; Alberti, S.; Guck, J. Correlative All-Optical Quantification of Mass Density and Mechanics of Subcellular Compartments with Fluorescence Specificity. *ELife* **2022**, *11*, No. e68490.

https://doi.org/10.1021/acsnano.1c11507
ACS Nano XXXX, XXX, XXX−XXX

(328) Roberts, A. B.; Zhang, J. T.; Singh, V. R.; Nikolic, M.; Moeendarbary, E.; Kamm, R. D.; So, P. T. C.; Scarcelli, G. Tumor Cell Nuclei Soften During Transendothelial Migration. *J. Biomech.* **2021**, *121*, 110400.
(329) Guo, S. M.; Yeh, L. H.; Folkesson, J.; Ivanov, I. E.; Krishnan, A. P.; Keefe, M. G.; Hashemi, E.; Shin, D.; Chhun, B. B.; Cho, N. H.; Leonetti, M. D.; Han, M. H.; Nowakowski, T. J.; Mehta, S. B. Revealing Architectural Order with Quantitative Label-Free Imaging and Deep Learning. *Elife* **2020**, *9*, 55502.
(330) Jo, Y.; Cho, H.; Lee, S. Y.; Choi, G.; Kim, G.; Min, H.-s.; Park, Y. Quantitative Phase Imaging and Artificial Intelligence: A Review. *IEEE J. Sel. Top. Quantum Electron* **2019**, *25* (1), 1−14.
(331) Paine, S. W.; Fienup, J. R. Machine Learning for Improved Image-Based Wavefront Sensing. *Opt. Lett.* **2018**, *43* (6), 1235−1238.
(332) Nishizaki, Y.; Valdivia, M.; Horisaki, R.; Kitaguchi, K.; Saito, M.; Tanida, J.; Vera, E. Deep Learning Wavefront Sensing. *Opt. Express* **2019**, *27* (1), 240−251.
(333) Zhou, Z.; Xia, J.; Wu, J.; Chang, C.; Ye, X.; Li, S.; Du, B.; Zhang, H.; Tong, G. Learning-Based Phase Imaging Using a Low-Bit-Depth Pattern. *Photonics Res.* **2020**, *8* (10), 1624.
(334) Wang, K.; Li, Y.; Kemao, Q.; Di, J.; Zhao, J. One-Step Robust Deep Learning Phase Unwrapping. *Opt. Express* **2019**, *27* (10), 15100−15115.
(335) Ronneberger, O.; Fischer, P.; Brox, T. In U-Net: Convolutional Networks for Biomedical Image Segmentation, *Medical Image Computing and Computer-Assisted Intervention − MICCAI 2015*; Springer: Cham, 2015; pp 234−241.
(336) Midtvedt, B.; Helgadottir, S.; Argun, A.; Pineda, J.; Midtvedt, D.; Volpe, G. Quantitative Digital Microscopy with Deep Learning. *Appl. Phys. Rev.* **2021**, *8* (1), 011310.
(337) Sheneman, L.; Stephanopoulos, G.; Vasdekis, A. E. Deep Learning Classification of Lipid Droplets in Quantitative Phase Images. *PLoS One* **2021**, *16* (4), No. e0249196.
(338) Rivenson, Y.; Liu, T.; Wei, Z.; Zhang, Y.; de Haan, K.; Ozcan, A. Phasestain: The Digital Staining of Label-Free Quantitative Phase Microscopy Images Using Deep Learning. *Light: Sci. Appl.* **2019**, *8*, 23.
(339) Nygate, Y. N.; Levi, M.; Mirsky, S. K.; Turko, N. A.; Rubin, M.; Barnea, I.; Dardikman-Yoffe, G.; Haifler, M.; Shalev, A.; Shaked, N. T. Holographic Virtual Staining of Individual Biological Cells. *Proc. Natl. Acad. Sci. U. S. A.* **2020**, *117* (17), 9223−9231.
(340) Ozaki, Y.; Yamada, H.; Kikuchi, H.; Hirotsu, A.; Murakami, T.; Matsumoto, T.; Kawabata, T.; Hiramatsu, Y.; Kamiya, K.; Yamauchi, T.; Goto, K.; Ueda, Y.; Okazaki, S.; Kitagawa, M.; Takeuchi, H.; Konno, H. Label-Free Classification of Cells Based on Supervised Machine Learning of Subcellular Structures. *PLoS One* **2019**, *14* (1), No. e0211347.
(341) Jo, Y.; Cho, H.; Park, W. S.; Kim, G.; Ryu, D.; Kim, Y. S.; Lee, M.; Park, S.; Lee, M. J.; Joo, H.; Jo, H.; Lee, S.; Lee, S.; Min, H. S.; Heo, W. D.; Park, Y. Label-Free Multiplexed Microtomography of Endogenous Subcellular Dynamics Using Generalizable Deep Learning. *Nat. Cell Biol.* **2021**, *23* (12), 1329−1337.
(342) Kandel, M. E.; He, Y. R.; Lee, Y. J.; Chen, T. H.-Y.; Sullivan, K. M.; Aydin, O.; Saif, M. T. A.; Kong, H.; Sobh, N.; Popescu, G. Phase Imaging with Computational Specificity (PICS) for Measuring Dry Mass Changes in Sub-Cellular Compartments. *Nat. Commun.* **2020**, *11* (1), 6256.
(343) Javidi, B.; Moon, I.; Yeom, S.; Carapezza, E. Three-Dimensional Imaging and Recognition of Microorganism Using Single-Exposure on-Line (SEOL) Digital Holography. *Opt. Express* **2005**, *13* (12), 4492−4506.
(344) Moon, I.; Javidi, B. Volumetric Three-Dimensional Recognition of Biological Microorganisms Using Multivariate Statistical Method and Digital Holography. *J. Biomed. Opt.* **2006**, *11* (6), 064004.
(345) Jo, Y.; Park, S.; Jung, J.; Yoon, J.; Joo, H.; Kim, M.-h.; Kang, S.-J.; Choi, M. C.; Lee, S. Y.; Park, Y. Holographic Deep Learning for Rapid Optical Screening of Anthrax Spores. *Sci. Adv.* **2017**, *3* (8), No. e1700606.
(346) Jo, Y.; Jung, J.; Kim, M. H.; Park, H.; Kang, S. J.; Park, Y. Label-Free Identification of Individual Bacteria Using Fourier Transform Light Scattering. *Opt. Express* **2015**, *23* (12), 15792−805.
(347) Barker, K. L.; Boucher, K. M.; Judson-Torres, R. L. Label-Free Classification of Apoptosis, Ferroptosis and Necroptosis Using Digital Holographic Cytometry. *Appl. Sci.* **2020**, *10* (13), 4439.
(348) Butola, A.; Popova, D.; Prasad, D. K.; Ahmad, A.; Habib, A.; Tinguely, J. C.; Basnet, P.; Acharya, G.; Senthilkumaran, P.; Mehta, D. S.; Ahluwalia, B. S. High Spatially Sensitive Quantitative Phase Imaging Assisted with Deep Neural Network for Classification of Human Spermatozoa under Stressed Condition. *Sci. Rep.* **2020**, *10* (1), 13118.
(349) Mirsky, S. K.; Barnea, I.; Levi, M.; Greenspan, H.; Shaked, N. T. Automated Analysis of Individual Sperm Cells Using Stain-Free Interferometric Phase Microscopy and Machine Learning. *Cytometry Part A* **2017**, *91* (9), 893−900.
(350) Singh, V.; Srivastava, V.; Mehta, D. S. Machine Learning-Based Screening of Red Blood Cells Using Quantitative Phase Imaging with Micro-Spectrocolorimetry. *Opt. Laser Technol.* **2020**, *124*, 105980.
(351) Kim, G.; Jo, Y.; Cho, H.; Min, H. S.; Park, Y. Learning-Based Screening of Hematologic Disorders Using Quantitative Phase Imaging of Individual Red Blood Cells. *Biosens. Bioelectron.* **2019**, *123*, 69−76.
(352) Javidi, B.; Markman, A.; Rawat, S.; O'Connor, T.; Anand, A.; Andemariam, B. Sickle Cell Disease Diagnosis Based on Spatio-Temporal Cell Dynamics Analysis Using 3d Printed Shearing Digital Holographic Microscopy. *Opt. Express* **2018**, *26* (10), 13614−13627.
(353) Go, T.; Kim, J. H.; Byeon, H.; Lee, S. J. Machine Learning-Based in-Line Holographic Sensing of Unstained Malaria-Infected Red Blood Cells. *J. Biophotonics* **2018**, *11* (9), No. e201800101.
(354) Pasquale, M.; Vittorio, B.; Pierluigi, C.; Andouglas Goncalves da Silva, J.; Luiz Marcos Garcia, G.; Francesco, M.; Melania, P.; Cosimo, D.; Pietro, F. *Identification and Classification of Biological Micro-Organisms by Holographic Learning* **2019**, *11060*, 110600H.
(355) Lam, V.; Nguyen, T.; Bui, V.; Chung, B. M.; Chang, L. C.; Nehmetallah, G.; Raub, C. Quantitative Scoring of Epithelial and Mesenchymal Qualities of Cancer Cells Using Machine Learning and Quantitative Phase Imaging. *J. Biomed. Opt.* **2020**, *25* (2), 1−17.
(356) Lam, V. K.; Nguyen, T.; Phan, T.; Chung, B. M.; Nehmetallah, G.; Raub, C. B. Machine Learning with Optical Phase Signatures for Phenotypic Profiling of Cell Lines. *Cytometry Part A* **2019**, *95* (7), 757−768.
(357) Nguyen, T. H.; Sridharan, S.; Macias, V.; Kajdacsy-Balla, A.; Melamed, J.; Do, M. N.; Popescu, G. Automatic Gleason Grading of Prostate Cancer Using Quantitative Phase Imaging and Machine Learning. *J. Biomed. Opt.* **2017**, *22* (3), 036015.
(358) Pavillon, N.; Hobro, A. J.; Akira, S.; Smith, N. I. Noninvasive Detection of Macrophage Activation with Single-Cell Resolution through Machine Learning. *Proc. Natl. Acad. Sci. U. S. A.* **2018**, *115* (12), E2676−E2685.
(359) Paidi, S. K.; Raj, P.; Bordett, R.; Zhang, C.; Karandikar, S. H.; Pandey, R.; Barman, I. Raman and Quantitative Phase Imaging Allow Morpho-Molecular Recognition of Malignancy and Stages of B-Cell Acute Lymphoblastic Leukemia. *Biosens. Bioelectron.* **2021**, *190*, 113403.

https://doi.org/10.1021/acsnano.1c11507
ACS Nano XXXX, XXX, XXX−XXX